UNIVERSITY OF OKLAHOMA

GRADUATE COLLEGE

A MICROPHYSICAL ANALYSIS OF THE STRATIFORM RAIN REGION OF MESOSCALE CONVECTIVE SYSTEMS USING POLARIMETRIC RADAR AND IN SITU AIRCRAFT MEASUREMENTS

A THESIS

SUBMITTED TO THE GRADUATE FACULTY

in partial fulfillment of the requirements for the

Degree of

MASTER OF SCIENCE IN METEOROLOGY

By

AMANDA MURPHY
Norman, Oklahoma
2018

A MICROPHYSICAL ANALYSIS OF THE STRATIFORM RAIN REGION OF MESOSCALE CONVECTIVE SYSTEMS USING POLARIMETRIC RADAR AND IN SITU AIRCRAFT MEASUREMENTS

A THESIS APPROVED FOR THE
SCHOOL OF METEOROLOGY

BY

Dr. Alexander Ryzhkov, Chair

Dr. Cameron Homeyer

Dr. Guifu Zhang

Dr. Greg McFarquhar

Acknowledgments

This thesis would have never been possible without the guidance and support of my advisor, Dr. Alexander Ryzhkov, so it is only appropriate that he is the first person I thank. I could have never imagined being able to work with and under the guidance of Dr. Ryzhkov, and I am so grateful to be his student and learn from him. His way of teaching, starting from the most basic concepts and building to the most difficult, has vastly increased my knowledge of polarimetry and radar meteorology in the past two years, and I'm thrilled to be able to continue working with him for my Ph.D.

I am also lucky to have such an involved and supportive committee. Dr. Guifu Zhang has taught me so much about weather radar polarimetry from his course, and I am incredibly grateful to be able to learn from him. Dr. Cameron Homeyer has been profoundly encouraging during this process, and never passes without giving a smile and bright hello. He has pushed me to dig deeper into my work, and always poses thoughtful and challenging questions. And finally, I have known Dr. Greg McFarquhar since my time back at the University of Illinois, where he and Dr. Bob Rauber gave me an opportunity to work under them for two years and opened the door for me to all kinds of research opportunities. I am forever indebted to the both of them, and have a great respect for Dr. McFarquhar and the thorough way he has taught me and still expects me to conduct research. I am lucky to work so closely with all three of my committee members.

Of course, outside of my committee, a number of other people have been heavily involved in this research. A huge thanks goes to Dr. Pengfei Zhang, for providing so much guidance on making QVPs and CVPs, including writing the original CVP code, helping me make modifications specifically for this study, and providing seemingly endless encouragement. Dr. Terry Schuur provided mobile radar data, and Dr. Jeff Snyder helped tremendously with viewing and understanding those data. Drs.

Wei Wu and Dan Stechman provided aircraft in situ data, and DYNAMO data were provided by NCAR/EOL under the sponsorship of the National Science Foundation (https://data.eol.ucar.edu/). Finally, Drs. Jake Carlin, Petar Bukovcic, and Katie Wilson were incredibly supportive during this process, offering both scientific input and tons of encouragement, from my first few days suffering through classes to writing and presenting the work herein.

Outside of work, a number of people and organizations have helped me tremendously through this process and made Norman feel like home. To the St. Thomas More University Parish Choir and Koda Crossfit Norman, thank you for accepting me with open arms, and for the welcome distractions from work. I'm also indebted to the friends I lean on each and every day, especially Natalie, Elisa, Brian, and Briana. Through difficult times professionally, and even more so personally, you were always there and always supported me, offering a helping hand and thoughtful advice (even if I was sometimes too stubborn to take it). I'm so grateful for your honesty, support, and friendship.

Finally, thank you to my family for allowing me to move so far away to do all of this. You believe in me when I don't believe in myself, and for your endless encouragement and sporadic cards in the mail, I am forever grateful. Your support means more to me than you will ever know, and I would never be able to do this without you.

Partial support for this work comes from grant DE-SC0014925. This thesis was prepared by Amanda Murphy with funding provided by NOAA/Office of Oceanic and Atmospheric Research under NOAA-University of Oklahoma Cooperative Agreement number NA11OAR4320072, U.S. Department of Commerce. The statements, findings, conclusions, and recommendations are those of the author and do not necessarily reflect the views of NOAA or the U.S. Department of Commerce.

Table of Contents

List of Tables

List of Figures

Abstract

The benefits of using polarimetric weather radar data to infer microphysical properties of and processes within observed precipitation is becoming more widely recognized. The quasi-vertical profile (QVP) technique has emerged as one way to examine vertical profiles of precipitation, but is not ideal for investigations of finescale polarimetric signatures. In this study, a new radar data processing technique, the column-vertical profile (CVP) technique, is introduced as an alternative way to process and present operational polarimetric radar data in a time-height format. Using CVP data, polarimetric ice microphysical retrieval algorithms are used in conjunction with aircraft in situ microphysical data to gain a deeper understanding of the ice microphysical structure of MCSs, and determine the usefulness and effectiveness of such new ice microphysical retrieval algorithms and the CVP technique. In situ aircraft microphysical data from two flights in both the MC3E and PECAN campaigns were analyzed as the UND Citation and P-3 aircraft flew within the stratiform rain region of four total MCSs. Vertical profiles of polarimetric variables were created following the aircraft using the CVP technique, and compared to analogous profiles made with GridRad radar data. CVP profiles were quite similar to those made with GridRad data, except for the enhanced vertical resolution of CVPs, confirming the effectiveness of the CVP technique in resolving vertical profiles of radar data along the flight track.

Novel ice microphysical algorithms were applied to these CVPs to get retrievals of D_m, N_t, and IWC. Extracting polarimetric radar data from the CVP along the flight track, point-by-point comparisons of in situ aircraft and radar retrieved ice microphysical data were made, and the effectiveness of the retrievals was examined in regions of low Z_{DR}, low K_{DP}, large CVP distance from the radar, and small distance above the melting layer. It was found that small distance above the ML was the best

predictor of poor quality retrievals, with a distance of ≤ 1 km above the ML related to worse estimates of all 3 variables.

Additionally, these retrievals were performed on QVPs of archetypal MCSs from both midlatitude and tropical environments. In midlatitude MCSs, an increase of D_m and decrease of N_t with depth, with a nearly constant IWC, suggest aggregation through the depth of the cloud. In tropical MCSs, nearly constant D_m paired with increasing N_t and IWC with depth suggest nucleation of new hydrometeors with much weaker aggregation.

Chapter 1

Introduction and Background

1.1 Microphysical Properties of Stratiform Regions of Mesoscale Convective Systems (MCSs)

Mesoscale convective systems (MCSs) are one of the most pervasive thunderstorm types in the United States. Houze (2004) broadly defines an MCS as "a cumulonimbus cloud system that produces a contiguous precipitation area 100 km or more in at least one direction." MCSs occur throughout large parts of the United States, often producing severe weather (e.g., Parker and Johnson, 2004) such as damaging straight line winds, hail, and tornadoes (e.g., Storm et al., 2007). Some of the first investigations into MCSs included Newton (1950), Fujita (1955), and Pedgley (1962) in the midlatitudes, and Hamilton and Archbold (1945) and Zipser (1969) in the tropics. A thorough review of the internal structure, dynamics, and large-scale interactions of MCSs beyond the general overview which is offered herein can be found in Houze (2004) and Houze (2018).

MCSs typically consist of a leading convective line, a transition zone, and a trailing stratiform region. Houze et al. (1990) found that two-thirds of mesoscale precipitation systems contributing to major rain events during the springtime in Oklahoma from 1977-82 could be classified as leading line-trailing stratiform types. Additionally, Parker and Johnson (2000) found that, in May of 1996 and 1997, the trailing stratiform mode of linear MCSs accounted for 60% of all MCSs observed. A widely accepted conceptual model of the vertical structure of an MCS is presented in Houze et al. (1989), shown as Fig. 1.1 herein. This model shows a "vertical cross section (oriented perpendicular to the line of convective clouds) through a squall line with

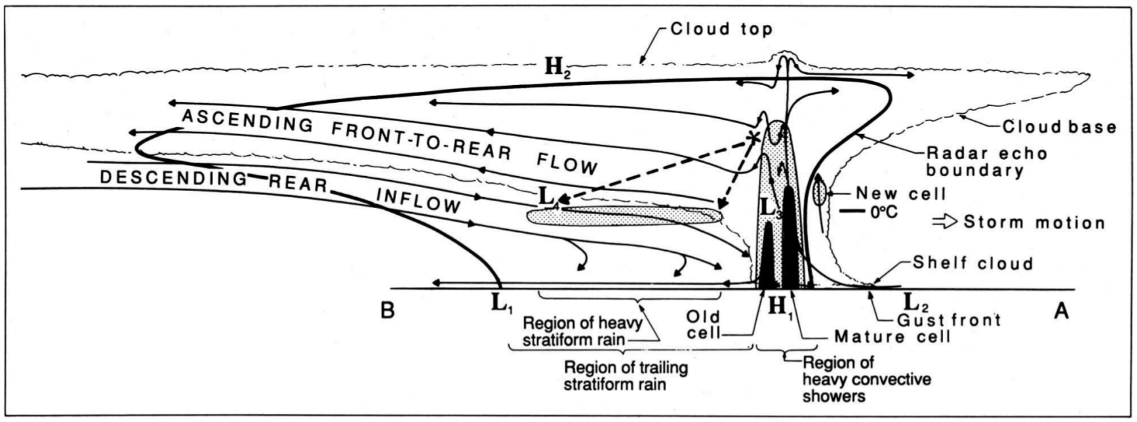

Figure 1.1: Conceptual model of a squall line with a trailing stratiform area viewed in a vertical cross section oriented perpendicular to the convective line (i.e., parallel to its motion). Taken from Houze et al. (1989).

trailing stratiform precipiation region." The heavy black and light scalloped lines indicate the extent of the cloud that is observed via weather radar and satellite observations, respectively. Stippled regions are indicative of enhanced radar reflectivity.

The trailing stratiform region dominates the horizontal area that the MCS covers, with a cloud shield extending well beyond what is observed by the radar. Within the trailing stratiform region on Fig. 1.1, there exists a region of enhanced radar reflectivity at a nearly constant altitude and of limited depth. This band of enhanced reflectivity indicates the level at which ice particles are melting into rain, referred to as the melting layer (ML), with the enhancement itself referred to as the "bright band" (e.g., Austin and Bemis (1950) and references therein). This enhancement occurs because as the snowflakes melt, they acquire a thin water coating, enhancing the particle's dielectric constant as observed by the radar. This enhancement does not extend to the ground, however, since as the ice particles melt and collapse into raindrops, their terminal fall speed increases dramatically, reducing the total number concentration of hydrometeors in a unit volume below the ML and therefore reducing reflectivity.

Aside from the MCS dynamics discussed in Houze et al. (1989) and Houze (2004), another important area of study concerning MCSs is their microphysical structure. A number of field campaigns have focused on gaining a deeper understanding of the microphysical structure of MCSs, including the Bow Echo and MCV Experiment (BAMEX; Davis et al., 2004), the Midlatitude Convective Clouds Experiment (MC3E; Jensen et al., 2016), and the Plains Elevated Convection At Night Field Project (PECAN; Geerts et al., 2017). Such campaigns and studies typically focus on the trailing stratiform region, as that region is much safer to fly and collect measurements in than the leading convective line. Of particular interest are regions such as the ML and dendritic growth layer (DGL), a zone from -10 to -20 °C where particles can grow quickly via diffusion and often grow in a highly anisotropic manner (e.g., Bailey and Hallett, 2009).

A thorough understanding of the ice microphysical properties of the stratiform rain region of MCSs is imperative for two main reasons. The first is that such regions typically contain high concentrations of very small ice crystals, especially between regions from -10 to -50 °C (e.g., Fridlind et al., 2015). This creates a serious risk for commercial aviation due to possible engine power loss and damage from aircraft engines ingesting ice in regions of low reflectivity ($Z < 20$ dBZ) where such aircraft do not expect a high concentration of ice. The values of ice water content (IWC) in the high ice water content (HIWC) regions can be as high as 3-4 g/m^3, with typical median volume diameters of ice particles less than 0.5 mm (Fridlind et al., 2015; Strapp et al., 2016; Leroy et al., 2017).

The second reason why understanding the ice microphysical properties of these regions is imperative is that modeling studies have yet to fully capture the structure of the stratiform rain region of MCSs, especially at high altitudes. Fridlind et al. (2017) modeled the microphysical structure of a midlatitude continental MCS observed on May 20, 2011 during the MC3E field campaign, and found that the simulation they used overpredicted mean volume diameter of ice particles by a factor of 3-5 and underpredicted number concentration by up to an order of magnitude. The simulated radar reflectivity at high altitudes was about 20 dBZ higher than that measured with radars. Fan et al. (2015) found a similar result for the same MCS, as did Stanford et al. (2017) in for a tropical MCS near Darwin, Australia, using a C-band polarimetric radar for observations and multiple microphysical parameterization schemes within their model. Both studies showed that modeling attempts highly overestimated the size of particles and reflectivity in the higher regions of the cloud. All of these studies show a deficiency in the community's ability to model microphysical processes and properties of such stratiform rain, and a need for additional details about the ice microphysical properties of MCSs.

The majority of the information collected about the microphysical structure of MCSs has been done via the use of in situ instrumentation, especially aircraft in situ probes. Aircraft in situ data, including IWC, total number concentration per unit volume (N_t), and median mass diameter (D_{mm}) provide valuable information about the properties of hydrometeors observed within a given volume. However, collecting information in this manner is incredibly costly, primarily done only during large field campaigns, and is only collected on a thin path where the aircraft flies. A more effective way to gain a deeper understanding of the microphysical structure of these regions would be to use data that are collected much more regularly, and on a much larger scale. Weather radar data, particularly data collected by the United States Weather Surveillance Radar, 1988, Doppler (WSR-88D) operational S-band weather radar network, can potentially serve as those data. A total of 143 WSR-88D weather radars exist all over the United States, and perform volume scans on the order of every 5 minutes (Crum and Alberty, 1993). Additionally, with the network's recent upgrade to dual-polarization capabilities, opportunities abound to further relate polarimetric signatures to microphysical properties of different precipitation structures.

1.2 Ice Microphysical Retrieval Techniques

To use weather radar data most effectively to further understand the stratiform rain region of MCSs, first these data must be examined in conjunction with aircraft in situ data to determine the meaning of various single- and dual-polarization signatures observed within the WSR-88D data. The most notable example of retrieving hydrometeor properties from polarimetric weather radar data is the development of the WSR-88D hydrometeor classification algorithm (HCA; see Park et al., 2009, and references therein). However, HCA output gives insight into what the dominant hydrometeor type likely is in a given radar volume (e.g., dry aggregated snow, graupel, heavy rain, etc.), but does not offer any quantitative information on the particles' shapes, sizes, or concentrations.

For specific information about the ice microphysical properties of radar observed precipitation, ice microphysical retrieval techniques have been developed. Sassen (1987) reviews ice microphysical retrieval techniques starting from the early 1970's, with a focus on using reflectivity (Z) to develop Z-IWC and Z-R (where R is rain rate) relations, particularly for K-band weather radar. For decades, radar reflectivity was the primary radar variable utilized for estimating IWC. A number of studies have suggested various Z-IWC relations in clouds comprised of ice and snow, including Sassen (1987); Atlas et al. (1995); Liu and Illingworth (2000); Hogan et al. (2006); Delanoe et al. (2014); Heymsfield et al. (2005, 2016) and Protat et al. (2016). Hogan et al. (2006) proposed perhaps the most widely used Z-IWC relation, with their algorithm estimating IWC using a combination of Z and atmospheric temperature T. One of the most recent studies employing a Z-IWC relation to retrieve particle information was Tian et al. (2016), which used Z alone to estimate IWC and D_m, or mean volume diameter. Relations that depend solely on radar reflectivity often struggle because such a single parameter is unable to capture the variability of the size distributions of ice and snow particles, their habits, and their densities. Simply using a single parameter to try and quantify the size, shape, orientation, density, and concentration of particles, among other properties, will fail to capture the true microphysical variability within one and across many precipitation structures.

To help rectify this problem, polarimetric radar data have shown promise for being the basis of quantitative retrievals of ice microphysical properties. As is often noted, the basic premise of polarimetric radar data is to provide further information on the size, shape, and orientation of hydrometeors within a volume beyond what limited information is offered with single-polarization radar (e.g., Zhang, 2017). However, polarimetric retrievals of ice microphysical properties remain largely unexplored. Pioneering work was done in the late 20th century performing ice microphysical retrievals using polarimetric radar data by Vivekanandan et al. (1994), who suggested using specific differential phase K_{DP} to estimate IWC. Because K_{DP} essentially depends on the particle aspect ratio and orientation whereas IWC does not (see subsection 1.3.5 for more information on K_{DP}), the use of K_{DP} requires the a priori knowledge of the particles' shapes and orientations, which is not ideal. Following the work on Vivekanandan et al. (1994), Aydin and Tang (1997) modeled ice crystals in the shapes of hexagonal columns and plates, combining K_{DP} and Z_{DR} for estimation of IWC, and producing relationships with biases and standard errors less than 5 and 15 percent, respectively.

Following the work of Vivekanandan et al. (1994) and Aydin and Tang (1997), Ryzhkov et al. (1998) developed a polarimetric relation relating IWC to K_{DP} and Z_{DP}, where Z_{DP} is defined as the reflectivity difference and is expressed as

$$Z_{DP} = Z_h - Z_v = Z_H(1 - Z_{dr}^{-1}) \tag{1.1}$$

where Z_{dr} is differential reflectivity expressed in linear scale. They found that the ratio Z_{DP}/K_{DP} is very robust with respect to the variability of the particles' aspect ratios and their orientations. This is because particle aspect ratio and orientation affect the values of Z_{DP} and K_{DP} in a similar way and, therefore, these effects are canceled out when the ratio of these two variables is used. Through testing of Eqn. 1.1 by Ryzhkov et al. (1998) and Nguyen et al. (2017), it was shown that such a relation provides significant improvement over the conventional Z-IWC method when the cloud is a mixture of small ice particles and large aggregates, with additional tuning of the polarimetric relation potentially necessary. Bukovcic et al. (2018) investigated radar snow rate estimates using Z and K_{DP}, using an extensive dataset of 2D-video-disdrometer (2DVD) measurements of snow in central Oklahoma to derive polarimetric relations for liquid-equivalent snowfall rate S and IWC in the forms of bivariate power-law relations. However, in situ validation of IWC estimates is necessitated beyond ground observations possible with the 2DVD used in the study. For validation of a given algorithm's effectiveness, the ice microphysical values retrieved by such algorithms must be compared to some measure of "truth," typically in the form of aircraft in situ measurements.

For the most exact comparison of such estimates to in situ measurements, polarimetric radar data must be collocated in time and space to the location of the in situ measurements. This poses a considerable challenge, as operational weather radar data are collected on the order of 5 minutes and over areas spanning hundreds of kilometers in diameter via plan position indicator (PPI) scans, whereas aircraft in situ measurements are often collected at frequencies at or below 1 Hz, along the very thin path the aircraft flies. To date, little has been done to directly compare operational polarimetric radar data and in situ measurements at a specific point. Finlon et al. (2016) related in situ measurements of ice particle habits, bulk cloud properties, and measurements of particle morphology to polarimetric radar data collected by an X-band dual-polarization radar within winter cyclones during the Profiling of Winter Storms (PLOWS) campaign. However, the radar was operating in range-height indicator (RHI) scanning mode when data collocation was performed, such that their methodology as it relates to radar scanning strategy is inapplicable to comparisons of in situ microphysical and operational weather radar data. This was also the case with Zrnic et al. (1993), where S-band polarimetric radar data were collected via RHI scans along with aircraft in situ data in the stratiform rain region of MCSs during the Cooperative Oklahoma P-3 Studies (COPS-89) campaign. Cazenave et al. (2016) compared aircraft in situ data to X-band radar measurements collected using PPI scans in the stratiform rain region of MCSs in the Sahel, but did so to verify a fuzzy logic technique, not to directly collocate and compare data.

Therefore, there exists a rich opportunity to use in situ microphysical measurements to validate ice microphysical retrieval algorithms optimized for S-band operational weather radar data, and gain a deeper understanding of the microphysical structure of a number of phenomena, specifically MCSs, as a result. This is the goal of this study–to utilize operational polarimetric radar data and polarimetric ice microphysical retrieval algorithms in conjunction with in situ aircraft data to gain a deeper understanding of the ice microphysical structure of MCSs, and determine the usefulness and effectiveness of such new ice microphysical retrieval algorithms and radar data processing techniques.

1.3 Radar Polarimetry

The potential benefits of radar polarimetry for enhancing understanding of meteorological phenomena have been recognized as far back as nearly seven decades. Kumjian (2013a) details some of the earliest work and advancements in radar polarimetry, dating back to the 1950's and 1960's in the United Kingdom, United States, and Soviet Union. In the late 1970's, Seliga and Bringi (1976) pioneered the first investigation into calculating rainfall rates using "differential and absolute reflectivity measurements at orthogonal polarizations," introducing to the community what is now known as differential reflectivity. Specific differential phase was then introduced by Sachidananda and Zrnic (1986, 1987), again in an attempt to calculate rainfall rate. The interest in microphysical interpretation of polarimetric radar data continued in a three-part paper by Jameson (Jameson, 1983a,b, 1985), in attempts to deduce properties of the drops in the volume. Expanding these analyses of the usefulness of dual polarization radar in inferring microphysical properties to investigations of hail, Balakrishnan and Zrnic (1990a,b) explored using polarization diversity to discriminate between regions of rain and hail. Although a non-exhaustive list at best, such work focusing on radars transmitting waves at orthogonal linear polarization (i.e., "dual-polarization" radars; Kumjian (2013a)) led to the upgrade of the National Severe Storms Laboratory's (NSSL) 10-cm S-band Doppler weather radar, or Cimarron radar, to dual-polarization capabilities as detailed in Zahrai and Zrnic (1993). The Cimarron radar measured three additional polarimetric variables, specifically "differential reflectivity, differential phase, and the correlation coefficient between copolar weather signals," beyond what was already provided by the conventional (non-polarimetric) WSR-88D radars.

Zrnic (1996) speculated on future trends and needs for radar polarimetry within the radar meteorology community, giving particular focus to the potential operational uses. He describes the significant but incremental improvements to the community's collective knowledge of radar meteorology, starting with the use of weather radar to detect precipitation echoes using radar reflectivity, and advancements including Doppler weather radar and polarimetry (Fig. 1.2). Following such extensive work investigating the uses of dual-polarization radars, Doviak et al. (2000) outlined the potential benefits of upgrading the WSR-88D radar system to have dual-polarization capabilities. With the completion of the WSR-88D radar network upgrade to dual-polarization capabilities within this decade, opportunities to further use polarimetry to study a wide variety of precipitation structures and weather systems abound. Polarimetry has been used extensively in the weather radar community since that time, including polarimetric WSR-88D data, in work including but not limited to

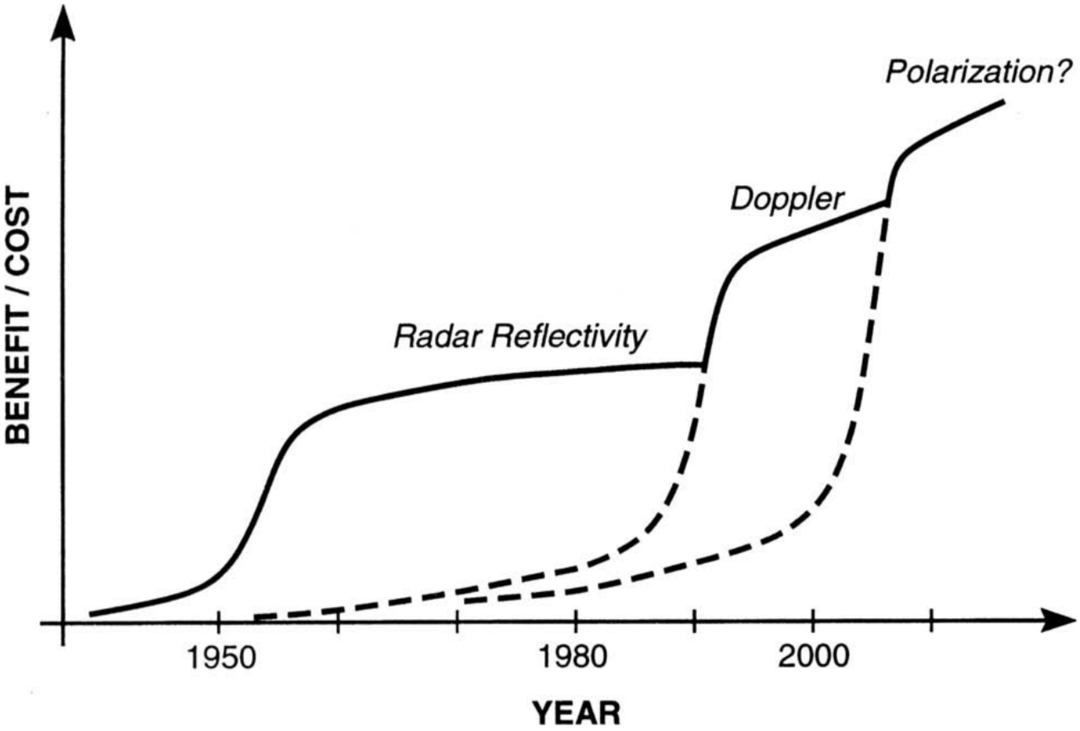

Figure 1.2: Relative benefit-cost in meteorological research and applications starting with the first use of radar. Major enhancements over reflectivity measurements are indicated. Taken from Zrnic (1996).

tornadic debris signatures (e.g., Ryzhkov et al., 2002, 2005c; Kumjian and Ryzhkov, 2008; Van Den Broeke and Jauernic, 2014; Snyder and Ryzhkov, 2015), hydrometeor classification (e.g., Zrnic and Ryzhkov, 1999; Straka et al., 2000; Zrnic et al., 2001; Heinselman and Ryzhkov, 2006; Park et al., 2009; Elmore, 2011; Snyder and Ryzhkov, 2015), and quantitative precipitation estimation (e.g., Ryzhkov and Zrnic, 1996b; Ryzhkov et al., 2005b; Giangrande and Ryzhkov, 2008).

Before transitioning to a discussion of radar data and how they have been and can be utilized to gain a deeper understanding of the stratiform rain region of MCSs, a thorough description of the polarimetric radar variables is necessitated. A large part of the discussion of polarimetric variables herein reflects the information provided in Kumjian (2013a), with that paper and the others in the series (Kumjian, 2013b,c) serving as ideal references for additional commentary on and further understanding of these radar variables, and of their uses in interpreting meteorological echoes. Ryzhkov et al. (1998, 2018); Hogan et al. (2006, 2012); Rasmussen et al. (2003); Zhang (2017); Bukovcic et al. (2018); Carlin et al. (2016) and Matrosov et al. (1996) were heavily referenced for discussions related specifically to the polarimetric variables' behavior in regions of ice and snow.

The five polarimetric radar variables of interest in this study are radar reflectivity factor (Z), differential reflectivity (Z_{DR}), co-polar cross correlation coefficient (ρ_{hv}), differential propagation phase shift (Φ_{DP}), and specific differential phase (K_{DP}). The following subsections each offer a description of these variables.

1.3.1 Radar Reflectivity Factor

Radar reflectivity factor (Z) is one of the three moments measured by conventional weather radars, with the other two being Doppler velocity and Doppler spectrum width. These moments were all previously measured at only horizontal polarization before the WSR-88D network's upgrade to dual-polarization capabilities, as the conventional WSR-88D radars only transmitted and received signals at horizontal polarizations. Although different from radar reflectivity η, radar reflectivity factor is typically referred to and will be herein referred to as radar reflectivity, or simply reflectivity.

Doviak and Zrnic (2006) define Z at horizontal polarization as

$$Z_h = \frac{4\lambda^4}{\pi^4|(\epsilon_w - 1)/(\epsilon_w + 2)|^2} < |S_{hh}|^2 > \tag{1.2}$$

where ϵ_w is the dielectric constant of water, λ is radar wavelength, and S_{hh} is the backscatter amplitude, with angular brackets denoting integration of the variable over all particles. In the case of spherical scatterers, Van de Hulst (1981) shows that simple analytical formulas can be obtained for the forward and backward scattering amplitudes $s^{(0)}_{a,b}$ and $s^{(\pi)}_{a,b}$:

$$s^{(0)}_{a,b} = s^{(\pi)}_{a,b} = \frac{\pi^2 D^3}{6\lambda^2} \frac{1}{L_{a,b} + \frac{1}{\epsilon - 1}} \tag{1.3}$$

where a is the axis of rotation of the spheroid, $D = (ab^2)^{1/3}$ is the equivolume diameter of the particle, ϵ is the dielectric constant, and L_a and L_b are shape parameters of the particle. In the case of spherical particles ($a = b$),

$$s^{(\pi)}_{a} = s^{(\pi)}_{b} = \frac{\pi^2 D^3}{2\lambda^2} \frac{\epsilon - 1}{\epsilon + 2} \tag{1.4}$$

Furthermore, if scatterers are spherical, then

$$< |S_{hh}|^2 > = < |s^{(\pi)}_{a}|^2 > = < |s^{(\pi)}_{b}|^2 > \tag{1.5}$$

and eqn. 1.2 can be written for spherical particles as

$$Z_h = \frac{< |(\epsilon - 1)/(\epsilon + 2)|^2 D^6 >}{|(\epsilon_w - 1)/(\epsilon_w + 2)|^2} \tag{1.6}$$

In the case of raindrops, $\epsilon = \epsilon_w$ and eqn. 1.6 can be simplified down to

$$Z_h = < D^6 > = \int D^6 N(D) dD \tag{1.7}$$

where N(D) is the particle number concentration. In the case of graupel and small hail, where ϵ does not change with size, eqn. 1.6 can be rewritten as

$$Z_h = \frac{|(\epsilon - 1)/(\epsilon + 2)|^2}{|\epsilon_w - 1)/(\epsilon_w + 2)|^2} \int D^6 N(D) dD \tag{1.8}$$

For frozen particles whose dielectric constants are not constant across the size spectrum of particles (such as dry snow, whose density decreases with increasing size), eqn. 1.6 can be rewritten as

$$Z_h = \frac{|K_i|^2}{|K_w|^2 \rho_i^2} \int \rho_s^2(D) D^6 N(D) dD \tag{1.9}$$

where $K_i = (\epsilon_i - 1)/(\epsilon_i + 2)$, $K_w = (\epsilon_w - 1)/(\epsilon_w + 2)$, ϵ_i is the dielectric constant of solid ice with density ρ_i, and ρ_s is the density of snow which depends on D. Knowing that ρ_s is nearly inversely proportional to particle diameter, for dry snow, Z is no longer proportional to the 6th moment of the size distribution as with rain, but rather is proportional to the 4th moment, due to how Z depends on the product of $\rho_s^2 D^6$ within the integral of eqn. 1.9. Additionally, the ratio of $|K_i|^2$ and $|K_w|^2$ is less than 1, which further explains why Z in snow is typically much less than Z in rain for volumes with comparable particle diameters and concentrations. These depressed Z values are found in almost all volumes of snow when compared to equivalent volumes of rain, except in the bright band, where large aggregates with thin water coatings produce local maximum values of Z in the vertical.

Reflectivity data are most commonly converted from their native units of $[mm^6 m^{-3}]$ to [dBZ], where

$$Z[dBZ] = 10log\left(\frac{Z[mm^6 m^{-3}]}{1[mm^6 m^{-3}]}\right) \tag{1.10}$$

Often, Z is subscripted to denote at which polarization the signal was transmitted and received, with lowercase subscripts denoting data with units of $[mm^6 m^{-3}]$, and uppercase subscripts denoting data with units of [dBZ]. Since primarily reflectivity data at horizontal polarization (Z_H) are analyzed herein, the subscript will be dropped and Z will denote reflectivity at horizontal polarization unless otherwise specified.

Because of reflectivity's relation to the 6th moment of the size distribution in rain and 4th moment in snow, measurements of Z are highly affected by the largest particles in the volume. For example, for a unit volume, the reflectivity from one wet marble sized[1] hailstone ($D = 10$ mm) is the same as the reflectivity from 100 relatively large drops ($D = 4.6$ mm). However, the total water content calculated from these two volumes will be an order of magnitude larger for the volume containing large drops compared to the volume containing the single hailstone.

Doviak et al. (2000) also noted that at the time, reflectivity was used exclusively to estimate rainfall rate R, but such equations constrain the drop size distribution to one having only a single parameter. Since, in general, the drop size distribution of a volume is only described accurately by using multiple parameters, these equations would fail to capture differences in hydrometeors between two volumes of equal reflectivity, such as in the two volumes described in detail above. Additionally, for ice, Bukovcic et al. (2018) discussed past attempts to quantify liquid water equivalent snowfall rate (S) in terms of Z, with most relations in the literature assuming a power-law relation where $Z \propto S^2$. However, as with rain size distributions, snow particle size distributions cannot be accurately quantified using only one variable, due to the variability of particles' size, shape, and orientation, to name a few. For that reason, they found that of the $Z - S$ relations in literature that they examined, there exists roughly an order of magnitude difference in estimates of S using the same Z. Estimates of IWC from Z also struggle, as was discussed in section 1.2. Reflectivity does not give any information on the shape or orientation of the particles, just the concentration and size of hydrometeors, though it is not possible to separate the contributions of size and concentration to the value of Z. These deficiencies show a

---

[1] The author recognizes that "marble sized" can be a misleading characterization of hail size, since marbles vary widely in size, but chooses to describe hail in accordance with the qualitative descriptors used by the Storm Prediction Center.

need for additional measurements and therefore additional information collected by operational weather radars.

1.3.2 Differential Reflectivity

The nature of the upgrade of the WSR-88D radar network to polarimetric capabilities is that these radars are now equipped with the technology to send and receive signals at both horizontal and vertical polarizations. This upgrade allows signals received at both horizontal and vertical polarizations to be compared quantitatively. Differential reflectivity (Z_{DR}) is defined as the logarithmic ratio of the reflectivity factors at H and V polarizations, expressed in $[dB]$:

$$Z_{DR}[dB] = Z_H - Z_V = 10log\left(\frac{Z_h}{Z_v}\right) \tag{1.11}$$

As mentioned in Kumjian (2013a), Z_{DR} was first defined and used by Seliga and Bringi (1976) for the precipitation measurements and estimation of rainfall rate. They explained that non-zero Z_{DR} in rain is a result of the oblate shape of raindrops falling at their terminal velocities. The particles become larger in the horizontal as they approach their terminal velocities, and therefore return more power at horizontal polarization than vertical, leading to a positive Z_{DR}. For that reason, it is evident that Z_{DR} is directly related to the particles' mean axis ratio within the sampling volume. For a volume of randomly oriented particles, power is returned equally at both horizontal and vertical polarizations, and $Z_{DR} = 0$ dB. Z_{DR} is independent of particle concentration, but can be affected by radar miscalibration, as miscalibration biases of Z in the two orthoganal channels are commonly different, leading to a miscalibration of Z_{DR}. It is related to the complex dielectric constant of the target, meaning that Z_{DR} values will be higher for a single raindrop than for an ice hydrometeor of the same shape and size, similar to how Z differs between an analogous raindrop and ice hydrometeor. Although Z_{DR} is concentration independent, the Z_{DR} value for a given volume will be representative of the most abundant/dominant hydrometeor shape in that volume (e.g., a low concentration of highly anisotropic hydrometeors with large Z_{DR} values can mask a large concentration of more isotropic hydrometeors).

Beyond the information it can provide about the shape and size of raindrops, Z_{DR} also provides a wealth of information about ice hydrometeors. For a given hydrometeor shape, the value of Z_{DR} is strongly dependent on the dielectric constant. For this reason, for a raindrop and snowflake of analogous shape and size, Z_{DR} will be higher for the raindrop. Z_{DR} also depends on the orientation of particles as they are falling. Magnitudes of Z_{DR} can be incredibly high for pristine ice, which can have preferred oblate (positive Z_{DR}) or prolate (negative Z_{DR}) orientations. Whereas large raindrops typically fall with their major axis oriented vertically, producing positive Z_{DR}, snowflakes often fall in a more random and chaotic fashion, where the absence of a preferred orientation decreases Z_{DR}. After the onset of aggregation, large aggregates typically have a very low density, further decreasing Z_{DR}, as it is linearly proportional to the density of dry snow ρ_s (Kumjian, 2013a).

Because Z_{DR} is dependent both on particle axis ratio and density, it can be used to infer the relative concentrations of isotropic and anisotropic ice particles within a volume. Small ice hydrometeors produced at levels colder than the DGL are comparatively more isotropic than those produced within the DGL, and thus produce low values of (still positive) Z_{DR}. Within and just below the DGL, the dendrites in this region are highly anisotropic (oblate) and quite dense, such that they can have very high Z_{DR} values, as high as 6-10 dB. Below the DGL and above the ML, individual ice hydrometeors begin to aggregate, and the radar sample volumes start to be dominated by isotropic, low-density aggregates. For this reason, Z_{DR} is near zero above the ML, usually around 0.2-0.25 dB (Ryzhkov and Zrnic, 1998; Ryzhkov et al., 2005a). This is correlated with an increase in Z_H in this region, as the particles are becoming larger as they descend towards the top of the ML. Strong Z_{DR} signatures in the DGL were observed by Griffin et al. (2018) in their work exploring polarimetric signatures in winter storms, as well as in Andric et al. (2013) and Williams et al. (2015). Such signatures may be absent, however, if the volume sampled by the radar remains dominated by small, quasi-isometric ice hydrometeors falling into the DGL from aloft, or if dendrites do not exist within the DGL. In the former case, the polarimetric signature expected of the anisotropic dendrites (i.e., high Z_{DR}) is masked by the presence of the much more abundant isometric ice.

1.3.3 Co-Polar Cross Correlation Coefficient

Whereas Z_{DR} provides information on the shape and orientation of the most dominant particle type in a sampling volume, co-polar cross correlation coefficient (ρ_{hv}; henceforth referred to as correlation coefficient) gives information about the diversity of particles within the sampling volume. As stated by Kumjian (2013a), "ρ_{hv} is a measure of the diversity of how each scatterer in the sampling volume contributes to the overall H- and V-polarization signals. This diversity includes any physical characteristic of the scatterers that affects the returned signal amplitude and phase. Thus, when there exists a large variety in the types, shapes, and/or orientation of particles within the radar sampling volume, [ρ_{hv}] is decreased." A volume containing scatters of nearly analogous type (i.e., complex dielectric constant), shape, and orientation will return values of ρ_{hv} near unity; any deviation from this uniformity decreases the value. Particle size does not necessarily have to be uniform, unless the values of the other three aforementioned particle characteristics change across the size spectrum. ρ_{hv} is independent of particle concentration and is immune to radar miscalibration, attenuation or differential attenuation, and beam blockage.

Values of ρ_{hv} in pure rain are near unity ($\rho_{hv} > 0.98$) at S and X bands, but may drop down to values closer to 0.9 at C band due to the effects of resonance scattering (occurs with drop sizes of 5-7 mm at C band; e.g. Carey and Petersen, 2015). Values are also high for dry snow aggregates ($\rho_{hv} > 0.97$) since their low density counteracts the effects of shape irregularity and increased wobbling, and in pristine ice ($\rho_{hv} > 0.96$). The slight reduction in ρ_{hv} possible for pristine ice is due to high anisotropy and lack of preferred crystal orientation giving the appearance of a higher diversity of particle shapes in the sampling volume (i.e., a dendrite with a canting angle of 0° will return power differently than a dendrite with a canting angle of 40°). When ice hydrometeors melt, a reduction of ρ_{hv} is often seen (< 0.90) due to the addition of liquid meltwater on the particles contributing to a larger complex dielectric constant, exaggerating any pre-existing variability in particle shapes and orientations (Kumjian, 2013a).

1.3.4 Differential Propagation Phase Shift

As the H- and V-polarized waves travel through various media in the atmosphere, the speed of each of the waves is affected by the type of medium they travel through. In any medium other than a vacuum, the speed of each wave will be slower than that of the speed of light, with waves traveling through ice or water more slowly than those traveling through air. When a polarized wave encounters a hydrometeor, if the horizontal and vertical dimensions of the particle are different, one wave (i.e., either the H- or V- polarized wave) will travel a longer path through the particle than the other. This means that that wave will travel at a lower rate of speed for a longer time than the other, producing a phase shift between the two waves. This phase shift will be greater the greater the difference between the hydrometeors' horizontal and vertical dimensions, and the higher the concentration of particles the waves pass through. This concept is the premise of differential propagation phase shift (Φ_{DP}), hereafter simply differential phase. Positive is defined as depolarization resulting from the H-wave being slowed compared to the V-wave, and commonly, differential phase is always positive with a few exceptions (e.g., in the presence of vertically oriented crystals due to strong electrostatic fields in thunderstorms).

As previously mentioned, Φ_{DP} is related to the axis ratio of the particle (and therefore often the particle size, as larger raindrops tend to be more oblate in size), and the number concentration of the particles in the volume. The same applies for ice hydrometeors; however, particle shape is not as directly related to particle size, as small pristine ice crystals can produce much higher Φ_{DP} than large, isotropic aggregates. Therefore, particle orientation has a large impact on Φ_{DP}, especially for ice particles. As a phase measurement, Φ_{DP} is attractive to use in a number of capacities because it is not affected by attenuation, partial beam blockage, or radar miscalibration, and is not biased by noise. This measurement is not often used operationally and is used less so in research compared to its counterpart specific differential phase (K_{DP}), which is explained in the next section.

1.3.5 Specific Differential Phase

A polarimetric variable derived from differential phase, specific differential phase (K_{DP}) is half the range derivative of Φ_{DP}, and therefore a quantity which "provides a measure of the amount of differential phase shift per unit distance (usually given in units of degrees per kilometer) along the radial direction" (Kumjian, 2013a). Because it is derived from Φ_{DP}, K_{DP} is also related to particle axis ratio and concentration, and is immune to attenuation, partial beam blockage, radar miscalibration, and biases from noise. Whereas Φ_{DP} values typically remain constant or increase downradial, showing the total effect of phase shift as the polarized waves propagate, K_{DP} shows the effect of phase shift at each range gate. To determine K_{DP}, a slope of the radial dependance of Φ_{DP} is determined over the range windows of 17 or 49 gates as a linear fit, depending on whether or not Z_H is greater than (17) or less than or equal to (49) 40 dBZ (Ryzhkov and Zrnic, 1996a; Ryzhkov et al., 2000).

Because K_{DP} is related to hydrometeor concentration, it has proven itself to be particularly useful in liquid water content (e.g., Doviak and Zrnic, 2006; Bringi and

Chandrasekar, 2001) and ice water content estimation (e.g., Vivekanandan et al., 1994; Ryzhkov et al., 1998; Bukovcic et al., 2018). However, relations using K_{DP} can suffer from the inherent noisiness of the variable (e.g., Kumjian, 2013a). While a big advantage of K_{DP} is that it is not biased by noise, attenuation, or radar miscalibration, the magnitude of K_{DP} in ice and snow is relatively small, particularly at longer radar wavelengths, so any noisiness of the variable is even more impactful in microphysical calculations using K_{DP} in ice. At S band, K_{DP} in dry ice and snow is usually smaller than 0.3 and typical values are below 0.05 deg/km in aggregated snow at warmer temperatures (Ryzhkov and Zrnic, 1998; Griffin et al., 2018).

Normalized values of K_{DP}, or the ratio of K_{DP} for monodispersed size distribution with equivolume diameter D to the total concentration of raindrops, for frozen precipitation such as dry graupel and small hail are about two orders of magnitude less than normalized K_{DP} values for raindrops of a similar size (Ryzhkov et al., 2013). This reduction of K_{DP} facilitates easier identification of regions of frozen hydrometeors among rain. It can be shown that, for dry aggregated snow, $K_{DP} \propto \rho_s^2 D^3$. Knowing that ρ_s is inversely proportional to particle diameter for snow, this means that K_{DP} is proportional to the 1st moment of the snow size distribution (i.e., the mean diameter of particles in the volume; Bukovcic et al., 2018, see their eqn. A25). This means that K_{DP} for dry aggregated snow is typically quite low compared to rain, where it is proportional to the 3rd moment of the size distribution. However, for high density pristine crystals (such as plates, columns, and dendrites), K_{DP} is close to the 3rd moment of the size distribution (Bukovcic et al., 2018) and can be quite large. This is a result of these crystals' high density, very high or low aspect ratio, and typically quite common alignment (e.g., Kumjian, 2013a, and references therein).

In regions of ice hydrometeors, Z_{DR} and K_{DP} can be used in conjunction to qualitatively determine the dominant ice hydrometeor type or particle habit within the region. For regions of spherical ice particle or aggregates, values of Z_{DR} will be low due to the nearly isotropic shape of the particles, but K_{DP} can still be high due to the large concentration of such particles. Conversely, in regions of pristine ice crystals such as dendrites, Z_{DR} can be quite high due to their anisotropy, but K_{DP} can remain fairly low due to the low concentration of particles. Griffin et al. (2018) noted this apparent anticorrelation of Z_{DR} and K_{DP} magnitudes in the DGL within a number of winter storms, attributing the signatures to the depth of the cloud and relative impact of seeding of ice particles into the DGL from aloft. Such signatures and other "polarimetric fingerprints" (Kumjian, 2012) can prove helpful in qualitatively understanding the dominant hydrometeor type and microphysical structure of varying precipitation systems.

1.4 Quasi-Vertical Profiles (QVPs)

Quasi-vertical profiles, or QVPs, have emerged as a novel way to view polarimetric radar data in a time-height format. These plots are created by taking radar data from PPI scans and processing it such that data collected at a single elevation angle are displayed as one vertical column. The elevation angle is typically chosen as the highest elevation angle scanned in one radar volume scan, with available elevation angles contingent on the scanning strategy used. Such plots facilitate more direct comparison of radar data to various meteorological data collected in a time-height format, such as aircraft microphysical data.

The idea was first posed in Troemel et al. (2013), where quasi-vertical profiles of Z, Z_{DR}, ρ_{hv}, and Φ_{DP} were created from PPI scans performed by JuXPol, a dual-polarization X-band radar in Julich, Germany. These analyses were one-dimensional in nature, as they analyzed data from a single elevation from only one volume scan, giving information only in the range (height) dimension and no information regarding temporal evolution of the system. Such analyses using these one-dimensional QVPs

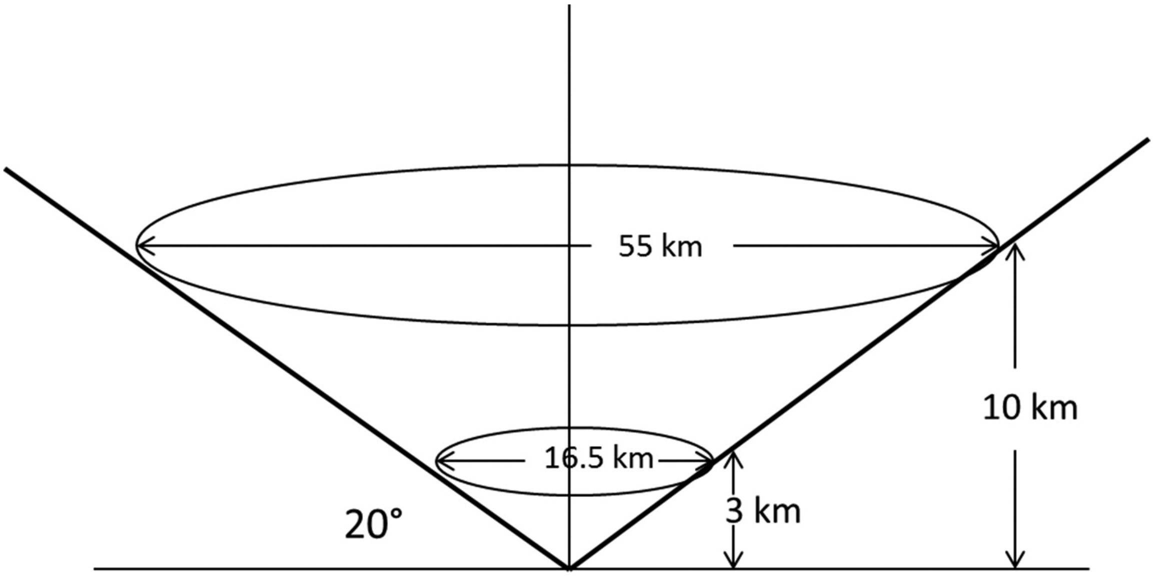

Figure 1.3: Conical volume representing azimuthally averaged quasi-vertical profiles of radar variables. Taken from Ryzhkov et al. (2016).

were used primarily to propose new methods for estimating backscatter differential phase δ in rain and in the melting layer. Kumjian et al. (2013) also employed the use of such profiles to analyze instances of hydrometeor refreezing in winter storms observed by a dual-polarization WSR-88D S-band radar and dual-polarization C-band radar in central Oklahoma. Similar to Troemel et al. (2013), this study created such profiles at a specific time using data from a single elevation angle scanned during one volume scan. Such one-dimensional profiles are useful in observing polarimetric signatures in precipitation at a given time, but are unable to diagnose any evolution of polarimetric signatures in time.

Ryzhkov et al. (2016) expanded on these initial analyses to create a QVP that spans over a specific length of time, allowing for analyses of the evolution of polarimetric signatures that were absent in earlier studies. Such two-dimensional QVPs (henceforth simply QVPs) are created analogously to one-dimensional QVPs, using data from one elevation scan typically between 10-20° in elevation. However, these profiles differ in that they use multiple scans at the chosen elevation, extracted from

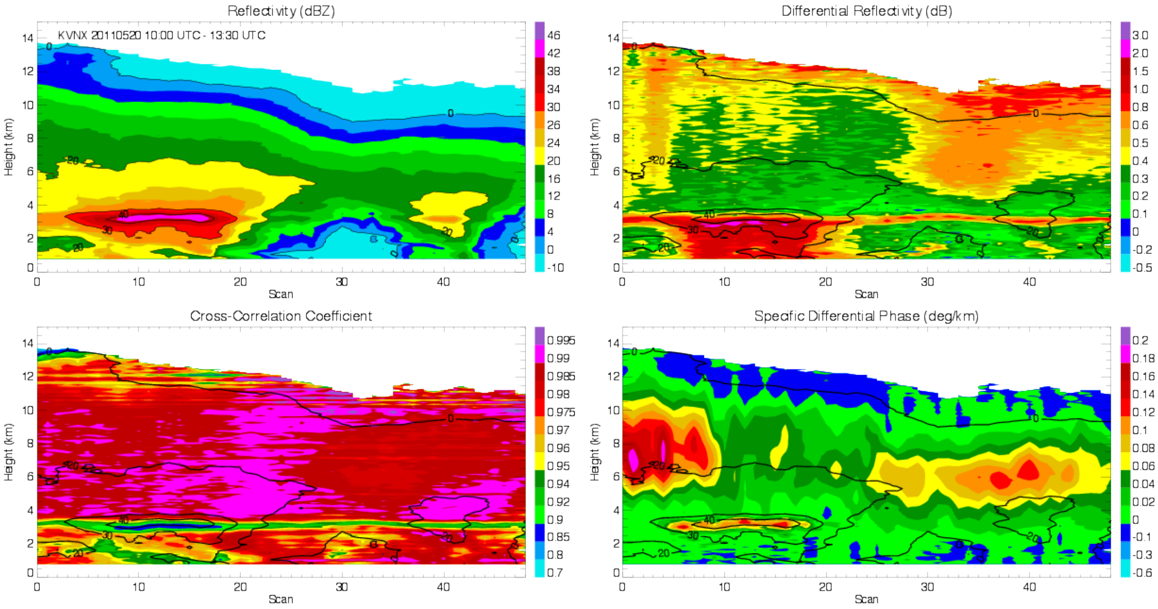

Figure 1.4: The height-vs-time representation of quasi-vertical profiles of (a) Z, (b) Z_{DR}, (c) ρ_{hv}, and (d) K_{DP} retrieved from the KVNX WSR-88D radar. Data shown were collected at elevation 19.5° in the case of an MCS observed in northern Oklahoma on 20 May 2011 from 10:00-13:30 UTC. Overlaid are contours of Z.

successive volume scans. The processing of data for QVPs, both one-dimensional and two-dimensional, is fairly straightforward. As the beam goes out in distance from the radar, it also increases in height due to expected beam propagation with a typical atmospheric refractivity, such that radar data collected at ranges further from the radar are located higher in the vertical than data closer to the radar. Therefore, data at a given range are assigned a corresponding height to be used in plotting. To filter out spurious data, QVPs exclude data points where $Z < -10$ dBZ and/or $\rho_{hv} < 0.8$. Additionally, extra heterogeneity checks are implemented with regards to Φ_{DP}. For each radial, a five-point running mean of Φ_{DP} is performed three times. That thrice-averaged radial profile of Φ_{DP} is considered the average value in calculations of the standard deviation of Φ_{DP} at each range gate along each radial, calculated over a five-point interval surrounding the point in question. Data points where the standard deviation of Φ_{DP} is greater than 10° are excluded from the QVP calculation.

Data that were not filtered by aforementioned techniques at all distances in range are averaged over the full 360° of the elevation scan, and those average polarimetric radar data at each range gate are plotted at the altitude that correlates to that distance in range. Fig. 1.3 shows a conical volume representing azimuthally averaged quasi-vertical profiles of radar variables. This data averaging is particularly advantageous for examining K_{DP}, as such averaging helps to smooth out the variable's inherent noisiness. Fig. 1.4 shows a QVP of an MCS passing over the Vance Air Force Base, OK (KVNX) WSR-88D radar in north central Oklahoma on May 20, 2011. It is clear that QVPs provide a unique insight into and opportunity to gain a deeper understanding of the vertical structure of various precipitation systems, including MCSs, beyond what is offered by the data in its traditional plan-position indicator (PPI) format.

In addition to the four standard dual-polarization variables plotted in QVPs (Z, Z_{DR}, ρ_{hv}, and Φ_{DP}), QVPs can also be made for K_{DP} as explained in Griffin et al.

(2018) and shown in Fig. 1.4, with appropriate special processing due to strong contribution of δ to Φ_{DP} in the melting layer (see also Troemel et al., 2014). For cases where the radar experienced a Z_{DR} bias, QVPs of Z_{DR} are manually calibrated such that values just above the ML are approximately 0.2-0.25 dB (Ryzhkov and Zrnic, 1998; Ryzhkov et al., 2005a). QVPs have been used in a number of studies to connect observed or modeled microphysical processes with what is observed by radar (e.g., Van Den Broeke et al., 2017; Bukovcic et al., 2017; Kumjian and Lombardo, 2017; Sulia and Kumjian, 2017; Ryzhkov et al., 2017; Troemel et al., 2017). Analyses to date have mainly focused on using the QVP technique with S-band radar data, typically from the WSR-88D S-band radar network in the United States (Crum and Alberty, 1993).

Chapter 2

Column-Vertical Profile (CVP) Methodology

2.1 Motivation

The development of the QVP technique has led to a number of studies mentioned previously investigating the microphysical properties and processes within different meteorological phenomena. However, one main drawback of QVPs is that they assume a degree of horizontal homogeneity in the sampled precipitation, as data are averaged over the full range and azimuth sampled by the radar (Ryzhkov et al., 2016). Therefore, QVPs struggle with accurately representing phenomena with considerable heterogeneities across the area sampled by the radar. For systems such as MCSs, this broad-brush azimuthal averaging of data has the potential to blur together polarimetric signatures from distinct precipitation substructures such as the leading convective line and trailing stratiform region. Fig. 2.1 shows the evolution of an MCS as it passed through the KVNX radar domain in north central Oklahoma from 13-17 UTC on May 20, 2011. It is clear that various precipitation structures, including leading line convection and trailing stratiform, are present, such that azimuthal averaging of the data over the entire 360° surrounding the radar would likely blur together distinct polarimetric signatures from the various precipitation substructures, making polarimetric analyses of such substructures difficult if not impossible.

For this reason, a more tailored method of processing operational polarimetric radar data to be viewed in a time-height format is necessitated. This method should restrict data sourcing to a specific region in the horizontal, allowing the user to select specific precipitation substructures of interest to analyze, and removing the effects of azimuthally averaging data from various precipitation substructures within the horizontal area sampled by the radar. For such an approach, using a single elevation

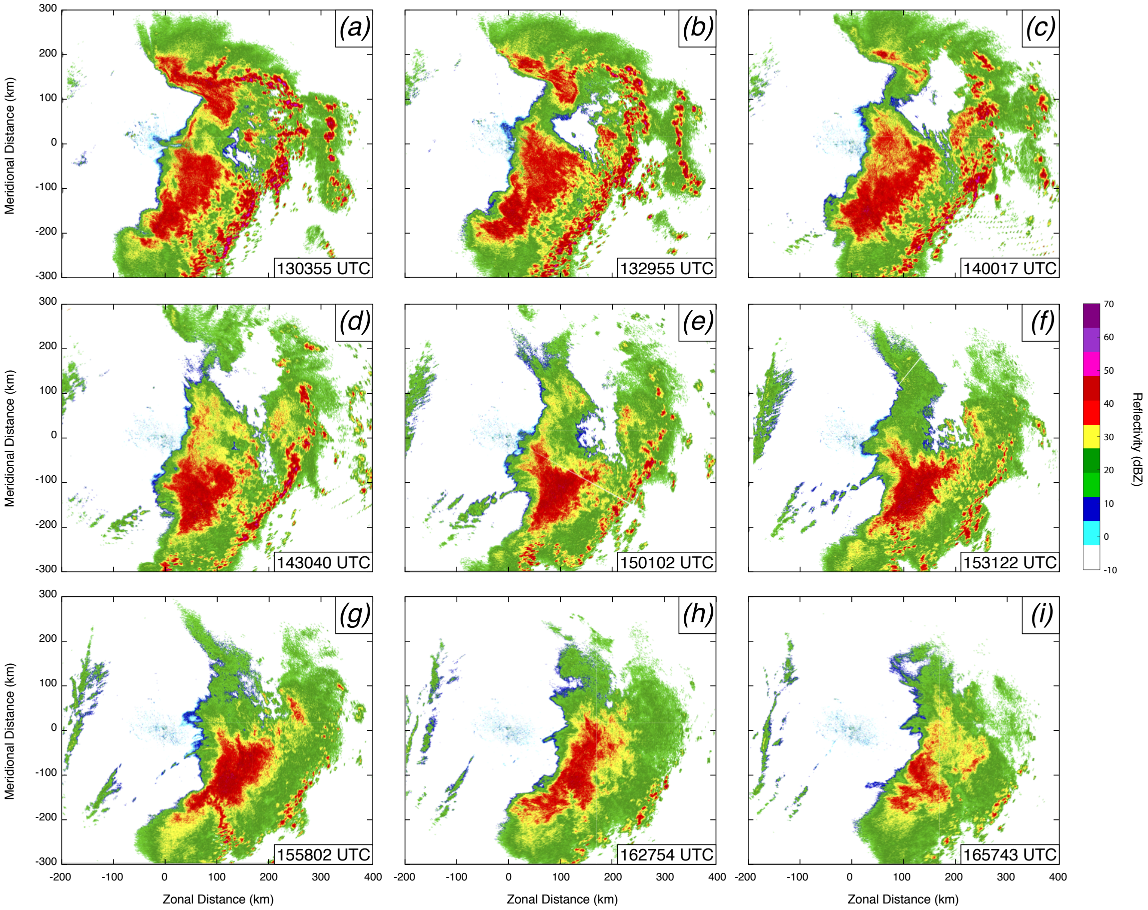

Figure 2.1: PPI images of radar reflectivity (dBZ) collected at the 0.5 degree elevation angle by the KVNX radar from 13-17 UTC. Images were selected at approximately half-hour intervals, with time increasing alphabetically and specific times of data collection listed in each panel.

angle is no longer feasible, since by limiting the radial extent of the region from which data will be sourced, one single elevation angle will capture a very limited extent in height.

Attempts at modifying the original QVP technique and using such modified techniques to construct vertical profiles of polarimetric variables have been made in recent studies. Bukovcic et al. (2017) employed the use of slanted vertical profiles (SVPs) to analyze data over a disdrometer site to compare to disdrometer ice microphysical measurements. A SVP is created using data from one elevation angle at a specific azimuth, with the azimuth chosen as the one whose radar beam most closely passes over the point of interest on the ground (in the case of Bukovcic et al. (2017), the disdrometer). A pair of ranges and azimuths are defined such that the point of interest is roughly centered between the beginning and ending range and azimuth, respectively. Then, all data between the beginning and ending azimuths are averaged azimuthally along the entire radial extent between the beginning and ending range. After producing this radial profile of the polarimetric variable in question, the data are then projected on their native horizontal planes to the point of interest, producing a vertical profile of radar data over that point. The authors state that the typical range interval is up to 60 km and azimuthal interval is up to 20°.

Such a profile provides useful data if analyses are restricted to a small vertical extent, as was done in Bukovcic et al. (2017). However, as they mention, “the data over such large-range intervals are likely inhomogeneous; hence, interpretation needs to be very cautious.” Because of the large radial extent of the SVP, it is likely that the profile can be sampling remarkably different precipitation substructures as the beam propagates further from the radar within the prescribed radial extent (e.g., sampling the leading convective line of an MCS closer to the radar and trailing stratiform region further from the radar). The potential for sampling profoundly different precipitation structures with radius and interpolating those data to a single vertical profile is problematic for situations where interest is in representing and analyzing the entire depth of the vertical profile for a single prescribed location.

In addition, Bukovcic et al. (2017) proposed and used another technique, namely that of enhanced vertical profiles (EVPs). This profile is initially different from the SVP technique because it uses all available elevation angles. Starting 2.5 km upradial from the point of interest, the median of all data spanning three azimuths and five range gates from that point is taken. This is done for each point in range up to 2.5 km downradial of the point of interest. Those median values are then projected from all elevations to the vertical, much like the SVP, to create a vertical profile over the point of interest.

This technique produces a more representative profile of polarimetric radar data over a given point, since data are sourced from a much more restricted extent in range. However, due to the inherent noisiness of polarimetric variables, especially K_{DP} (e.g., Kumjian, 2013a), using the median value of data around a single point may struggle to eliminate noise, since data are not smoothed in any direct way. Additionally, the limited azimuthal extent, even if mean values were used instead of median, may allow for noise to still greatly influence the final values in the EVP.

A third modification on the original QVP technique was proposed by Tobin and Kumjian (2017). They suggested the use of a "range-defined" QVP to examine the occurrence and evolution of refreezing signatures during transitions from ice pellets to freezing rain. They were motivated to modify the QVP technique since it censors the first eight 250-m range gates, which can "partially or fully mask low-level ($<$ 1 km) signatures such as refreezing when using higher elevation angles," such as the 10-20° elevation angles typically used to construct QVPs. Range-defined QVPs use data from all available elevation angles, defining a set range from the radar within which the data will be used. QVPs are then created for all available elevation angles within that restricted range from the radar, and those data are all interpolated to a

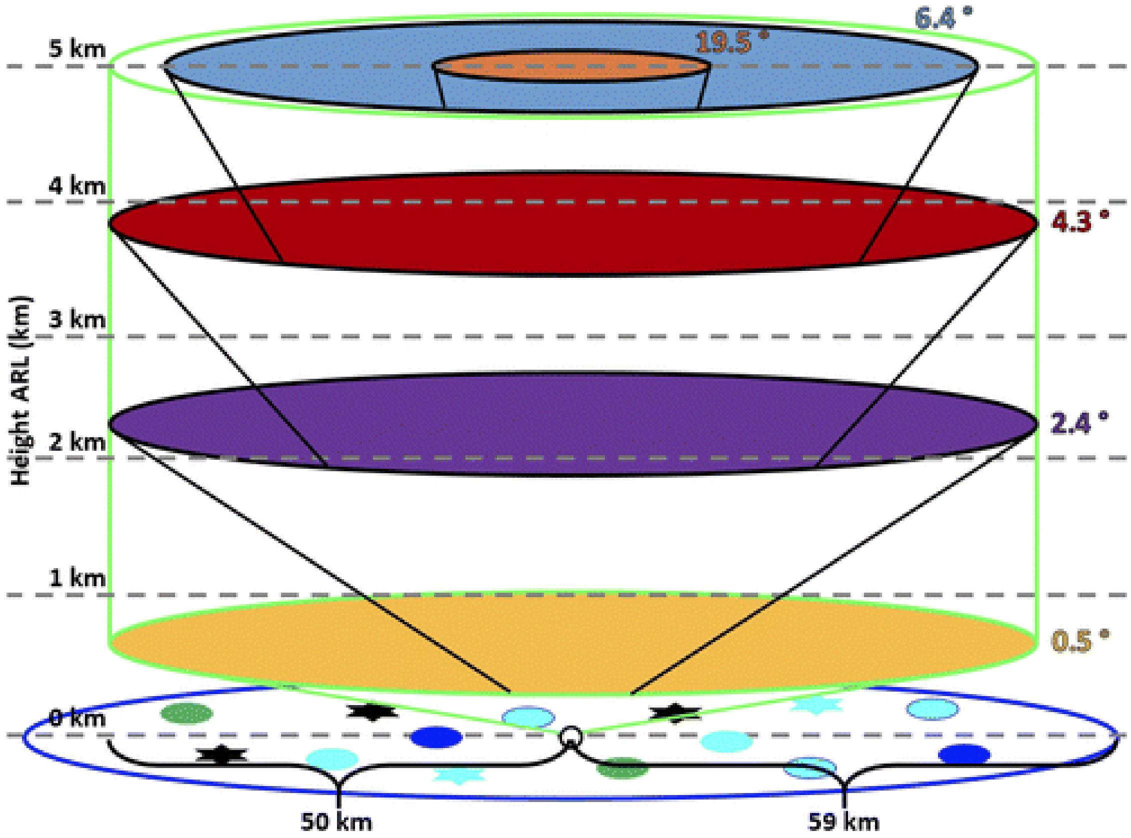

Figure 2.2: Diagram explaining computation of the range-defined QVP and its interpretation. Additional details available within and figure taken from Tobin and Kumjian (2017).

common vertical axis with 2-m resolution. These data are interpolated to such a fine vertical grid by employing an inverse distance weighting technique, with the ability to tune the technique to weight the output more and more heavily to the value closest to the desired location in the vertical. Fig. 2.2 provides a conceptual depiction of the range-defined QVP geometry.

This technique works well for the identification and monitoring of temporally-evolving refreezing signatures, as it provides rich data near the ground surrounding the radar. However, this technique does not allow for specific tailoring of the analysis location as in Bukovcic et al. (2017), as the technique still produces a radar-centric vertical profile as in the original Ryzhkov et al. (2016) QVP technique. The authors noted this limitation of being radar-centric, stating that, "in principle, one could also define two azimuths and two ranges to isolate a particular location.... This may be especially useful in cases of spatially heterogeneous or widely scattered precipitation."

2.2 Description of Technique

To further tailor the QVP technique to analyze more limited areas in the horizontal within a large region sampled by a radar, the column-vertical profile, or CVP, technique was developed (Murphy et al., 2018). Similar to QVPs, CVPs offer novel insight into the microphysical properties of various meteorological phenomena by providing a simple and effective way to process polarimetric data and view it in a time-height format. Whereas QVPs average radar data over the full range and azimuth of one radar elevation scan, CVPs average data within a set sector in range and azimuth and using multiple radar elevation scans performed during one volume scan. CVP data analysis begins with selecting a specific location in range and azimuth from the radar where the CVP will be centered. Next, a sector over which data will be sourced is chosen, defined by a given distance upradial and downradial, and azimuth clockwise and counterclockwise from the center point of the CVP analysis. Often this sector spans 20 km in range and 20° in azimuth—specifically, 10 km up and downradial, and 10° clockwise and counterclockwise from the CVP center. This is the sector size used within all analyses shown herein. Fig. 2.3 shows a plan view of an arbitrary CVP sector, spanning 20 km in range and 20° in azimuth.

For CVPs, because only data collected within a designated sector are included in data processing and not data from every range gate and across all 360° in azimuth, a single elevation scan cannot provide enough data to construct a full vertical profile. Therefore, multiple elevation angles must be used to create the CVP. To create a CVP, first a full volume scan is performed, and data that are collected from each elevation scan within the analysis sector are averaged azimuthally. The averaged data, existing at various distances along the radial (and therefore varying heights), are projected along the horizontal to the center location of the CVP. The result is that all data are located at varying heights at the same horizontal location in radius and azimuth from the radar—namely, at the CVP center. This initial averaging and projection of data from three dimensions to one dimension is done for each elevation angle and without any weighting of data. Since volume scans are performed on the order of 5 minutes, the times at which the data that are averaged and projected to the CVP center are collected vary on the order of 5 minutes.

If two subsequent elevation scans have a sufficiently small elevation angle difference and the range over which the CVP sector spans is sufficiently large, both elevation scans may collect data at the same height within the analysis sector, leading to data overlap when projected to the CVP center. To prevent overlap in projected data from two subsequent elevation scans, for a given elevation angle, intermediate elevation angles are defined as (imaginary) elevation scans inbetween the given elevation angle and the elevation angles directly above and below (e.g., if a radar had elevation scans at 0.5°, 1.5°, and 2.4°, the intermediate elevation angles for the 1.5° elevation scan would be 1.0° and 1.95°). A restriction is placed such that data cannot be projected

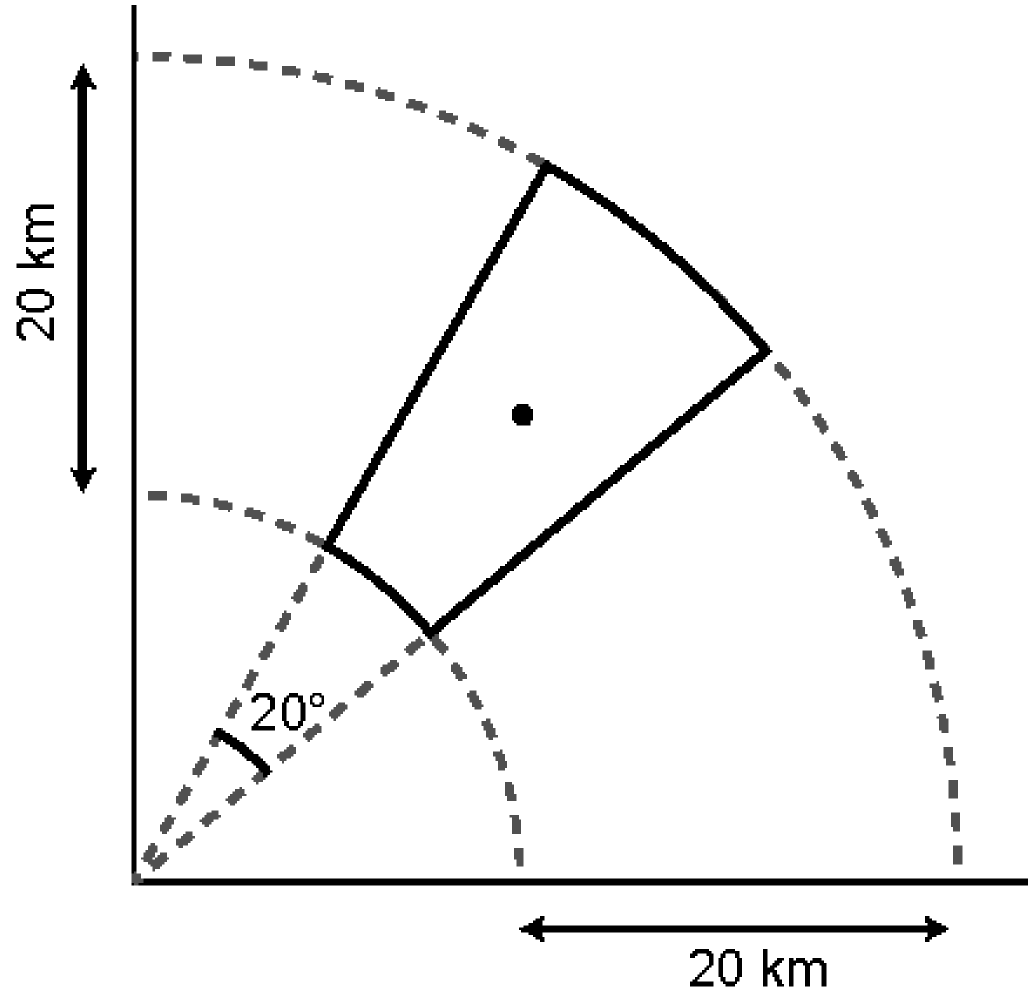

Figure 2.3: Plan view of a CVP sector (outlined in solid lines), spanning 20 km in range and 20° in azimuth. The CVP center is represented by a dot in the middle of the sector.

in the vertical to the CVP center from that elevation scan at heights below the height of the lower intermediate elevation angle at the CVP center, or above the height of the higher intermediate elevation angle at the CVP center. Fig. 2.4 shows how data from subsequent elevation scans are projected to the CVP center, including limits on projection placed by intermediate elevation angles. This ensures data that are collected closer are preferred over data collected farther from the CVP center in range.

Once projected in the vertical dimension to the location of the CVP center, the data are not regularly spaced in height, as an increase in the slope of the radar beam as the radar scans higher in elevation creates a decrease in data density in the vertical with height (see Fig. 2.4). To create a distribution of data in the vertical that are evenly spaced with height, a Cressman averaging technique is employed (Cressman, 1959). This technique creates an evenly spaced array of data in the vertical by searching for all data within a specified vertical distance from a given height, and interpolating those data to that height via weighted averaging. This invokes the use of a Cressman radius of influence, or how far away in the vertical from the specified vertical location the algorithm will search for data to interpolate to that location. A Cressman radius of influence of 100 m is typically used, meaning that the algorithm will search vertically up and down 100 m for data to interpolate to a given height. While the Cressman averaging technique and weighted interpolation of data to a regular grid often fills data gaps due to its averaging in the vertical, it can still allow for gaps in data if, for a given vertical location, there are no radar data within the vertical distance of the Cressman radius of influence above or below that location. Cressman averaging is typically done every 50 m from 0 to 15 km, resulting in vertical profiles with data spacing of 50 m in the vertical. The distance from the radar at which a CVP begins to have these gaps depends on the choice of the Cressman radius of influence, the radar scanning strategy, and the range over which the CVP sector

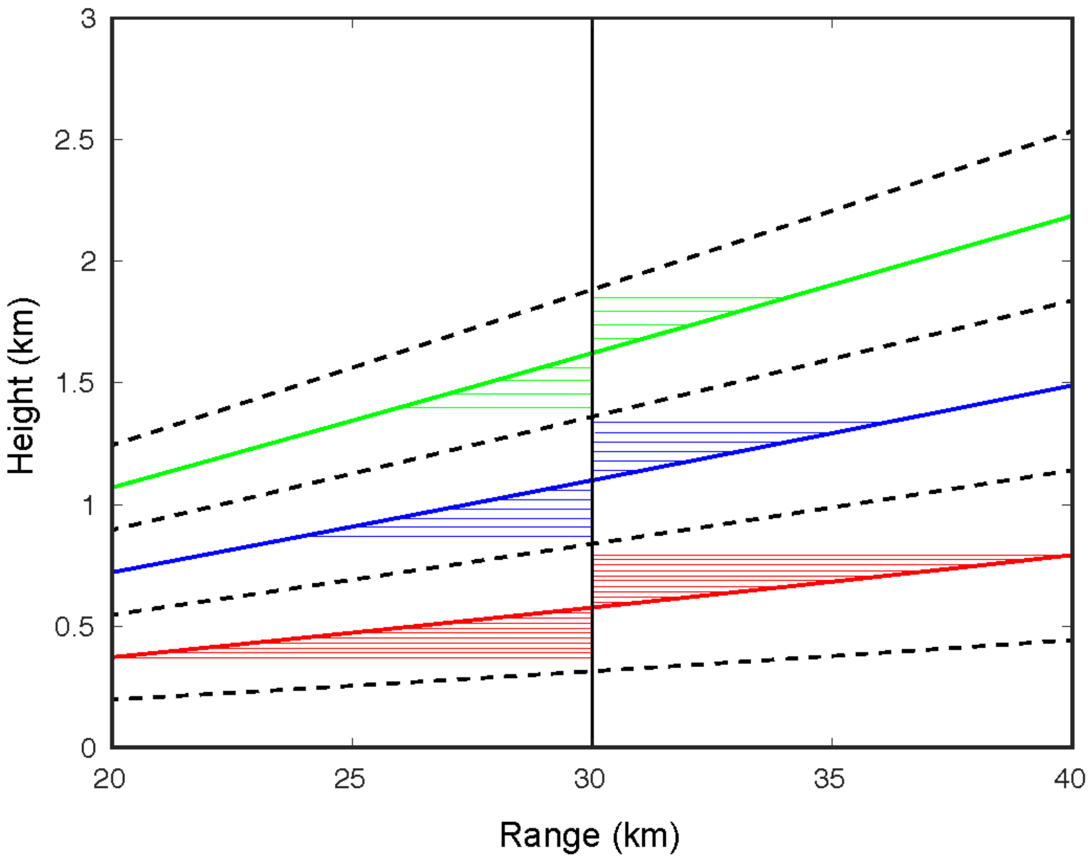

Figure 2.4: Visualization of how data are projected from different elevation angles to the CVP center. Darker lines represent data collected at 1° (red), 2° (blue), and 3° (green) elevations, and lighter lines represent the native horizontal planes on which the data are interpolated. Dashed lines represent intermediate elevation angles of 1.5° and 2.5°. For visual simplicity, the figure suggests data are collected at 1 km range resolution; WSR-88D data are actually collected at 250 m range resolution.

spans. CVPs can typically be created at a range less than or equal to 110 km from the radar when dealing with S-band radar data. Further investigation needs to be done to determine the maximum distance in range from the radar CVPs can be created with radars of different wavelengths. As with QVPs, for cases where the radar experienced a Z_{DR} bias, CVPs of Z_{DR} are manually calibrated such that values just above the ML are approximately 0.2-0.25 dB (Ryzhkov and Zrnic, 1998; Ryzhkov et al., 2005a).

The focusing of CVPs on a single location allows for tailoring of data selection and processing to a unique feature or area of interest. As mentioned previously, QVPs assume a certain degree of horizontal homogeneity in the observed precipitation (Ryzhkov et al., 2016). While this can be appropriate for some analyses, for applications such as comparison of polarimetric radar data to aircraft data, QVPs can smooth out small mesoscale features that can lead to distinct microphysical characteristics observable by the aircraft. For this reason, for intricate comparison of polarimetric radar data to aircraft microphysical data, the detail offered by CVPs is imperative. Fig. 2.5 shows a QVP and a CVP of Z from the same radar, date, and time as in Fig. 1.4. During this time, an MCS was in the vicinity of the radar and passed through the CVP's analysis sector. Whereas in the QVP it is relatively unclear what type of precipitating system is being sampled by the radar, in the CVP, one can clearly pick out the leading convective line, transition zone, and trailing stratiform region (e.g., Houze et al., 1989) of an MCS.

2.3 Modifications for Moving CVPs

The primary advantage of CVPs over QVPs is the ability to tailor the vertical profile the technique creates to a specific location in range and azimuth from the radar. This allows for analyses of polarimetric radar signatures and their trends over a specific area, which could prove useful for a number of applications, including for comparing aircraft microphysical data to polarimetric radar data, as will be the focus

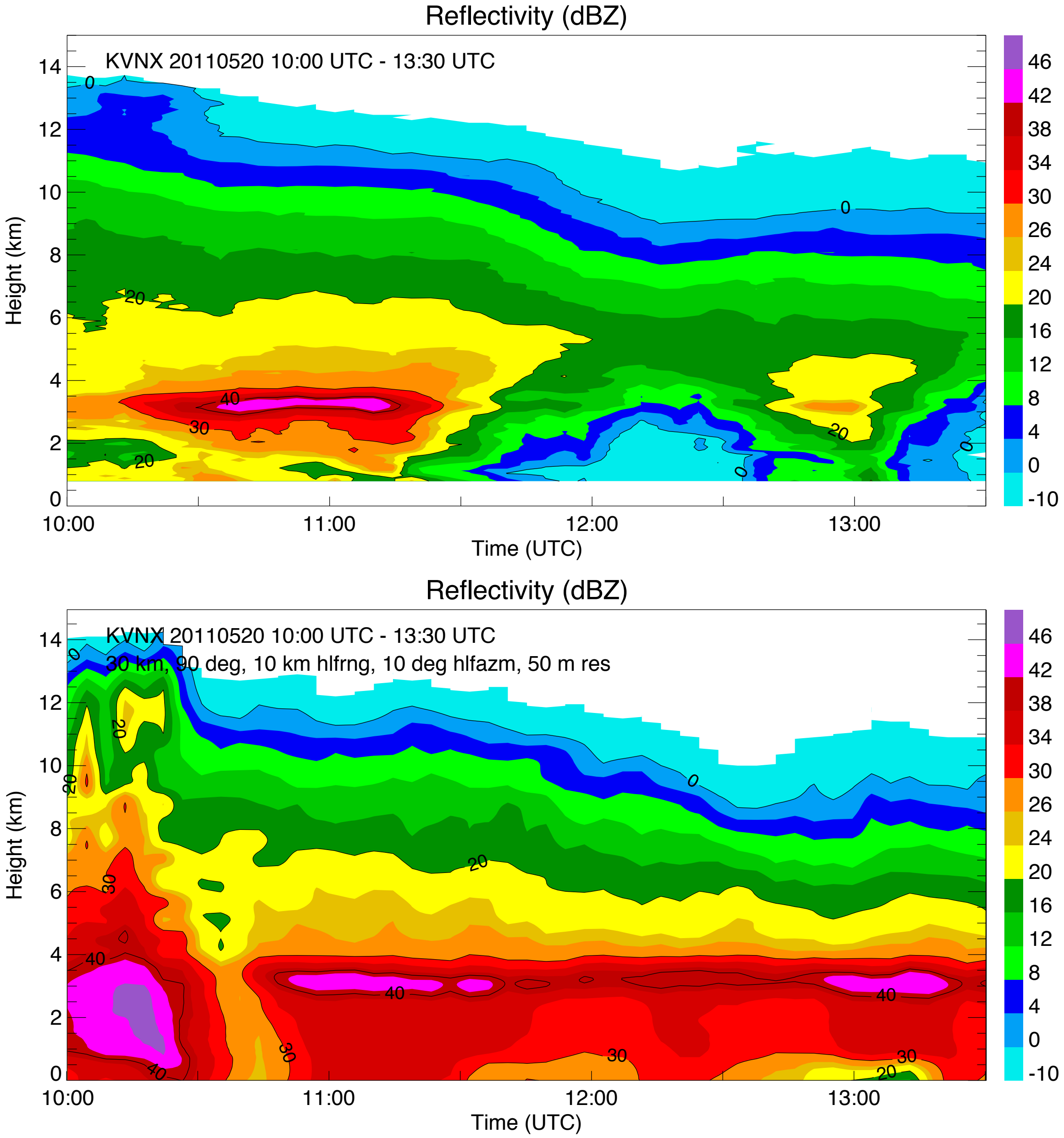

Figure 2.5: QVP (top) and CVP (bottom) of reflectivity for the same MCS case and time as Fig. 1.4. The CVP is centered at 30 km and 90° from the radar, vertical data spacing in the CVP is 50 m, and the sector size is 20 km in range and 20° in azimuth.

herein. Using the same methodology for creating a CVP at a fixed location, CVPs can be created such that the CVP is centered on a different location for every single volume scan. This moving CVP has the same sector size in range and azimuth for every scan, the same vertical data spacing, and the same Cressman radius of influence for each volume scan, and differs only in the location on which it is centered. This technique can be used as a first step in collocating polarimetric radar and in situ aircraft data by having the CVP move roughly in conjunction with the aircraft. Fig. 2.6 shows a conceptual model of how a CVP can be made to move in time with the aircraft. The upper panel shows a 3-D model of an aircraft moving in time, with different colored columns representing the location of the CVP sector and the column from which data were sourced to create a CVP at that time and volume scan. The lower panel shows how these data, collected at different locations and from sequential operational volume scans, can be displayed in a time-height format much like a traditional stationary CVP, with dark columns indicating data plotted in the vertical, and graduated rectangles indicating how these data are visually smoothed to create a cohesive image. The data themselves are not smoothed in time, and only done so for the sake of the image, in the same manner as QVPs.

Figure 2.7 shows a CVP moving in time, using data from the KVNX S-band WSR-88D operational radar located at Vance Air Force Base, OK, on May 20, 2011, during the MC3E field campaign. On this day, the University of North Dakota (UND) Cessna Citation II jet aircraft was flying within and on the periphery of the stratiform region of a large mesoscale convective system passing over central Oklahoma, and was within the requisite 110 km of the KVNX radar for the entire flight, from roughly 13-17 UTC. The CVP is centered on the location of the aircraft at the recorded start time of the lowest elevation scan in each volume scan, with the black line on all subpanels denoting the aircraft altitude at that time. Having the CVP move in such

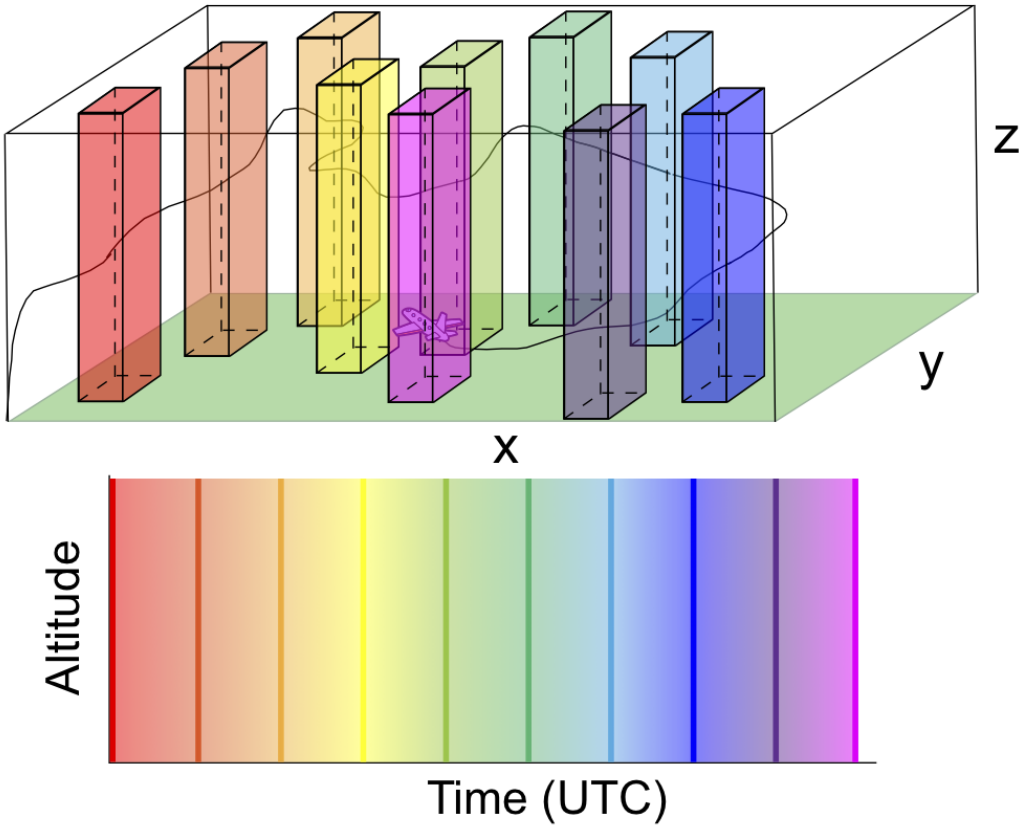

Figure 2.6: A conceptual model of how a moving CVP is created following the flight path of an aircraft. The upper panel shows how data are sourced from different regions for each sequential volume scan, and the lower panel shows how the data are then plotted in a time-by-height format.

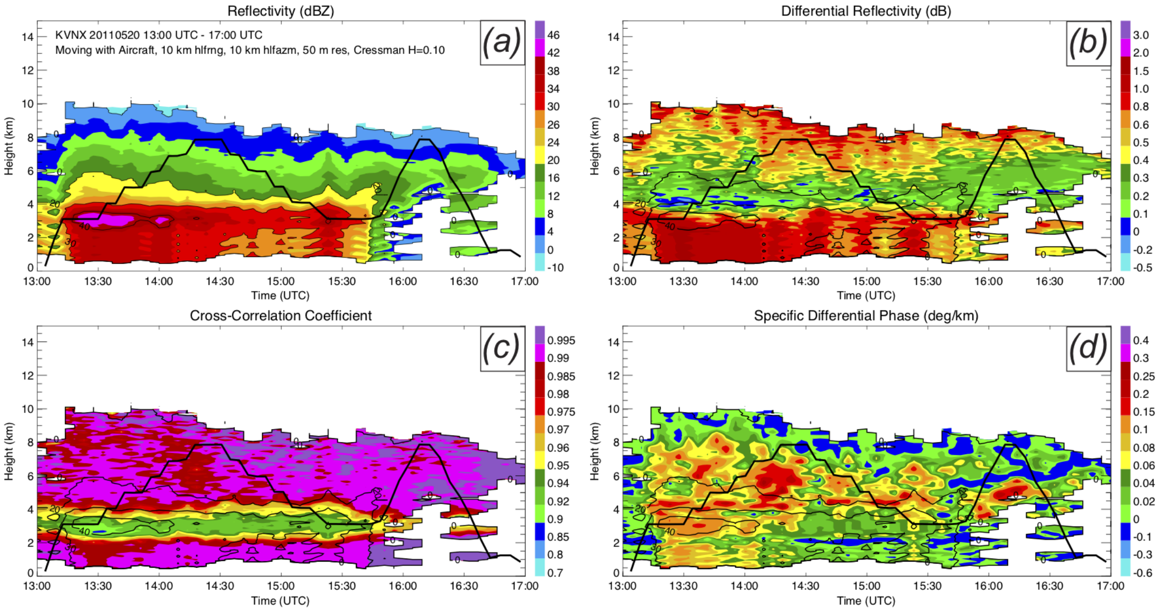

Figure 2.7: Moving CVP using data from the KVNX radar on May 20, 2011 from 13-17 UTC. The CVP sector moved with the location of the research aircraft flying during the MC3E campaign. Panels show (a) Z, (b) Z_{DR}, (c) ρ_{hv}, and (d) K_{DP}. The black line overlaid on each panel represents the altitude of the aircraft with time. Vertical data spacing in the CVP is 50 m, and the sector size is 20 km in range and 20° in azimuth.

a manner results in vertical columns of data that are representative of the region in which the aircraft is flying.

Chapter 3

Methodology

Data from multiple field campaigns and a number of different intensive operation periods (IOPs) are used in this study. The main focus will be on the May 20, 2011 MCS during the MC3E campaign, with additional analyses of the April 27, 2011 MCS during MC3E and July 6 and 9, 2015 MCSs during PECAN. Short descriptions of these cases and the data collected during each are offered in sections 3.1 and 3.2, respectively. More extensive detail about the individual campaigns and their observing platforms beyond what is relevant for this study is available in Jensen et al. (2016) for MC3E and Geerts et al. (2017) for PECAN. Section 3.3 expands on the aircraft and radar data collocation technique introduced in section 2.3, and section 3.4 details a newly developed ice microphysical retrieval technique to be used in this study.

3.1 Case Overviews

The MC3E campaign focused on obtaining measurements of convective clouds to improve scientific understanding of convective processes, and utilize this knowledge to improve their representation in models. The campaign was based out of the DOE ARM Southern Great Plains (SGP) Central Facility (CF) (`www.arm.gov/sites.sgp`) in north-central Oklahoma, “where an extensive array of both airborne and ground-based instrumentation was deployed” (Jensen et al., 2016, see their Fig. 1). Operational weather radar data were collected by the KVNX radar during the entire campaign. Because of the fixed location of ground instrumentation, IOPs were tethered in geographic location to northern OK.

On April 27, 2011, while the southeastern United States was dealing with the first of three deadly rounds of tornadoes, north central OK experienced persistent stratiform precipiation from approximately 7-13 UTC. This stratiform rain appeared to be the remnants of a small convective line that attempted to organize on the OK panhandle late on April 26, 2011. This convection quickly fell apart, but its associated shallow stratiform precipitation grew in spatial scale and persisted throughout most of April 27th, passing right over the MC3E observing domain.

The MCS sampled during the May 20, 2011 MC3E mission resulted in a robust dataset of ground, aircraft, and radar measurements. This was a particularly successful case during the MC3E campaign, such that the data collected have been examined in a number of different capacities within multiple publications (e.g., Van Lier-Walqui et al., 2016; Fridlind et al., 2017; Marinescu et al., 2017). Discrete convective cells formed in far southwestern OK/the southeastern TX panhandle around 4 UTC and quickly grew upscale into a convective line by 7 UTC. The line developed a robust stratiform region by 10 UTC as it approached central OK, and the leading line and trailing stratiform persisted in intensity as the system traversed the state in a mainly east-west fashion, decaying into disorganized convection embedded in stratiform on and after 20 UTC over northern AK/southern MO. The archetypal structure of the MCS on that day, the persistance of its stratiform region, and its path directly over the MC3E observing domain made this a particularly attractive case to study.

The PECAN experiment utilized more mobile assets than did MC3E. A core domain for IOPs was defined as an approximate 5 degree latitude by 6 degree longitude box over southern NE, KS, and northern OK; however, the actual domain over which IOPs were conducted stretched longitudinally from CO to IN, and latitudinally from north TX to ND (Geerts et al., 2017, see their Fig. 1b). This experiment was much more mobile in nature than MC3E because the ground instrumentation itself was mobile, and not tethered to a specific location such as the ARM SGP CF in

MC3E. Operational weather radar data were sourced from a number of different radars nationwide for this campaign.

On July 6, 2015, just after 0 UTC, an MCS began to develop in southern SD. Around 4 UTC, that convection started to merge with convection to its northeast and southwest, with stratiform precipitation developing by 5 UTC behind the convective line. Robust stratiform precipitation persisted as the convection began to decay, with stratiform precipitation passing over the Grand Forks, SD (KFSD) WSR-88D radar from approximately 5-9 UTC. The system progressed off to the ENE and began to dissipate after this time.

At the other end of the PECAN domain, on July 9, 2015, an MCS was sampled in the northern TX panhandle. Convection initiated in the far NW panhandle around 0 UTC, propagating to the SSE. Stratiform that was more parallel in nature (e.g., Parker and Johnson, 2000) formed around 3 UTC, transitioning to trailing stratiform around 5 UTC and passing over the Amarillo, TX (KAMA) WSR-88D radar. The MCS persisted to the SSE, decaying by about 14 UTC in the SE TX panhandle.

3.2 Aircraft In Situ Data

3.2.1 In Situ Probes

During MC3E, the University of North Dakota (UND) Cessna Citation II aircraft housed all of the in situ microphysical instrumentation. The goal was to sample ice-phase hydrometeors, such that flights focused on the region between the ML and cloud top. The two probes of particular interest to this study are the 2D cloud imaging probe (2D-C) and the high-volume precipitation spectrometer, version 3 (HVPS-3, hereafter just HVPS). The 2D-C measured cloud and precipitation particle number distribution functions, nominally measuring particles from 0.03 to 1.0 mm, whereas the HVPS measured precipitation particle number distribution functions, nominally measuring particles from 0.15 to 19.2 mm. On April 27, the aircraft flew a step down pattern into a single spiral up and down pattern, whereas on May 20, the aircraft flew both a step up and step down pattern into a single spiral up and down pattern. Although two probes sampling cloud particle distributions, the 2D-C and Cloud Imaging Probe (CIP), were installed on the aircraft, the 2D-C data are used because that probe had modified tips designed to reduce shattering, whereas the CIP did not. For probes without anti-shattering tips, after a crystal bounces off the tip or inlet, the shattered fragments may travel into the sample area and cause multiple artificial counts of small ice (Korolev et al., 2013). Although the data processing technique used for the in situ data herein has routines to eliminate shattered artifacts (see section 3.2.2), for this reason, the 2D-C data are used to derive cloud particle size distributions for MC3E.

During PECAN, the NOAA P-3 aircraft housed all of the in situ microphysical instrumentation, concentrating on the study of MCS dynamics and microphysics. For the cases analyzed herein, flights mainly focused on passes through the ML, with the P-3 flying a combination of straight legs and spiral ascents and descents in the trailing stratiform region. The two probes of particular interest to this study are the CIP and Precipitation Imaging Probe (PIP). The CIP measured primarily cloud particle spectra, measuring particles from 0.125 to 1.6 mm, whereas the PIP measured precipitation particle spectra, measuring particles from 0.6 to 6.4 mm. The P-3 performed a number of spirals during both IOPs, 4 in total on July 6 and 8 on July 9.

During PECAN, the PIP malfunctioned fairly regularly, leading to a dataset that is not of consistently good quality. For that reason, for analyses of in situ microphysical data herein, the focus will be on the 2D-C and HVPS probes in MC3E, and the CIP in PECAN.

3.2.2 Data Processing and Bulk Properties

The data used in this study were processed using the University of Illinois/Oklahoma Optical Array Probe (OAP) Processing Software (UIOOPS; McFarquhar et al., 2018). UIOOPS is a collection of 22 total codes that are used to process data and compute particle size distributions (PSDs) from optical array probe data. The code outputs information on the morphology of individual particles and PSDs, as well as estimates of bulk extinction, mass weighted terminal velocity, and ice water content. A general overview of the processing technique is provided here; a wealth of information beyond what is reproduced here is available in McFarquhar et al. (2018). There are three steps that the software follows to generate PSDs from raw 2D optical array probe data: processing OAP raw data, generating shape parameters for each particle, and determining size distributions.

First, OAP raw data are processed. The first file produced in this step contains raw image data of every frame recorded by the probe, and timing information about the frame (from the year down to the millisecond of data collection). After the particle images and timing information are output, a netCDF file is generated containing several descriptors (e.g. timing information, morphological description) of each particle. In generating this netCDF file, the software also accepts or rejects particles based on a series of criteria designed to remove spurious stuck bits, splash artifacts, blank records, and streaker particles (but not shattered artifacts).

In the second step, shape parameters for each particle are generated. These include parameters such as the particle's projected area (A_p), the length of the particle in the directions perpendicular and parallel to the photodiode array (L and W, respectively), and several calculations of D_{max}, or the particle's maximum dimension. These parameters can be used to eliminate shattered artifacts. If $L/W > 5$ (or 6, if the particle touches the edge of the photodiode array), the particle is rejected, to remove streakers and stuck bits with large aspect ratios. Additionally, a particle is identified as out of focus if it is a spherical hollow particle, and particle size for those such particles is adjusted using a correction factor according to Korolev (2007).

Third, the particle shape parameters are used to determine the size distributions. To check for streakers and stuck bits, the area ratio is defined as

$$A_r = \frac{A_p}{(\pi/4)D_{max}^2} \tag{3.1}$$

If $A_r < 0.2$, then the particle is removed. Additionally, the interarrival time, or time difference between two successive particles passing through the probe's sample volume (e.g., Korolev and Field, 2015), is used to eliminate shattered artifacts. Because shattered particles are closely spaced, their interarrival time is typically much less than that for naturally occurring particles. Therefore, when an interarrival time is less than a given threshold (determined using one of multiple methods), the particle and the preceding particle are removed. For PECAN, that threshold was determined on a spiral-by-spiral basis, with an average value of $3.5 * 10^{-5}$ across all spirals during the project, and average values of $2.07 * 10^{-5}$ and $5.09 * 10^{-5}$ for July 6 and 9, 2015, respectively (Stechman, 2018). For MC3E, the data suggested that few shattered artifacts were sampled by either the 2D-C or HVPS probes, and therefore no shattering removal algorithm was used for either probe (Wu and McFarquhar, 2016).

After these final tests to remove artifacts are performed, size distributions and bulk parameters can be calculated. The number of accepted particles in a size bin j for each 1 s time interval is determined and represented as $N_{acc}(j)$. Noting that D_j is the midpoint of D in bin j with width ΔD_j, the 1 s number distribution function $N(D_j)$ can be calculated, where

$$N(D_j) = \frac{N_{acc}(j)}{(SA)(TAS)(1 - t_d)} \tag{3.2}$$

where SA is the probe sample area, TAS is the true air speed, and t_d is the deadtime of the probe in the 1 s time period. The size distribution is then sorted into bins according to A_r and D_{max}, and is represented as $N(D_j, A_{r_k})$, where j represents the jth size bin with midpoint D_j and k represents the kth A_r bin with area ratio midpoint A_{r_k}. This can be determined by replacing $N_{acc}(j)$ in eqn. 3.2 with $N_{acc}(j,k)$, to sort particles by both size and area ratio.

To calculate IWC, two methods are used in the software. The first uses mass-dimensional relationships, and was not used in this study. The second uses the cross sectional mass-area relation of Baker and Lawson (2006), where

$$IWC = \sum_j \sum_k a \left(\frac{\pi}{4} D_j^2 A_{r_k} \right)^{1.218} N\left(D_j, A_{r_k}\right) \Delta D_j \tag{3.3}$$

where $a = 0.115\ mg * mm^{-2.436}$. After determining the PSDs for each second, the median mass dimension, D_{mm}, is also calculated and is the primary measurement of particle dimension used in most microphysical studies. It is defined as the diameter for which half of the mass is given by particles with maximum dimensions smaller than D_{mm}, and half of the mass is given by particles larger than D_{mm} (McFarquhar and Heymsfield, 1998).

3.2.3 Particle Imagery

During the May 20, 2011 MC3E flight, the aircraft flew one spiral through the entire depth of the DGL. This spiral provided an opportunity to examine particle shapes and habits, and the relative concentrations of particles with these varying shapes and habits, in this region in detail. As mentioned in Griffin et al. (2018), an anticorrelation of Z_{DR} and K_{DP} signatures was often seen within the DGL in winter storms. They postulated that this anticorrelation was related to the presence of dendrites, and the relative concentrations of dendrites and isometric ice. Examination of particle images from both the 2D-C and HVPS probes captured as the aircraft flew the downward leg of its spiral through the DGL will give further information about the relative concentration of dendrites and isometric ice in the DGL of MCSs, and about the microphysical causes for any polarimetric signatures that are or are not observed during the time of the spiral.

3.3 Collocation of CVP and Aircraft Data

Employing the moving CVP technique allows for polarimetric radar data to be collocated to in situ aircraft data in time, range from the radar, and azimuth; however, the four-dimensionality of radar data means that these data still need to be collocated to the aircraft location in the vertical. This presents a challenge, as the aircraft is often moving vertically as the radar is performing the volume scan, and the exact time the data in each vertical column of the CVP were collected cannot be definitively stated, due to the nature of the vertical smoothing of data at each vertical level. To deal with these challenges, we employ a collocation technique between the polarimetric radar data and aircraft in situ data that includes a time-offset component for the CVP data. The technique is as follows. For every full volume scan of data (and therefore every column in the CVP), the start times of that volume scan and of the following volume scan are recorded. Then, the data in the CVP column associated with the current volume scan are assigned times that are linearly offset between the start times of the current and next volume scans, with time increasing with increasing altitude in the CVP column. In other words, data collected higher in the vertical are assumed to have been collected later in time, with the time of data collection increasing linearly with height in the CVP column, from the start time of the current volume scan to just before the start time of the next volume scan.

After assigning approximate times of data collection for every data point in the CVP, we assume that the data at that specific altitude are actually representative of the region between that altitude and the altitude above (e.g., for a 50 m resolution CVP, the data at 5.50 km in the CVP datafile are assumed to be representative of the region from 5.50 to 5.55 km). This is done since the aircraft will rarely, if ever, be located at the exact altitude CVP data are assigned at that exact time, and is a reasonable assumption again due to the nature of the vertical smoothing inherent to CVPs. For every region of CVP data in the vertical, the altitude of the aircraft

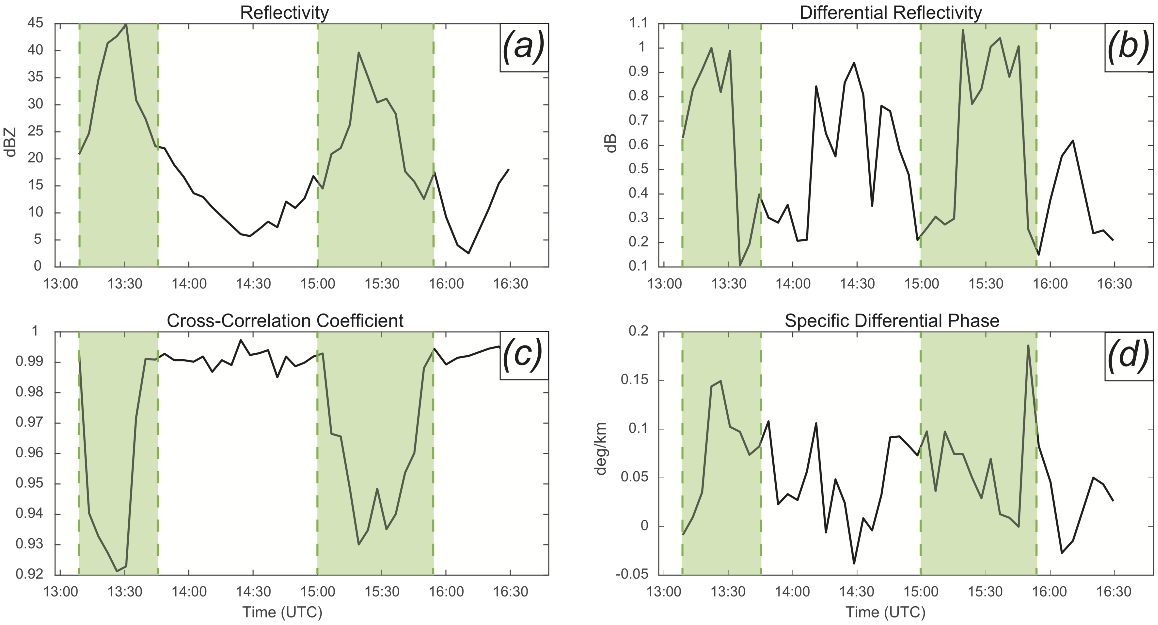

Figure 3.1: Time series plots of (a) Z, (b) Z_{DR}, (c) ρ_{hv}, and (d) K_{DP} collocated to the aircraft location as it flew through the MCS represented in the CVP in Fig. 2.7. Green shaded regions represent times where the aircraft flew within or below the ML.

is found at the region's estimated collection time. If the aircraft was within the given CVP data region in the vertical at the region's estimated collection time, the CVP and aircraft in situ data are extracted and saved as collocated data for future analyses. Data extraction is then suppressed for the next ten seconds, to prevent data extraction from two nearly identical locations in the CVP and locations of the aircraft. In analyses herein, we use CVPs with 50 m data spacing in the vertical. Fig. 3.1 shows a time series plot of polarimetric radar data extracted from the flight path shown on the CVP in Fig. 2.7, with green shaded regions representing times where the aircraft flew within or below the ML. Looking qualitatively at Figs. 2.7 and 3.1, both figures in conjunction clearly show that the values extracted from along the flight path match up quite well to the values where the aircraft was flying in the images, corroborating the effectiveness of this technique.

3.4 Ice Microphysical Retrieval Technique

3.4.1 Development of Technique

As previously mentioned, polarimetric radar data provide a wealth of information that can be used to improve existing ice microphysical retrieval algorithms and develop even more sophisticated ones. The ice microphysical retrievals used in this study were developed by Ryzhkov et al. (2018), and use Z_{DP}, Z, Z_{dr}, K_{DP}, and radar wavelength λ to estimate IWC, N_t, and mean volume diameter (D_m). D_m differs from D_{mm} in that D_m is the ratio of the fourth and third moments of the size distribution (Zhang, 2017), whereas D_{mm} is the "dimension for which half of the mass is given by particles with maximum dimensions smaller than [D_{mm}]" (McFarquhar and Heymsfield, 1998). Knowing that Z_{DP} can be calculated from Z and Z_{DR}, and that Z_{dr} is Z_{DR} in linear scale, this algorithm truly uses three radar variables (Z, Z_{DR}, and K_{DP}) to estimate three microphysical variables. A short overview of the development of the retrievals is provided herein. The majority of the text is sourced from Ryzhkov et al. (2018), with more detail available therein. A typo in eqn. 18 in Ryzhkov et al. (2018), herein eqn. 3.11, has been identified and rectified (Alexander Ryzhkov, personal communication).

Ryzhkov et al. (2018) start the development of their retrieval techniques by explaining that multipliers in IWC(Z) power-law relations are almost entirely dependent on the product αD_m^2, where α is related to the density of snow (ρ_s) such that

$$\rho_s \approx \alpha D^{-1} \tag{3.4}$$

and α is proportional to the degree of riming. They further showed that an analytical expression for IWC in terms of Z can be obtained following derivations of Hogan et al. (2006) and Bukovcic et al. (2018):

$$IWC = 3.09 * 10^{-3} \left(\frac{Z}{\alpha D_m^2} \right) \tag{3.5}$$

Therefore, the first step in determining IWC is calculating D_m. To do so, they use K_{DP} measurements, based on the fundamental fact that Z is proportional to the 4th moment of the snow size distribution and K_{DP} is proportional to the 1st moment (given that snow density is inversely proportional to the diameter of the snow particle). The ratio of Z to K_{DP} is therefore approximately proportional to D_m^3.

The advantage of using the ratio of Z and K_{DP} to estimate D_m is that it has low sensitivity to size distribution variability, changes in snow density, and degree of riming (due to the mutual proportionality of Z and K_{DP} to α). However, such an estimator does not account for the diversity of ice particle shapes and orientations, both of which strongly affect K_{DP}. This makes the estimator most appropriate for irregular or aggregated snow, which are mostly isotropic and have little aspect ratio variability. Therefore, this works well for regions near the ML, where aggregates typically dominate sampling volumes, but poorly for ice regions aloft such as the DGL, where highly anisotropic particles are most prevalent. Since the primary region of interest for this study is high up in ice clouds, modifications to such an approach must be made.

It is therefore imperative to develop a D_m estimator that is immune to variations in particle shape and orientation. As mentioned in section 1.2, Ryzhkov et al. (1998) developed a retrieval technique for IWC that depended on Z_{DP} and K_{DP}, whose ratio is robust with respect to the variability of particle aspect ratio and orientation due to how similarly particle aspect ratio and orientation affect the values of both. So, a similar approach can be used here to estimate D_m. It can be shown that Z_{DP} is roughly proportional to the 3rd moment of the snow size distribution (Ryzhkov et al., 2018), such that the ratio of Z_{DP} and K_{DP} is expected to be linearly dependent on D_m^2. Following this reasoning, the variable η is defined as:

$$\eta = \left(\frac{Z_{DP}}{K_{DP}\lambda} \right)^{\frac{1}{2}} \tag{3.6}$$

where Z_{DP} is in linear scale and λ is radar wavelength in mm.

Ryzhkov et al. (2018) simulated the value of η and D_m for 12 snow habits, including irregular/aggregated snow with aspect ratio of 0.6, and 11 types of pristine ice crystals as in Matrosov et al. (1996). All particles are modeled as oblate or prolate spheroids, with aspect ratios dependent on particle size, approximated by the power-law relation

$$h = cL^d \tag{3.7}$$

for all 12 snow habits, where L is the larger and h is the smaller dimension of a crystal, both expressed in mm. Table 3.1 offers more detail on the 11 snow habits besides irregular/aggregates, and shows values of c and d for each. Using the results of these simulations, they developed an equation for D_m dependent on η, such that:

$$D_m = -0.1 + 2.0\eta \tag{3.8}$$

This equation approximates the average dependence of D_m on η for all 12 snow habits.

	Crystal Habit	c	d
1)	Dendrites	0.038	0.377
2)	Solid Thick Plates	0.230	0.778
3)	Hexagonal Plates	0.047	0.474
4)	Solid Columns ($\frac{L}{h} < 2$)	0.637	0.958
5)	Solid Columns ($\frac{L}{h} > 2$)	0.308	0.927
6)	Hollow Columns ($\frac{L}{h} < 2$)	0.541	0.892
7)	Hollow Columns ($\frac{L}{h} > 2$)	0.309	0.930
8)	Long Solid Columns	0.128	0.437
9)	Solid Bullets ($L < 0.3$ mm)	0.250	0.786
10)	Hollow Bullets ($L > 0.3$ mm)	0.185	0.532
11)	Elementary Needles	0.073	0.611

Table 3.1: Parameters c and d in Eqn. 3.6 for different types of crystals (as in Matrosov et al., 1996).

They next show that IWC can be determined from the combination of Z and D_m, using γ, where:

$$\gamma = \alpha D_m^2 \tag{3.9}$$

It can be shown that γ is highly correlated with η^2:

$$\gamma \approx 0.78\eta^2 = 0.78\left(\frac{Z_{DP}}{K_{DP}\lambda}\right) \tag{3.10}$$

From Eqns. 3.5 and 3.10, an equation for IWC can be derived:

$$IWC \approx 4.0 * 10^{-3}\left(\frac{K_{DP}\lambda}{1 - Z_{dr}^{-1}}\right) \tag{3.11}$$

Total concentration of ice particles N_t can be estimated from the combination of Z and γ. Ryzhkov et al. (2018) show that $\log(N_t)$ can be estimated as such:

$$\log(N_t) = 0.1Z - 2\log(\gamma) - 1.33 \tag{3.12}$$

where Z is expressed in dBZ and N_t in L^{-1} to facilitate comparison to aircraft observations of N_t, which are typically expressed in L^{-1}.

Before calculating these microphysical quantities, data are thresholded such that retrievals are only performed for points where $Z > 0.1$ dB, $Z_{DR} > 0.1$ dB, and $K_{DP} \geq 0.01$ deg/km. For clarity, Table 3.2 lists the 3 equations that will be used in ice microphysical retrievals herein.

Variable	Equation	Equation Number
D_m	$D_m = -0.1 + 2.0\eta$	3.8
IWC	$IWC \approx 4.0 * 10^{-3}\left(\frac{K_{DP}\lambda}{1-Z_{dr}^{-1}}\right)$	3.11
N_t	$\log(N_t) = 0.1Z - 2\log(\gamma) - 1.33$	3.12

Table 3.2: Summary of ice microphysical retrieval equations and their equation numbers used in this study.

3.4.2 Application to Moving CVPs

After a moving CVP is created for a particular flight and interval of time, the data at each vertical level can be ingested into the aforementioned ice microphysical retrieval algorithms. Only data above the ML, subjectively determined by examining moving CVP images, are ingested into the algorithms, producing estimates of D_m, N_t, and IWC at all altitudes above the ML on the moving CVP. Microphysical retrieval data are then collocated to aircraft in situ data in the same manner in which CVP and aircraft in situ data are collocated, explained in section 3.3. More detail and examples of this technique are available in section 4.5.

Chapter 4

Results

4.1 Moving CVPs

The first case of interest to this study is May 20, 2011, where the aircraft flew through a robust region of stratiform cloud for approximately 4 hours. Shown in Fig. 2.7, the aircraft remains within stratiform precipitation resolvable by the radar until the very end of the flight. A robust ML from 3-4 km is visible in both Z and ρ_{hv}, and hinted at via an enhancement of Z_{DR} below 4 km, indicative of oblate raindrops. Of note is that there is very little enhancement in the DGL of Z_{DR}, and slight enhancement of K_{DP}, where the DGL is between approximately 6-7.5 km (estimated from coincident aircraft altitude and air temperature measurements). A lack of Z_{DR} signature and presence of K_{DP} signature is also seen in the QVP from this day constructed using data before and just after the aircraft took off (Fig. 1.4). This absence of a strong Z_{DR} signature in the DGL could mean that it is dominated by isometric ice, with little to no dendrites (Griffin et al., 2018).

There are a number of degrees of freedom when creating a CVP. One of the many adjustable specifications is the vertical data spacing. In this study, a 50 m vertical data spacing is employed, but the CVP algorithm can be tuned to create CVPs of any vertical data spacing. Fig. 4.1 is analogous to Fig. 2.7, but with a vertical data spacing of 10 m instead of the typical 50 m. Comparing the two CVPs, qualitatively, it is extremely difficult to find any differences between the two. Just how fine the vertical data spacing should be in a CVP to adequately resolve polarimetric signatures is a topic of continuing work, and is also a highly subjective question, depending on the goals of the project and type of precipitation. The remainder of the work shown herein will use exclusively 50 m moving CVPs.

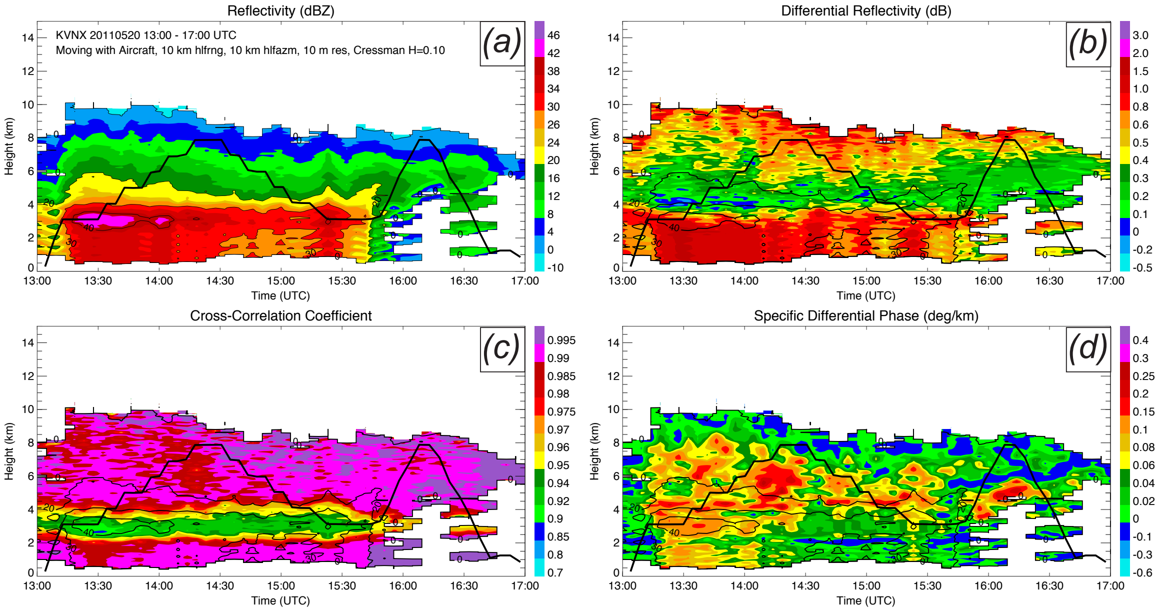

Figure 4.1: As in Fig. 2.7, but with vertical data spacing of 10 m.

On April 27, 2011, the precipitation was much more shallow, with a freezing level at only 2 km. Figure 4.2 shows a moving CVP for that case, with shallow precipitation that extends only to a height of 5-6 km. Most notable about this case is the prolific number of gaps in the CVP. Some of the small gaps in Fig. 4.2 could potentially be smoothed by increasing the Cressman radius of influence, another degree of freedom when creating a CVP. The Cressman radius of influence is how far away in the vertical from each vertical level the algorithm will search for data to interpolate to that location, using a weighted averaging technique. In this study, a Cressman radius of influence of 100 m is used. As mentioned previously, this use of a Cressman averaging technique often fills in data gaps due to its averaging in the vertical, but can still allow for gaps in data if, for a given vertical location, there are no radar data within the vertical distance of the Cresman radius of influence above or below that location. Figure 4.3 shows a moving CVP analogous to Fig. 4.2, but with a 250 m Cressman radius of influence. The gaps in the vertical are markedly reduced, due to the larger window in the vertical from which data are being sourced

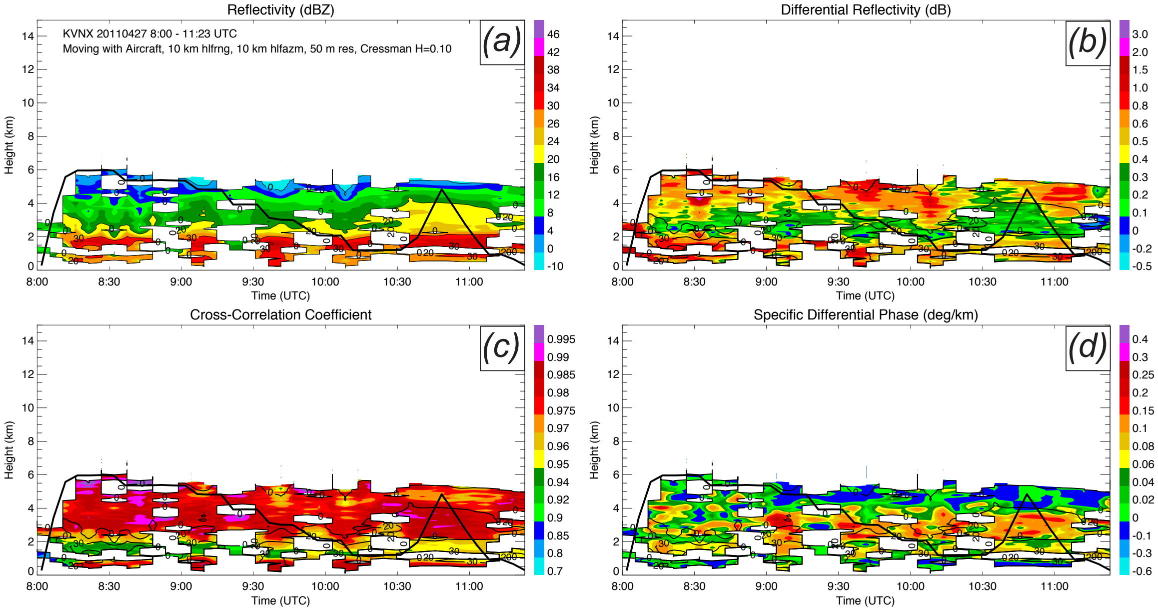

Figure 4.2: Moving CVP using data from the KVNX radar on April 27, 2011 from 8-11:23 UTC. The CVP sector moved with the location of the research aircraft flying during the MC3E campaign. Panels show (a) Z, (b) Z_{DR}, (c) ρ_{hv}, and (d) K_{DP}. The black line overlaid on each panel represents the altitude of the aircraft with time. Vertical data spacing in the CVP is 50 m, and the sector size is 20 km in range and 20° in azimuth.

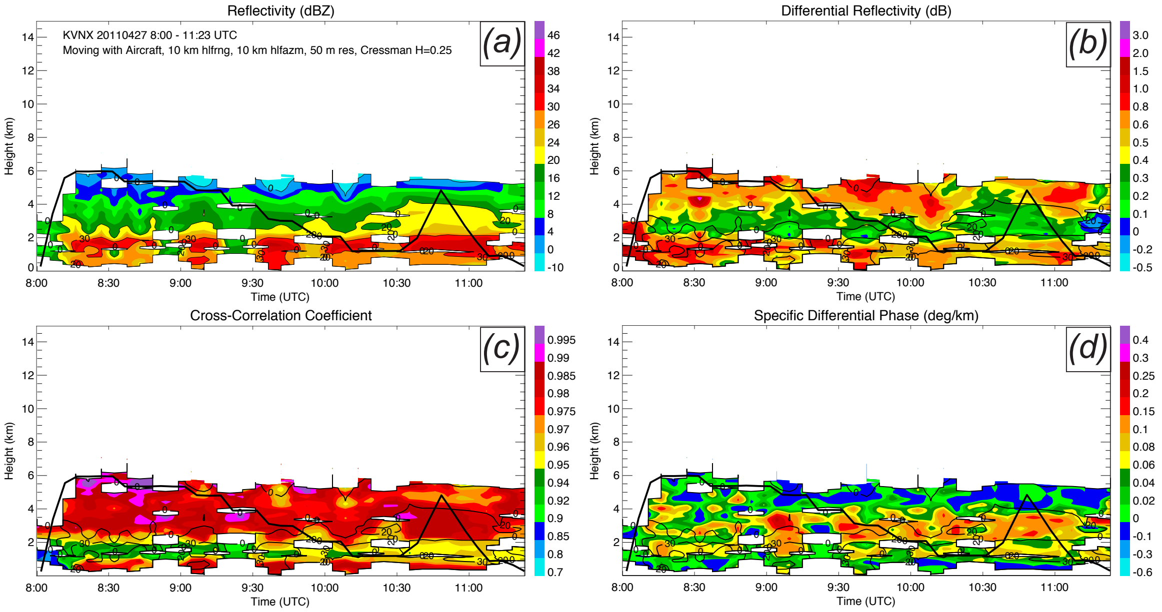
Reflectivity (dBZ)

Differential Reflectivity (dB)

Cross-Correlation Coefficient

Specific Differential Phase (deg/km)

Figure 4.3: As in Fig. 4.2, but with a Cressman radius of influence of 250 m.

for each vertical level. However, with this reduction in gaps in the data comes with more smoothing in the vertical, potentially smoothing out fine scale polarimetric signatures as a result. In a case such as this where the number of gaps in the vertical severely impedes the ability to analyze the image, this additional smoothing via a larger Cressman radius of influence may be warranted. Although some smoothing of polarimetric signatures is visible between Figs. 4.2 and 4.3, upon close inspection, there appears to be qualitatively little loss of information in this case. As the CVP methodology is used more, the use of varying Cressman radii of influence and their effect on the ability to resolve fine scale polarimetric signatures must be explored.

The storm was considerably deeper on July 6, 2015, where the P-3 flew through MCS stratiform extending up to 14 km. In the moving CVP for this case (Figure 4.4), a ML is visible in Z and ρ_{hv}, with an increase in Z_{DR} clearly visible below it, as in Fig. 2.7. There are also strong signatures of K_{DP} within the DGL (from approximately 6-8 km, estimated from aircraft altitude and air temperature measurements at the bottom of the DGL and assuming a somewhat constant lapse rate). This region

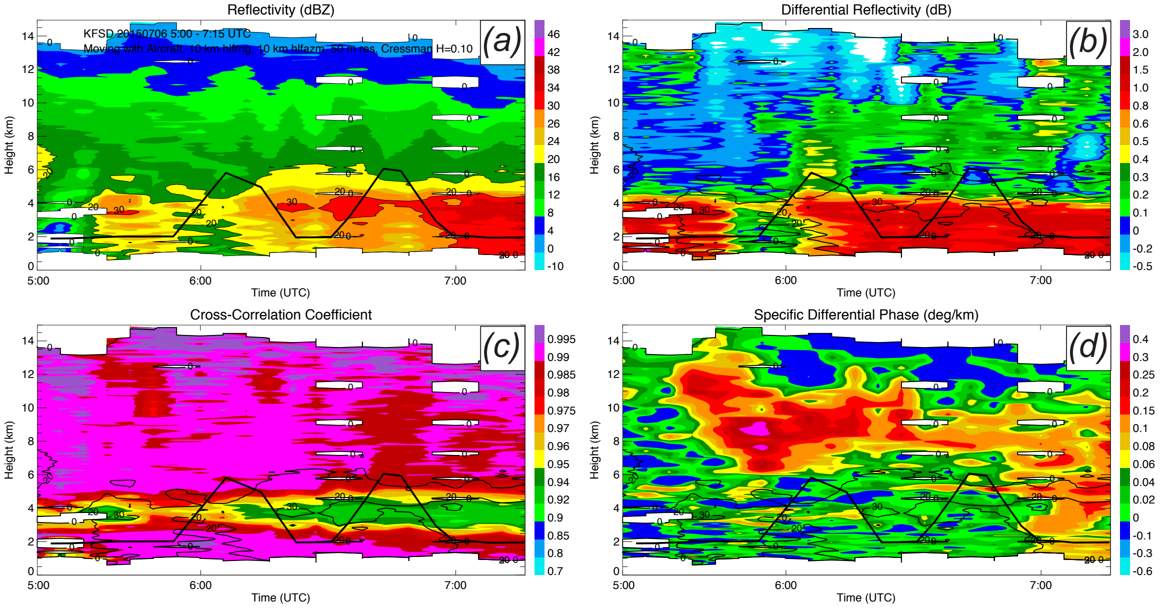

Figure 4.4: Moving CVP using data from the KFSD radar on July 6, 2015 from 5-7:15 UTC. The CVP sector moved with the location of the research aircraft flying during the PECAN campaign. Panels show (a) Z, (b) Z_{DR}, (c) ρ_{hv}, and (d) K_{DP}. The black line overlaid on each panel represents the altitude of the aircraft with time. Vertical data spacing in the CVP is 50 m, and the sector size is 20 km in range and 20° in azimuth.

of high K_{DP} is collocated with a region of low Z_{DR}, which could indicate a high concentration of predominantly isometric ice. Additionally, such strong signatures of K_{DP} are likely to result in more extreme ice microphysical retrieval estimates.

One peculiar quality about the July 6, 2015 moving CVP is its non-monotonic time scale. This is the result of the aircraft flying near the 110 km range limit, where at distances further, CVPs cannot be made. Out of 28 scans performed during the time where the aircraft flew on July 6, 2015, 22 scans were within the required 110 km. The other 6 scans where the aircraft was beyond 110 km occurred not all at once, but one to two at a time throughout the period for which the CVP was made. On plots of CVP data, when the sector's center is not close enough to the radar for a CVP to be created for that volume scan, the processing technique does not insert data to create a blank column. Rather, it simply skips that scan and moves on to the next, such that no matter the length of time the CVP center was too far from the radar to create a CVP, the data from the time immediately before and immediately after the sector moved too far away will be plotted right next to each other on the x-axis. This plotting technique suggests temporal continuity between those times before and after the CVP was centered beyond 110 km, when in reality tens of minutes or even hours could have passed between columns of CVP data. This is something that must be taken into consideration when examining moving CVPs herein, and also when examining microphysical retrievals performed on these CVPs in section 4.5. The fact that scans are intermittently skipped when creating the July 6, 2015 moving CVP has been taken into account when overlaying aircraft flight tracks.

The moving CVP for the July 9, 2015 PECAN case will not be analyzed herein, due to the large number of gaps on that CVP as a result of the proximity to which the aircraft flew to the edge of the stratiform region. However, bulk microphysical properties of this system will still be examined in section 4.4.

4.2 Comparison of CVP and GridRad Techniques

Another recently developed technique to examine radar data and vertical profiles of radar data at any location in the United States is the GridRad technique (Bowman and Homeyer, 2017). GridRad data are data sourced from 125 S-band NEXRAD National Weather Service (NWS) radars (Crum and Alberty, 1993), merged together to create a three-dimensional, high-resolution dataset of radar data covering most of the contiguous United States. In publically available GridRad data, NEXRAD Level II data from multiple radar sites are merged and gridded to a regular, high-resolution (0.02° x 0.02° x 1 km), longitude-latitude-altitude grid. The data for this particular study differ slightly in that the vertical resolution of the data is 500 m from 1-7 km, providing greater detail of radar characteristics of precipitation in lower levels. GridRad data shown herein include Z, Z_{DR}, ρ_{hv}, and K_{DP} at 1-minute temporal resolution. Due to how data from all WSR-88D radars are merged to create GridRad data, polarimetric radar data are only available for cases occuring after the completion of the entire WSR-88D network's upgrade to dual-polarization capabilities, which herein include only PECAN and not MC3E cases.

To create GridRad vertical profiles, first, the gridpoint closest to the aircraft's location at the beginning of each given minute is found. Then, data are smoothed over nine gridpoints latitudinally and nine gridpoints longitudinally (i.e., an 81-gridpoint region) surrounding and including the gridpoint closest to the aircraft location. This process is repeated at the beginning of each minute of the flight. Averaging the GridRad data in this sense mimics the azimuthal averaging of radar data performed during the creation of CVPs. The main differences between GridRad vertical profiles and CVPs following the aircraft are the enhanced horizontal resolution of GridRad data, contrasted with the enhanced vertical resolution of the CVP data. In smoothing the GridRad data over a nine-by-nine gridbox, some of this enhanced horizontal resolution is eliminated; however, this averaging is paramount to reducing statistical noise of polarimetric radar variables, therefore proving especially important for investigations of (polarimetric) PECAN vertical profiles. Qualitative agreement between the vertical profiles created using the GridRad and CVP techniques would instill confidence that the CVP technique is accurately resolving the vertical profiles of radar data at locations along the aircraft track, given that the GridRad technique has been peer reviewed and used in a number of studies (e.g., Homeyer, 2014; Homeyer and Kumjian, 2015; Solomon et al., 2016; Cooney et al., 2018).

For the MC3E campaign, although the KVNX radar was equipped with dual-polarization capabilities, the entire WSR-88D network was not, so GridRad data are limited to only Z. However, comparisons can still be made between CVPs and GridRad vertical profiles to determine the CVP technique's effectiveness in constructing representative vertical profiles of Z at the aircraft's location. Figure 4.5 shows vertical profiles of Z following the aircraft on May 20, 2011, using the CVP and GridRad techniques. At a first glance, these profiles look qualitatively quite similar, increasing confidence that the CVP methodology is accurately resolving the vertical profile of Z over the aircraft's location. Beyond just a cursory look at both plots, there are a number of differences between the two. The ML in the GridRad plot is lower in peak magnitude than in the CVP, by about 5 dBZ. This is likely attributable to the vertical resolution of the GridRad data, which is 500 m at the height of the ML. Additionally, the CVP shows a cloud top height extending to near 10 km at the beginning of the period, with a minimum in cloud top height of approximately 8 km during the period. The GridRad technique shows a maximum in cloud top height of only approximately 9 km, except for some spurious peaks to 10 km through the period. The higher cloud top heights on the CVP are likely due to the finer vertical data spacing when compared to GridRad (50 m vs. 1 km at that altitude). In the GridRad profile, if the cloud top exists within a 1 km interval above 7 km, the data from below and above cloud top are smoothed together, and cloud top can appear

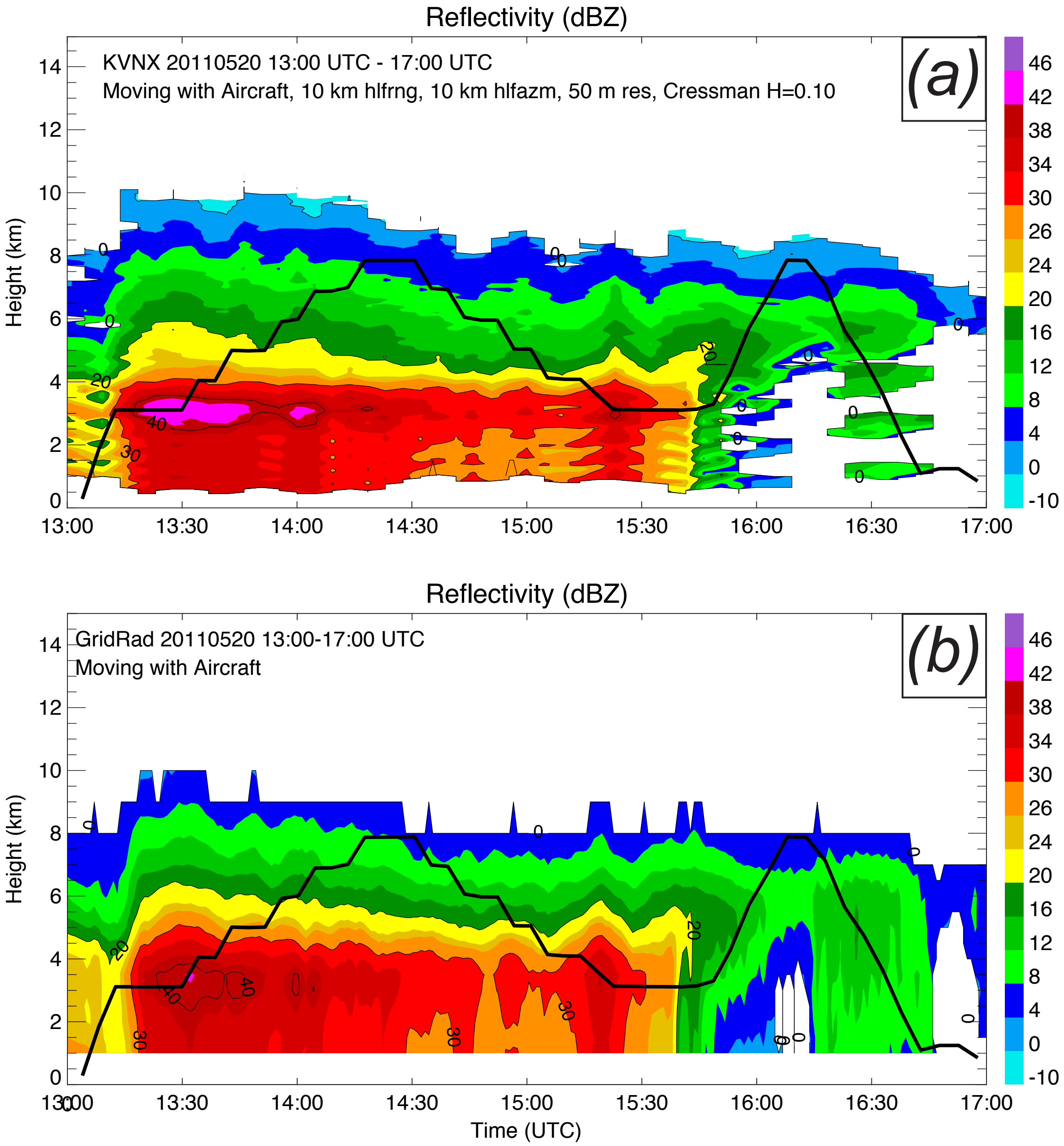

Figure 4.5: Vertical profiles of Z along the flight track during the May 20, 2011 MC3E flight, creating using the (a) CVP and (b) GridRad techniques. The black line overlaid on each panel represents the altitude of the aircraft with time. Vertical data spacing in the CVP is 50 m, and the sector size is 20 km in range and 20° in azimuth. Vertical profiles of GridRad data are created using data averaged over a nine-by-nine gridbox surrounding the closest longitude-latitude point to the aircraft location at the beginning of each minute.

lower on the GridRad profile than it actually is. In addition, the GridRad profile does have a finer temporal resolution, which is evident in regions of additional detail along the x-axis of Fig. 4.5b.

A similar analysis of CVP vs. GridRad vertical profile can be done for the April 27, 2011 MC3E case. Figure 4.6 shows vertical profiles of Z following the aircraft on April 27, 2011, using the CVP and GridRad techniques. Again, qualitative similarities between the profiles increase confidence that the CVP technique is accurately resolving the vertical profiles of Z over the aircraft's location. Although the CVP in Fig. 4.6a is riddled with gaps, close inspection reveals a temporal collocation of enhanced reflectively regions, similar vertical extents of various values of Z (i.e., similar vertical extents of each color plotted), and a similar cloud top height. While qualitative comparison is more difficult due to the number of gaps in Fig. 4.6a, one interesting difference between the two profiles is that the GridRad profile has a higher cloud top height after 9 UTC than the CVP. Whereas the CVP cloud top height hovers around 5 km, occasionally reaching 5.5 km, the GridRad cloud top height is fairly steady at 6 km. This difference likely suggests the opposite of what was occuring in Fig. 4.5–that the finer vertical data spacing in the CVP is resolving a cloud top height lower than the GridRad profile is. Additionally, gaps in the vertical may be artificially decreasing CVP cloud top height. The GridRad cloud top height is, at times, approximately 1 km greater than the CVP cloud top height, and the effects of a more coarse vertical data spacing in the GridRad data should only result in a cloud top height difference of less than 500 m at that altitude.

With the WSR-88D network upgrade to dual-polarization completed in 2013, GridRad data after that time include the full suite of polarimetric variables used to make CVPs. Therefore, comparisons of the techniques can go beyond just profiles of Z, and include profiles of Z_{DR}, ρ_{hv}, and K_{DP} as well. Figure 4.7 shows CVPs and GridRad vertical profiles of all four variables. Note that GridRad data have been

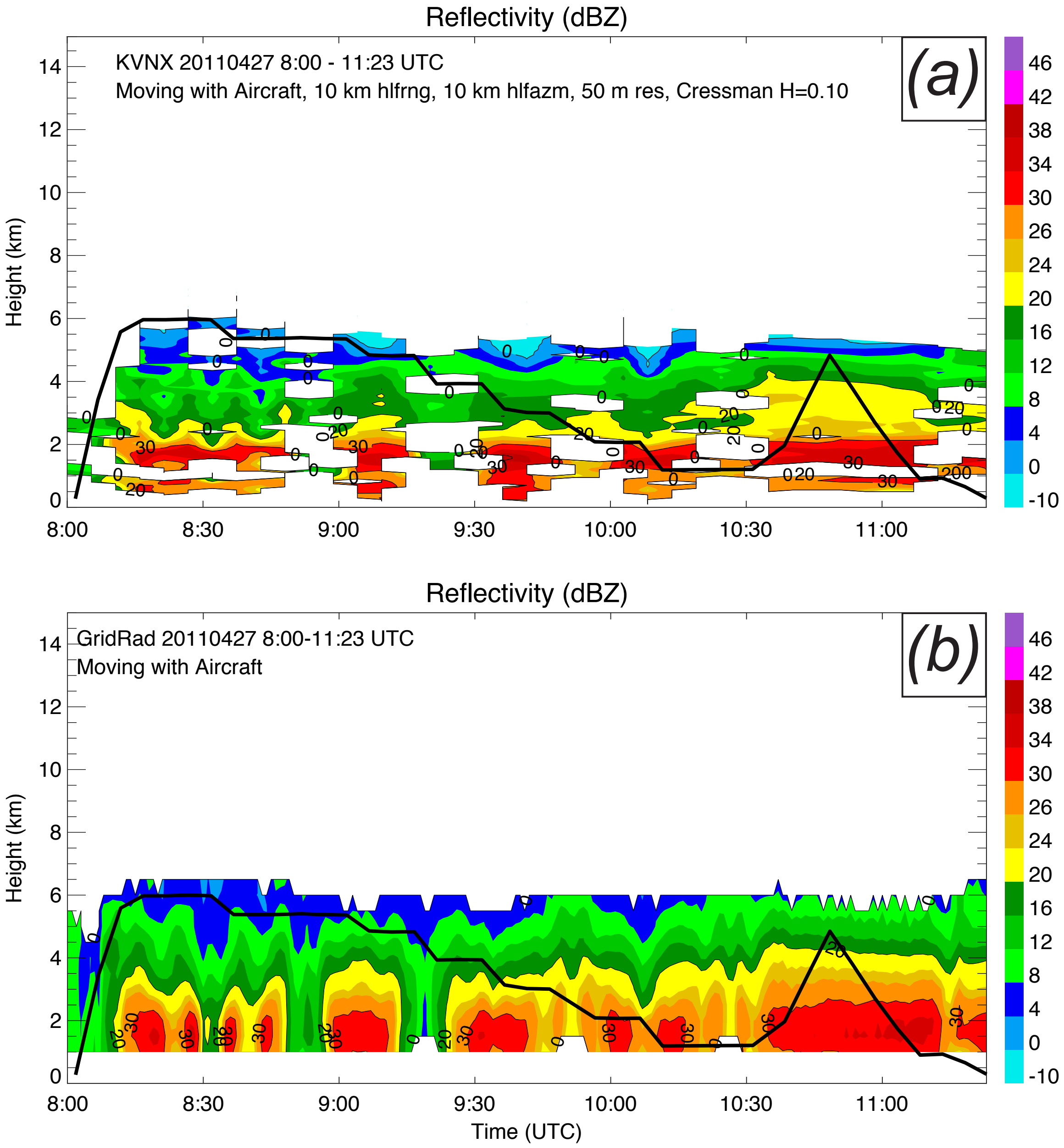

Figure 4.6: Vertical profiles of Z along the flight track during the April 27, 2011 MC3E flight, creating using the (a) CVP and (b) GridRad techniques. The black line overlaid on each panel represents the altitude of the aircraft with time. Vertical data spacing in the CVP is 50 m, and the sector size is 20 km in range and 20° in azimuth. Vertical profiles of GridRad data are created using data averaged over a nine-by-nine gridbox surrounding the closest longitude-latitude point to the aircraft location at the beginning of each minute.

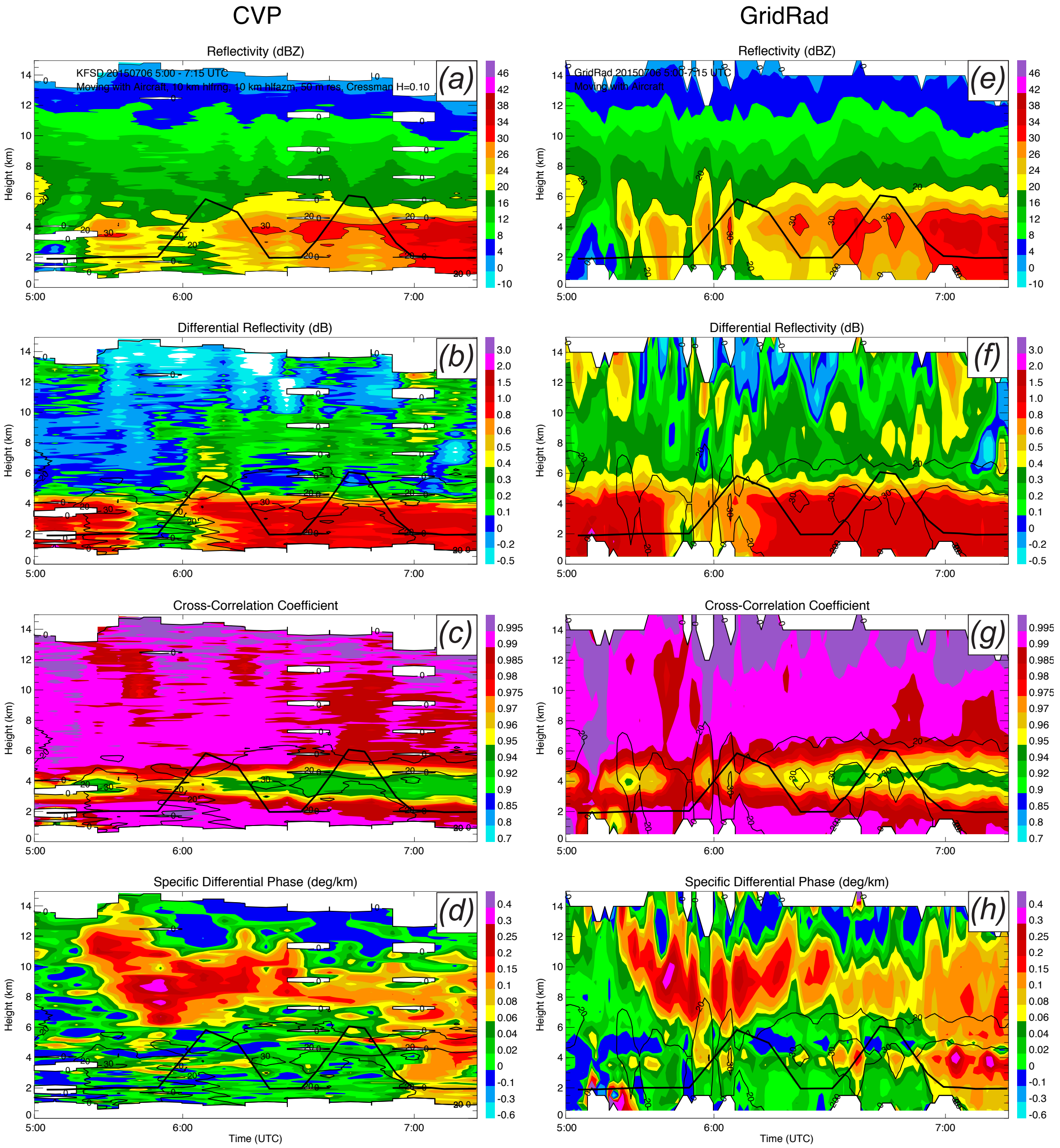

Figure 4.7: Vertical profiles of Z (a,e), Z_{DR} (b,f), ρ_{hv} (c,g), and K_{DP} (d,h) along the flight track during the July 6, 2015 PECAN flight, creating using the (a-d) CVP and (e-h) GridRad techniques. The black line overlaid on each panel represents the altitude of the aircraft with time. Vertical data spacing in the CVP is 50 m, and the sector size is 20 km in range and 20° in azimuth. Vertical profiles of GridRad data are created using data averaged over a nine-by-nine gridbox surrounding the closest longitude-latitude point to the aircraft location at the beginning of each minute.

removed for time periods where there were temporal gaps in CVP data (explained in section 4.1), so each subplot in Fig. 4.7a-d represents the same time period as the corresponding subplot in Fig. 4.7e-h. Each variable shows interesting similarities and differences between the CVP and GridRad vertical profile.

For profiles of Z, the CVP and GridRad profiles are fairly similar, except for isolated periods of erroneously high extents of $Z > 20$ dBZ in the GridRad profile. In profiles of Z_{DR}, values of Z_{DR} above the ML in the GridRad profile are slightly higher than those in the CVP. The GridRad technique calibrates Z_{DR} automatically, whereas for QVPs and CVPs, Z_{DR} must be calibrated by hand if the radar being used has a Z_{DR} bias. While the magnitudes are slightly different, the manual Z_{DR} calibration–calibrating the data such that values above the ML are approximately 0.2-0.25 dB, as in Ryzhkov et al. (2005a)–seems to perform well when compared to the GridRad values for Z_{DR}. However, for low values of Z_{DR}, even small fluctuations of Z_{DR} values can cause large fluctuations in calculations ingesting Z_{DR} values, such as microphysical retrievals. The effects of low Z_{DR} values on microphysical retrievals are explored more in section 4.6.

The vertical profiles of ρ_{hv} in Figs. 4.7c,g show similar magnitudes of ρ_{hv} values far above the ML, with values at or above 0.975. The depth of the ML is also quite similar between the two plots; however, the magnitudes of ρ_{hv} in the center of the ML are lower in the CVP than in the GridRad vertical profile for a majority of the period, especially after 6 UTC. This is likely due to the more coarse vertical resolution of GridRad data when compared to CVP data, resulting in a smoothing out the minimum value of ρ_{hv} in the center of the ML.

Comparing the CVP and GridRad vertical profiles of K_{DP} (Figs. 4.7d,h), both show local enhancement of K_{DP} from 6-12 km at the beginning of the period. Both profiles show this local maximum, prolonged enhancement of K_{DP} above the ML through the flight period, and some localized enhancement of K_{DP} below the ML near the end of the period. The GridRad vertical profile of K_{DP} struggles to resolve the ML, as shown by the dipole of high values just below low values of K_{DP} straddling 4 km. The CVP technique, conversely, seems to handle the ML well, using techniques from Griffin et al. (2018) as previously described. Strong contribution of δ to Φ_{DP} can prove problematic to calculations of K_{DP} in the ML, and is discussed in more detail in section 4.3.

Smoothing of GridRad data over a nine-by-nine gridbox proved incredibly important for K_{DP} in particular. A GridRad vertical profile of K_{DP} for this case where data was sourced from a single latitude-longitude point instead of smoothing over a nine-by-nine gridbox (not shown) showed a much noisier vertical profile. Such smoothing is recommended when GridRad data are used for applications such as vertical profiles of radar data and/or microphysical retrievals. However, CVPs likely remain the preferred choice when examining vertical profiles of polarimetric radar data due to their enhanced vertical resolution, as visible when looking at all variables in Fig. 4.7.

4.3 Comparison of QVPs Created with Various Wavelength Radars

Since the creation of the QVP technique, data from a number of sources have been analyzed via the use of QVPs. These include data from various wavelength radars, including S- (Schrom and Kumjian, 2016; Van Den Broeke et al., 2016; Kumjian and Lombardo, 2017; Troemel et al., 2017; Ryzhkov et al., 2017), C- (Kumjian et al., 2016; Montopoli et al., 2017), and X-band radars (Sulia and Kumjian, 2017). However, no investigations have been done about how QVPs of the same precipitation using data collected from radars of different wavelengths compare. This cross comparison of QVPs using data collected at different wavelengths is particularly interesting, because it allows for better understanding of different signatures seen in QVPs at various wavelengths, and whether those signatures are a result of the different precipitation structures sampled by, or of the different wavelengths of, these radars.

Cursory comparison of QVPs of the same precipitation using data collected by radars of different wavelengths is the first step in understanding the differences between such QVPs. Data collected during PECAN provide a unique opportunity to compare QVPs at multiple wavelengths, due to the variety of instrumentation and radars deployed during the campaign. As long as the radars are primarily sampling the trailing stratiform region and not the leading convective line, MCSs lend themselves well to doing this type of cross-comparison of QVPs.

An opportunity to compare QVPs from multiple wavelength radars presented itself during the MCS observed on July 6, 2015. Both KFSD and the dual-polarized X-band mobile radar NOAA X-POL (NOXP) sampled robust stratiform precipitation from 7-8 UTC, with a nearly horizontally homogeneous echo sampled by both radars. Figure 4.8 shows PPI images of data collected at 0.5 degree elevation from two similar times for both of these radars. The box in Fig. 4.8a-b shows the zonal and meridional extent of Fig. 4.8c-d, with the location of NOXP denoted by the black dot. Although some convection is evident in the S-band radar data, the majority of the echo sampled by both radars was stratiform precipitation, making an analysis of the vertical structure of such precipitation using the QVP technique appropriate. C-band radar data from the Shared Mobile Atmospheric Research and Teaching radars (SMART-R; Biggerstaff et al., 2015) were collected on this day but are not used for QVP analyses, as SMART-R1 did not have dual-polarization capabilities, and SMART-R2 was not collecting data during this time period. At the time of data collection, NOXP was sited approximately 56 km southwest of KFSD. This means that the precipitation that both radars were scanning was analogous, but cannot be assumed to be identical, even though the data were collected at the same time. Values of Z in Fig. 4.8 are considerably lower in PPIs of NOXP data than of KFSD data within the box in

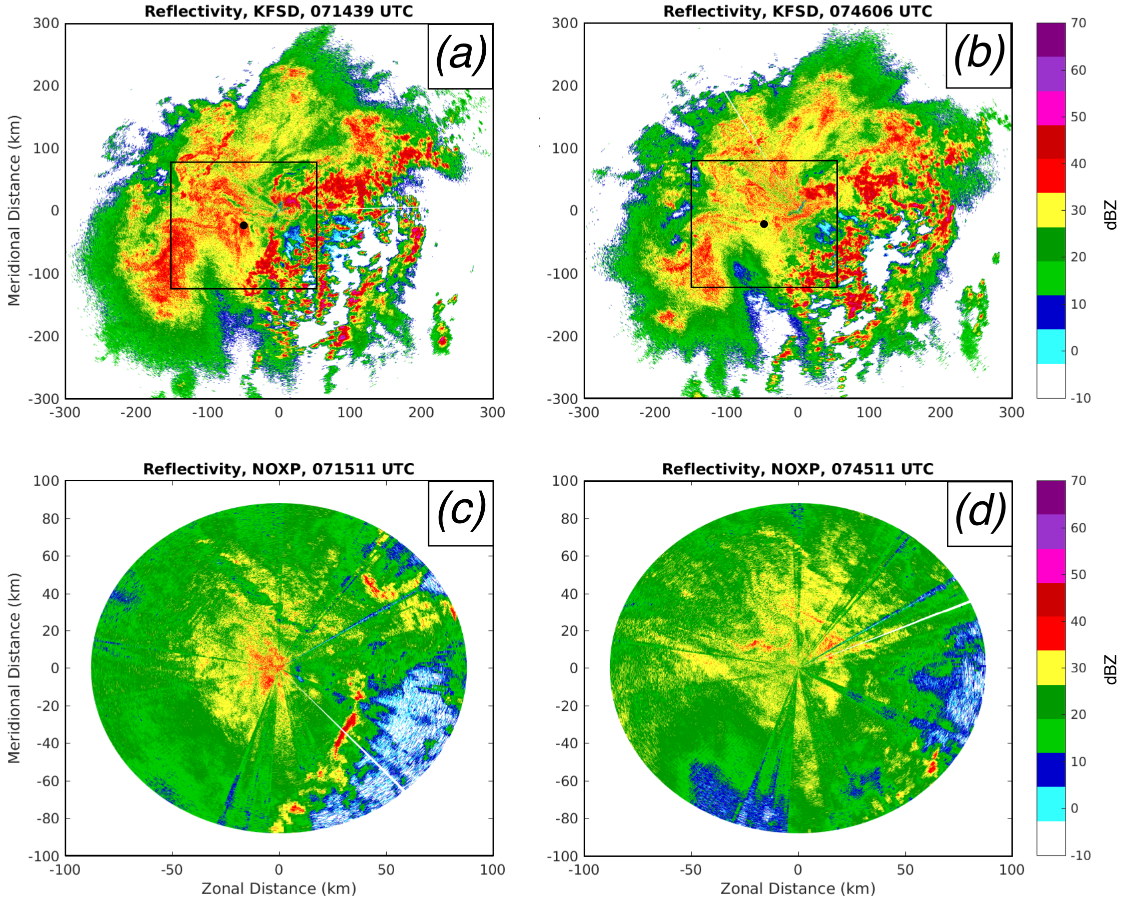

Figure 4.8: PPI scans of reflectivity at 0.5 degrees elevation from (a-b) KFSD and (c-d) NOXP, at scan times closest to (a,c) 7:15 and (b,d) 7:45 UTC. Note that the meridional and horizontal extents of the images are 300 km for (a-b) and 100 km for (c-d), and that the colorbar is different from the QVP and CVP colorbar. The box in (a-b) shows the zonal and meridional extent of (c-d), with the location of NOXP denoted by the black dot.

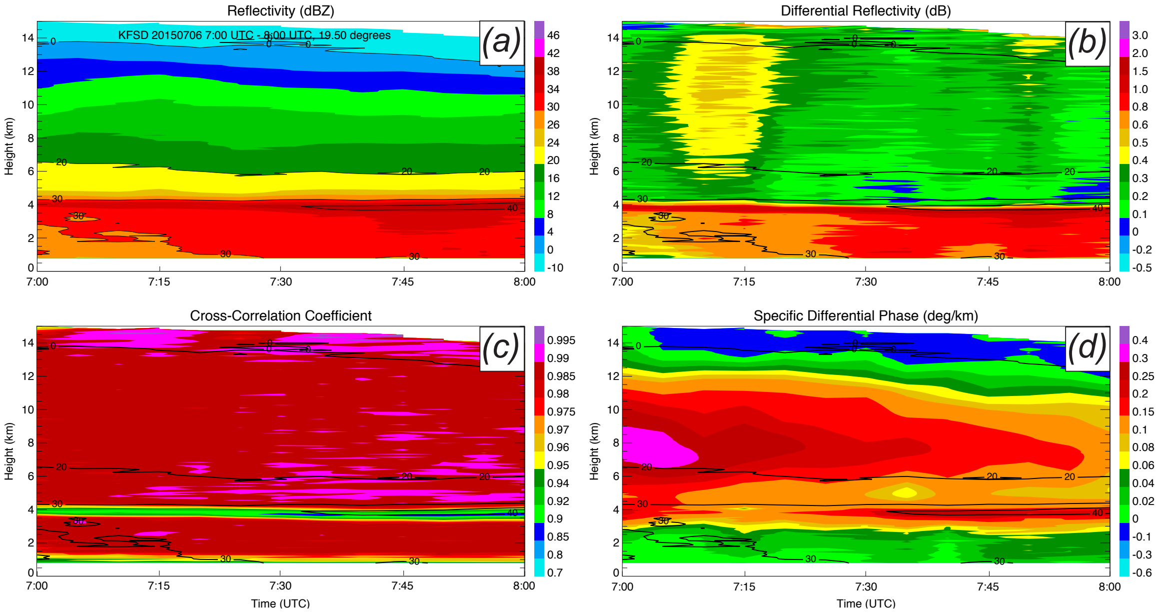

Figure 4.9: QVP of Z (a), Z_{DR} (b), ρ_{hv} (c), and K_{DP} (d) from 7-8 UTC on July 6, 2015, using data from the KFSD radar.

Fig. 4.8a-b where NOXP data were collected. This is likely due to beam attentuation at X-band as the beam passed through regions of enhanced reflectivity (upwards of 35-40 dBZ as sampled by KFSD; Fig. 4.8a-b). Radar miscalibration could also have played a role.

Figures 4.9 and 4.10 show QVPs of Z, Z_{DR}, ρ_{hv}, and K_{DP} using KFSD and NOXP radar data, respectively. The KFSD QVP was created using data from the 19.50° elevation angle, and the NOXP QVP using 18.00° elevation angle data. For the KFSD QVP, Z_{DR} in Fig. 4.9 was calibrated such that values just above the melting layer were approximately 0.2 dB (Ryzhkov and Zrnic, 1998; Ryzhkov et al., 2005a). For the NOXP QVP in Fig. 4.10, Z_{DR} and Z were calibrated such that values below the melting layer were approximately equal to those for KFSD, requiring calibration of +0.1 dB and +3 dBZ through the entire depth of the QVP, respectively. This allowed for investigations of how attenuation through the ML affected Z and Z_{DR} at X-band, relative to how it affected those variables at S-band.

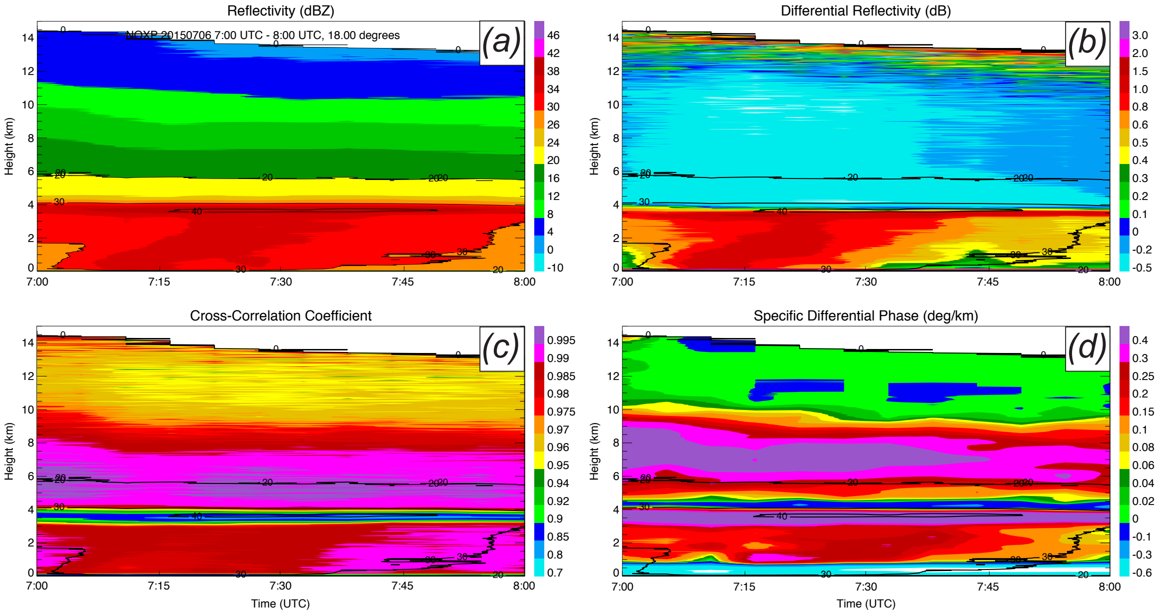

Figure 4.10: QVP of Z (a), Z_{DR} (b), ρ_{hv} (c), and K_{DP} (d) from 7-8 UTC on July 6, 2015, using data from the NOXP radar.

A number of interesting signatures within and differences between these two plots are immediately noticeable. First, the plots themselves show qualitative agreement in the precipitation structures they resolve. Both show a melting layer at approximately 4 km, high K_{DP} at 8 km that gradually decreases during the hour long time period, and cloud top heights near 14-15 km at 7 UTC, gradually descending to closer to 13-14 km by 8 UTC. Despite these similarities, there are also a number of stark differences between these plots. Z_{DR} above the melting layer is considerably lower for the NOXP QVP, despite correction of Z_{DR} below the melting layer to be approximately equal to that measured by KFSD. This is indicative of strong beam attenuation in the bright band, preferentially attenuating the H-polarized beam and lowering Z_{DR} above the melting layer as a result. Also, above about 9 km, ρ_{hv} in the NOXP QVP is fairly low, dropping to values near 0.95. This artificial decrease in ρ_{hv} is thought to be due to low signal to noise ratio at distances farther from the radar. These signatures persist in these images because no correction of NOXP data was done for low SNR or for attenuation.

Additionally, there are obvious issues with K_{DP} in and around the melting layer for NOXP. Just below the melting layer, K_{DP} is incredibly high, above 0.4 deg/km, while just above the melting layer, K_{DP} drops dramatically down to below zero. This dramatic change in K_{DP} happens over the span of less than a kilometer, and is due to high backscatter differential phase (δ) in the melting layer. Figure 4.11 shows the vertical profile of Φ_{DP} from the fifth volume scan performed by each radar during the hour. Magnitudes of Φ_{DP} are considerably higher for NOXP than KFSD, with peak values of δ in the ML higher for NOXP as well. Also, while the local peak in Φ_{DP} for KFSD is quite limited in vertical extent, spanning only about 0.5 km, the peak for NOXP has a much larger vertical extent. Calculations of K_{DP} in and around the ML for NOXP may be suffering from the much larger vertical extent of this peak, or potentially from the concavity of the profile from approximately 4-5 km. Depending on how K_{DP} is calculated in this region, this concavity could be a main contributor in the "dipole" of high and low K_{DP} just below and above the ML. This problem with appropriately calculating K_{DP} in the ML for shorter wavelength radars is a concern that needs to be addressed in the future.

Above the melting layer, however, K_{DP} is fairly robust in both the NOXP and KFSD QVPs. In the region from 6-10 km, K_{DP} as measured by NOXP is approximately twice that measured by KFSD, just below the factor of 3 increase from S to X band measurements of K_{DP} predicted by theory. Because K_{DP} is not affected by radar miscalibration or attenuation, it remains a robust estimate despite calibration and attenuation challenges.

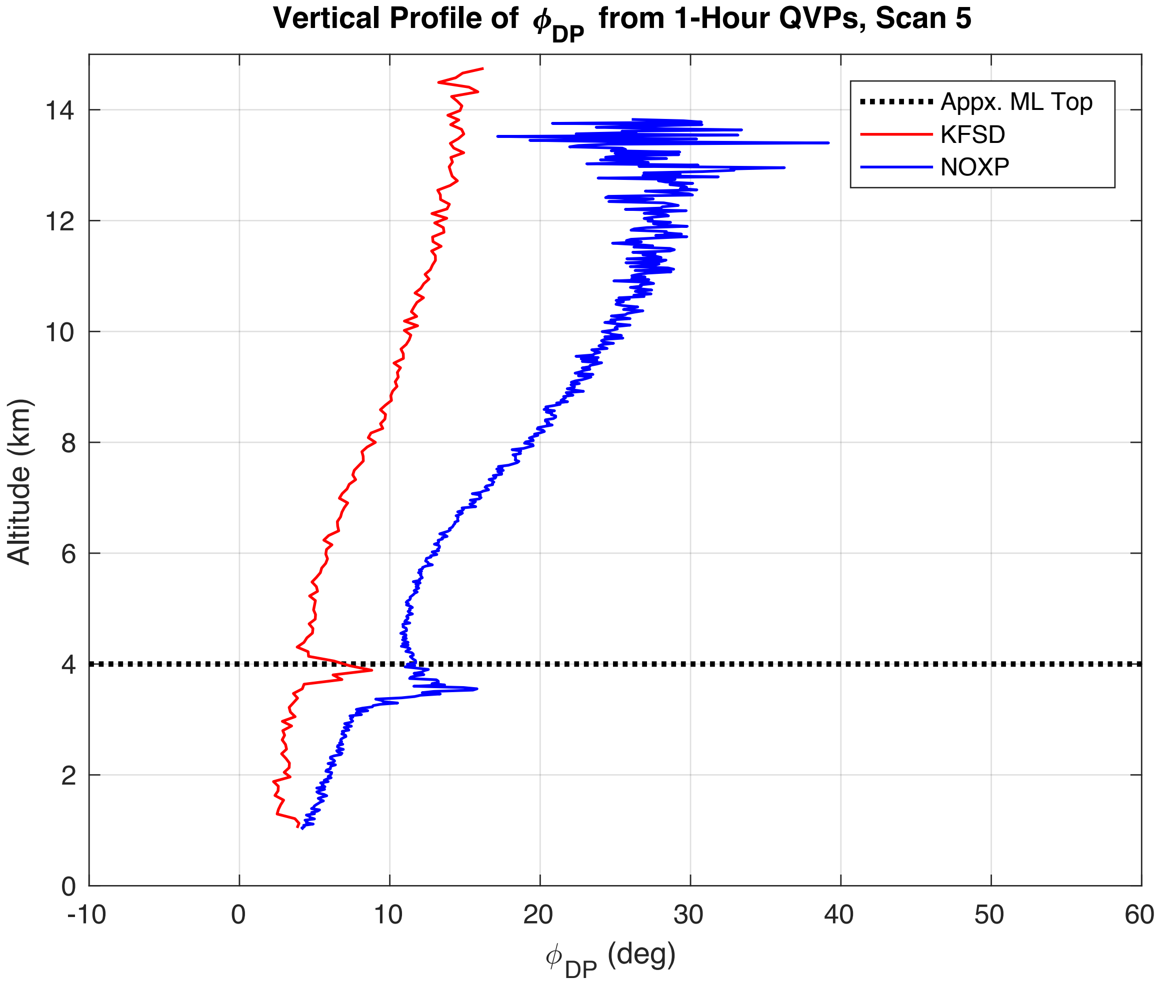

Figure 4.11: Vertical profiles of Φ_{DP} from the fifth volume scan performed by the KFSD (red) and NOXP (blue) radars. The approximate top of the melting layer is denoted by the horizontal dotted line.

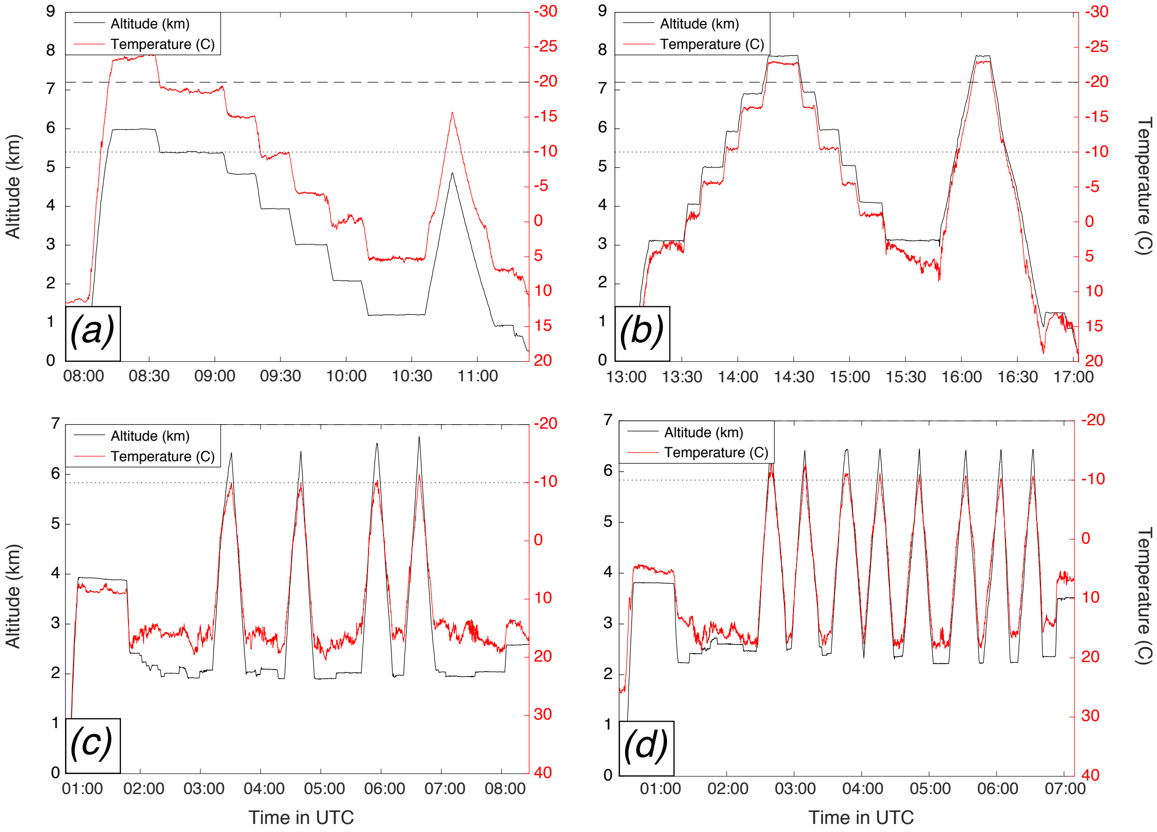

Figure 4.12: Time series plots of altitude (black, in km) and temperature (red, in °C) along the flight tracks of IOPs from (a) April 27, 2011, (b) May 20, 2011, (c) July 6, 2015, and (d) July 9, 2015. Dotted and dashed lines are placed at the -10 and -20 °C levels, respectively.

4.4 Bulk Microphysical Properties of MCS Stratiform Precipitation

The flight patterns in MC3E and PECAN both included spiral ascents and descents, but flights in MC3E targeted regions high above the ML (such as the DGL), whereas flights in PECAN mainly flew transects through the ML. Figure 4.12 shows time series plots of altitude and temperature along the flight paths for the full extent of the flights performed during the 4 cases discussed in section 3.1. Because these campaigns primarily sampled different temperature regions, an opportunity exists to separately examine the vertical profiles of D_{mm}, N_t, and IWC through the ML and DGL. It must be noted that Lagrangian sampling was not performed during these spirals, so the following investigations are of vertical data trends, from which processes are inferred. For investigations of the vertical structure of the DGL using MC3E data, the focus will be solely on the downward spiral performed on May 20, 2011, since the spiral on April 27, 2011 only reached temperatures as low as -15.5 °C (Fig. 4.12a), making an examination of the full vertical extent of the DGL impossible.

To examine the vertical structure of the DGL, Fig. 4.13 shows box and whisker plots of D_{mm}, N_t, and IWC using 2D-C data for the downward spiral on May 20, 2011, with data binned into 2 °C intervals from -5 to -25 °C, as well as a vertical profile of relative humidity with respect to ice (RH_i). Boxes show the 25th, 50th, and 75th percentiles, with whiskers at the 5th and 95th percentiles. Data within each temperature bin were analyzed if there were 40 or more samples (i.e., seconds of data) in the bin, to ensure a large enough sample size (e.g., Murphy et al., 2017). A few signatures stick out in these vertical profiles. First, IWC and D_{mm} increase through the depth of the DGL, with median values of IWC increasing from 0.13 to 0.22 g/m^3, and D_{mm} from 512.5 to 750 μm from the -21 to -19 °C bin to the -13 to -11 °C bin. From the top to the bottom of the DGL, however, N_t remains fairly constant, with median values only increasing from 28.2 to 33.5 L^{-1} from the -21 to -19 °C bin to the -13 to -11 °C bin, with a local maximum median value of 38.5 L^{-1} in the -15 to

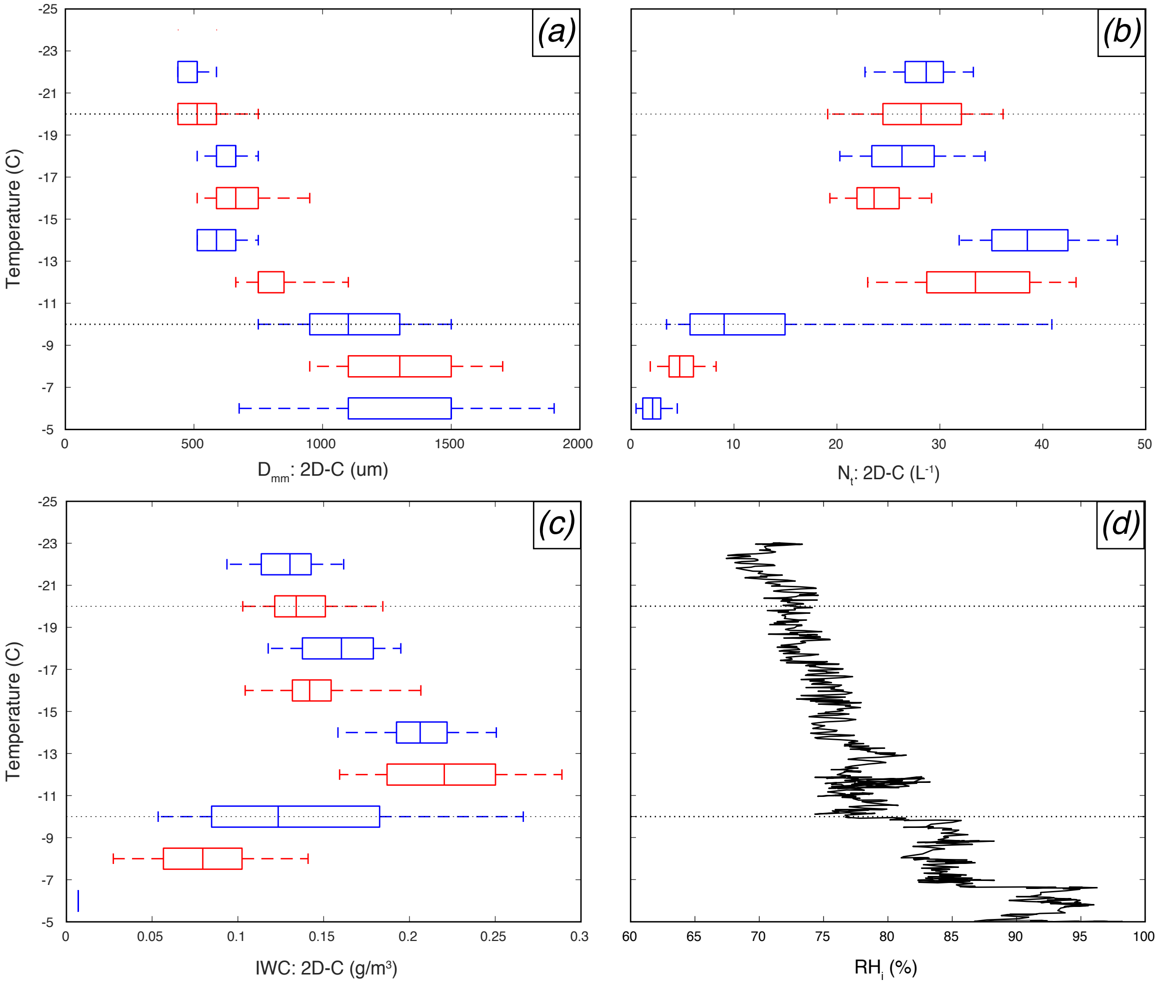

Figure 4.13: Box and whisker plots of (a) D_{mm}, (b) N_t, and (c) IWC from the 2D-C probe for the downward spiral on May 20, 2011, with data binned into 2 °C intervals from -5 to -25 °C. Boxes show the 25th, 50th, and 75th percentiles, with whiskers at the 5th and 95th percentiles. Box and whiskers for each temperature bin are shown only if there are 40 or more samples in the given bin. Dashed lines are placed at -10 and -20 °C. Panel (d) shows the vertical profile of RH_i through the same temperature range. Temperature increases downward to mimic typical atmospheric temperature structure.

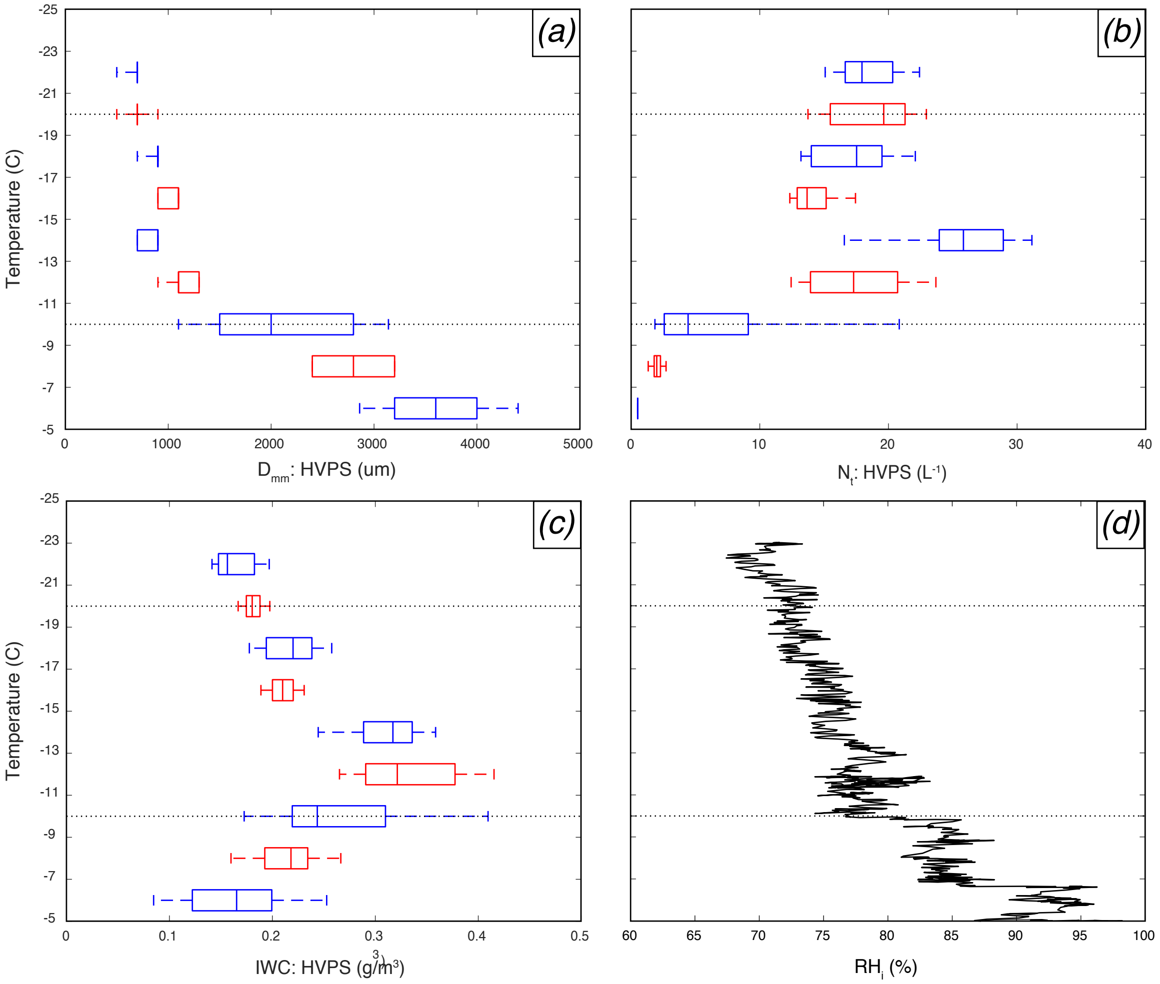

Figure 4.14: As in Fig. 4.13, but using data from the HVPS probe.

-13 °C bin. At a first glance, these vertical profiles suggest particle growth via vapor deposition in the absence of aggregation. However, looking at Fig. 4.13d, along the flight track, values of RH_i ranged from 70.6% to 83.3% within the DGL, indicating subsaturated air with respect to ice. Therefore, sublimation, and not depositional growth, is expected. Examining the 18 UTC sounding launched from Lamont, OK, located just NW of the ARM SGP CF, strong southerly winds ranging from 46 to 55 knots were sampled between the -10 and -20 °C levels. This could indicate that horizontal advection of ice crystals may be responsible for increasing IWC within the DGL for this storm, as typical crystal fall speeds are approximately 1 m/s, which pale in comparison to the observed southerly winds at near 25 m/s. This is one of the dangers of using a Lagrangian-type interpretation of these data.

At the bottom of the DGL and just below, IWC values drop off sharply, with median values dropping to 0.12 g/m^3 in the -11 to -9 °C bin and 0.08 g/m^3 in the -9 to -7 °C bin. This occurs concurrently with a jump in median D_{mm} values to 1.1 and 1.3 mm, and a decrease in median N_t values to 9.0 and 4.7 L^{-1} in the same bins. The marked increase in D_{mm} at temperatures warmer than -10 °C in conjunction with a rapid decrease in N_t is potentially indicative of aggregation. Sublimation of particles may also be occuring, preferentially sublimating the smallest particles, therefore increasing D_{mm}, decreasing N_t, and decreasing IWC. This sublimation is plausible, as the Lamont, OK 18 UTC sounding showed subsaturated air between the bottom of the DGL and top of the ML, model soundings indicated the presence of subsaturated air in the environment just ahead of the MCS at temperatures lower than 10 °C (Xue et al., 2017), and values of RH_i in Fig. 4.13 remain below 100% through the depth of the profile. A decrease in IWC is also possible due to increased fall speeds of larger hydrometeors. A similar trend is seen in the HVPS data (Fig. 4.14). From the -21 to -19 °C bin to the -13 to -11 °C bin, median IWC values increase from 0.18 to 0.32 g/m^3, and median D_{mm} values increase from 700 μm to 1.1 mm, while median N_t values are very similar at the top and bottom of the DGL, decreasing from 19.6 to 17.3 L^{-1}. Below the DGL, a decrease in IWC and N_t is observed, with median IWC values dropping to 0.24 and 0.22 g/m^3, and median N_t values dropping to 4.4 and 2.0 L^{-1}, in the -11 to -9 °C and -9 to -7 °C bins. In addition, D_{mm} increases rapidly below the DGL, to values of 2.0 and 2.8 mm in the -11 to -9 °C and -9 to -7 °C bins, and even further to 3.6 mm in the -7 to -5 °C bin.

Transitioning from an examination of the vertical structure of the DGL to that of the ML, Figs. 4.15-4.20 show box and whisker plots of D_{mm}, N_t, and IWC using CIP data for multiple downward spirals on July 6 and July 9, 2015, with data binned into 2 °C intervals from 10 to -10 °C. Boxes show the 25th, 50th, and 75th percentiles, with whiskers at the 5th and 95th percentiles. These plots differ from Fig. 4.13 and 4.14 in that for profiles of RH, since these plots show data at temperatures both above and below 0 °C, the vertical profile of RH_i is plotted at temperatures below 0 °C, and RH is plotted at temperatures above 0 °C, as in Fig. 2 in McFarquhar et al. (2007). Again, only bins with 40 or more samples are included in Figs. 4.15-4.20. Additionally, as these plots investigate regions at temperatures greater than 0 °C, box and whiskers are only shown for bins at temperatures above 0 °C where median IWC values are greater than or equal to 0.01 g/m^3, to mitigate investigating regions of predominantly liquid water and no longer of ice. For brevity, 2 of the 4 spirals performed on July 6, 2015, and 4 of the 8 performed on July 9, 2015 are examined here.

Spirals on July 6, 2015 show an increase of median values of D_{mm} from 1.175 to 1.325 mm and 950 μm to 1.325 mm from the -10 to -8 °C bin to the -2 to 0 °C bin in Figs. 4.15 and 4.16, respectively. This increase in D_{mm} is concurrent with decreases in N_t and IWC, with median values of N_t decreasing from 34.3 to 1.6 L^{-1} and IWC decreasing from 0.29 to 0.04 g/m^3 from the -10 to -8 °C bin to the -2 to 0 °C bins in Fig. 4.15, and median values of N_t decreasing from 65.0 to 3.6 L^{-1} and

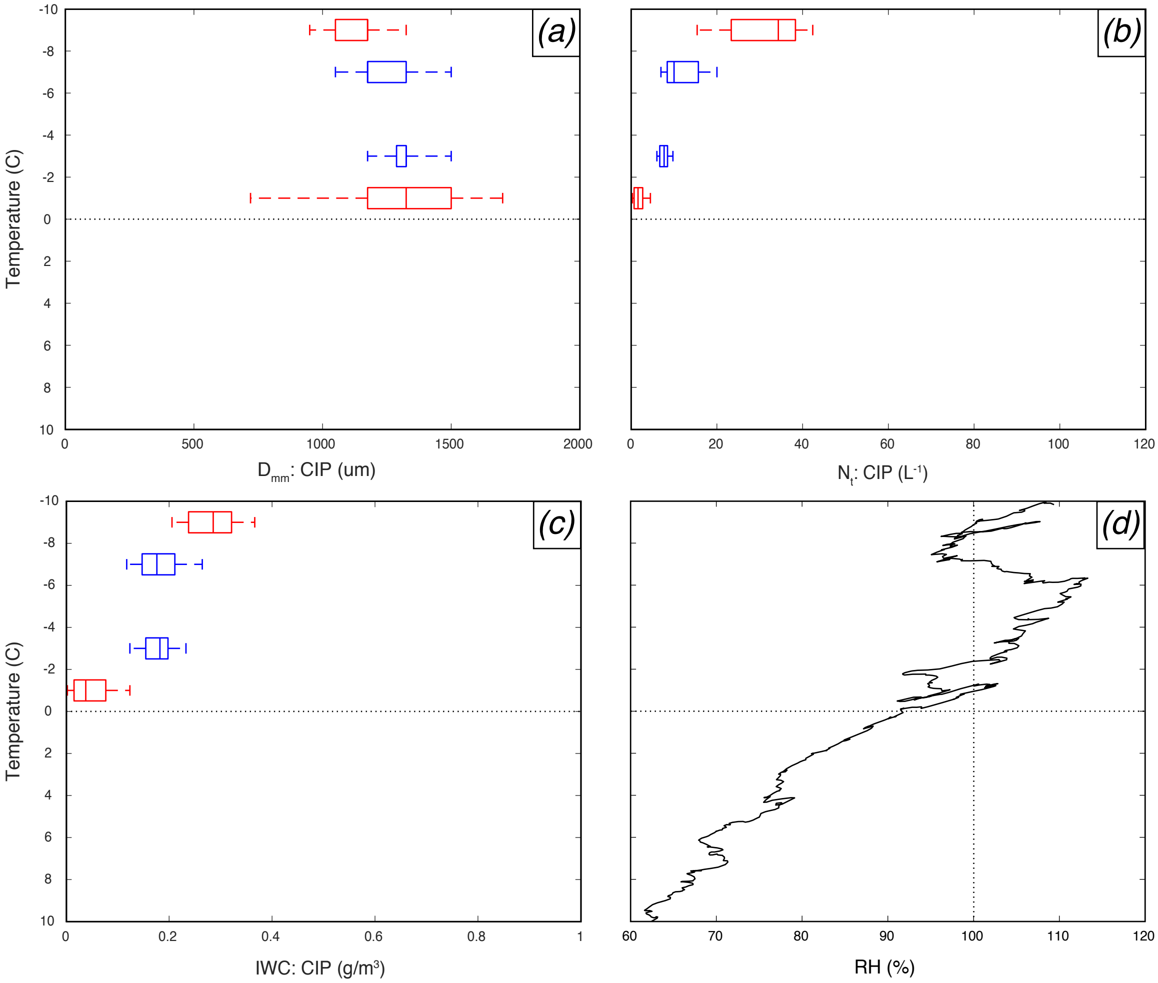

Figure 4.15: Box and whisker plots of (a) D_{mm}, (b) N_t, and (c) IWC from the CIP probe for the second downward spiral on July 6, 2015. Data are binned into 2 °C intervals from 10 to -10 °C. Boxes show the 25th, 50th, and 75th percentiles, with whiskers at the 5th and 95th percentiles. Box and whiskers for each temperature bin are shown only if there are 40 or more samples in the given bin. Panel (d) shows the vertical profile of RH_i at temperatures below 0 °C, and RH at temperatures above °C, through the same temperature range. Dashed lines are placed at 0 °C and 100% RH. Temperature increases downward to mimic typical atmospheric temperature structure.

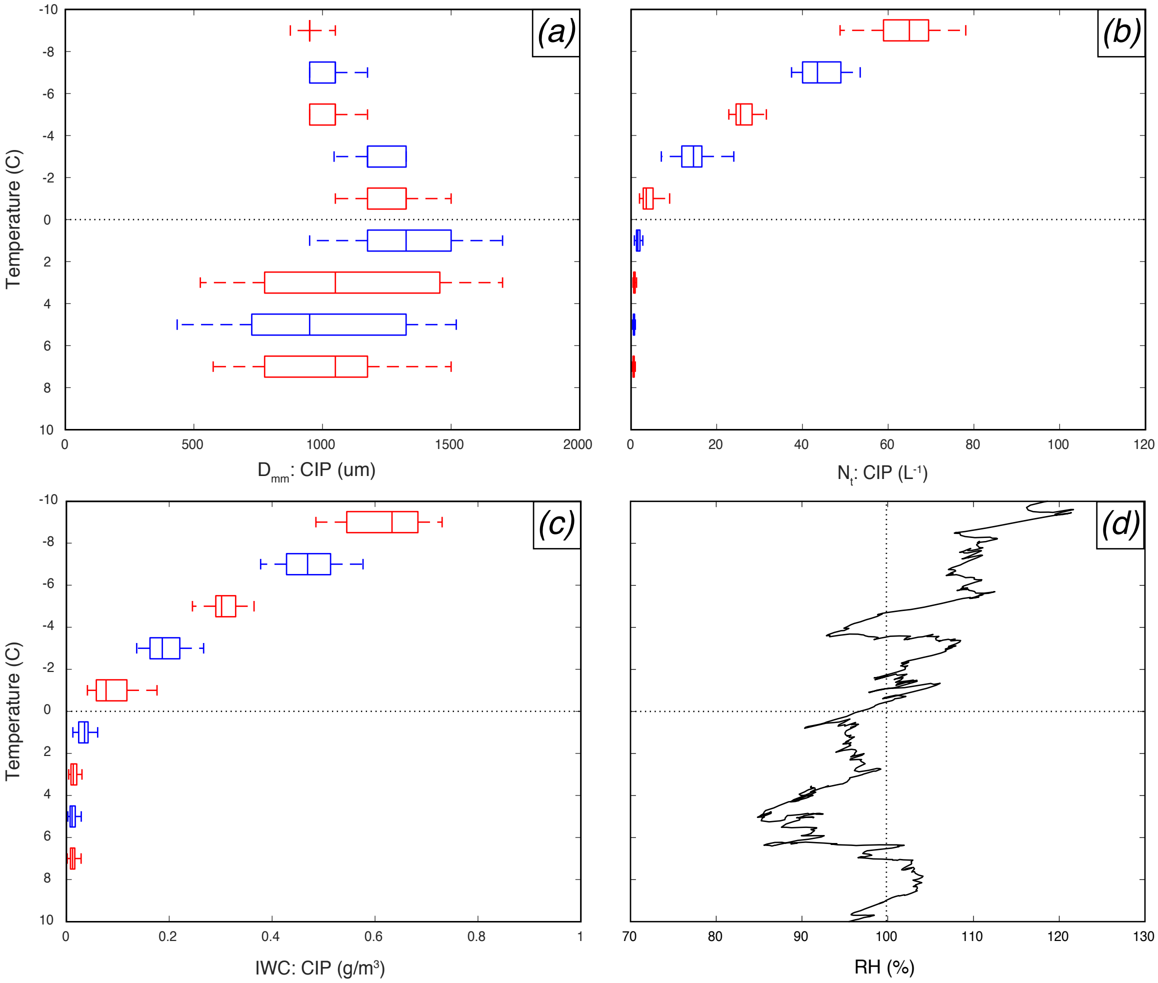

Figure 4.16: As in Fig. 4.15, but for the fourth downward spiral.

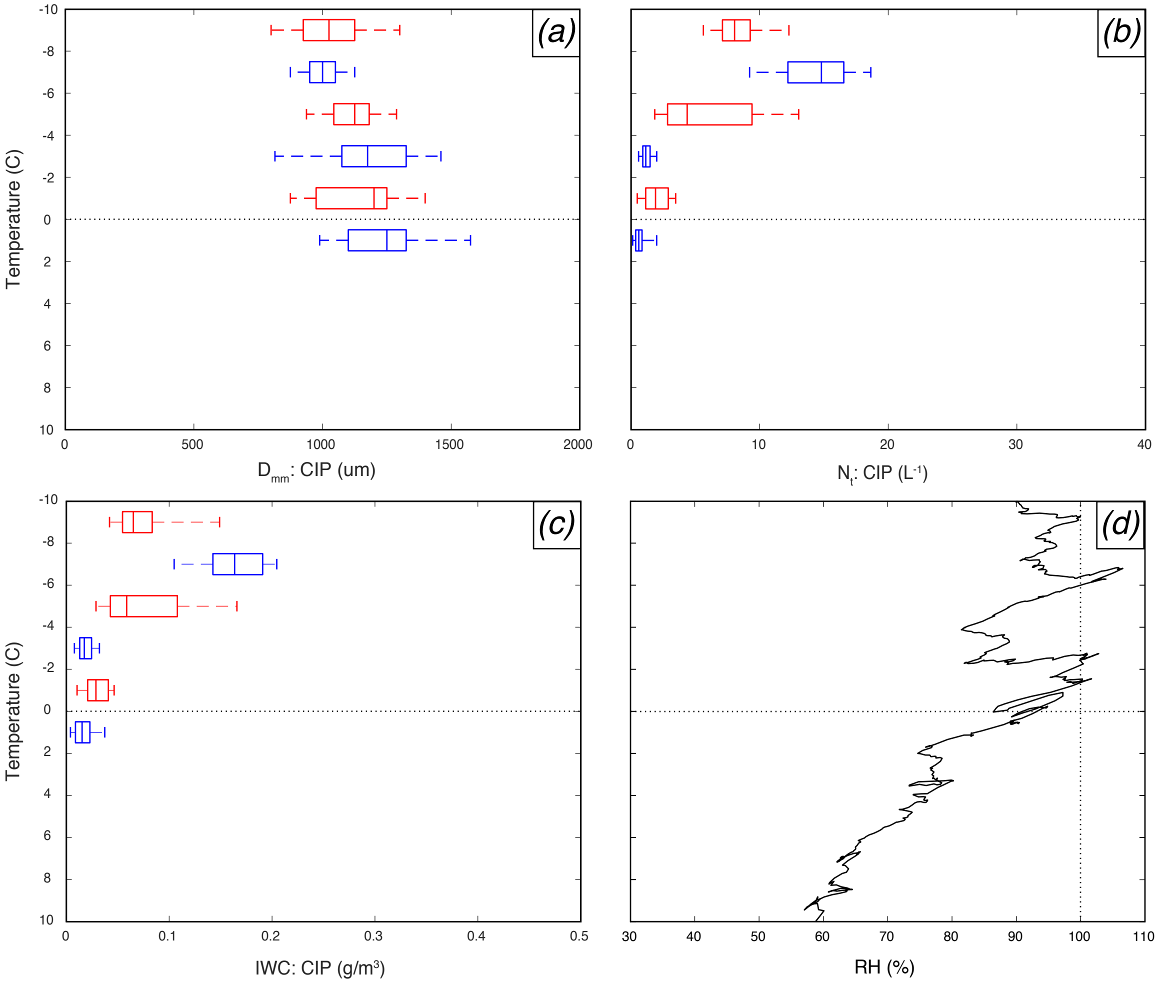

Figure 4.17: Box and whisker plots of (a) D_{mm}, (b) N_t, and (c) IWC from the CIP probe for the third downward spiral on July 9, 2015. Data are binned into 2 °C intervals from 10 to -10 °C. Boxes show the 25th, 50th, and 75th percentiles, with whiskers at the 5th and 95th percentiles. Box and whiskers for each temperature bin are shown only if there are 40 or more samples in the given bin. Panel (d) shows the vertical profile of RH_i at temperatures below 0 °C, and RH at temperatures above 0 °C, through the same temperature range. Dashed lines are placed at 0 °C and 100% RH. Temperature increases downward to mimic typical atmospheric temperature structure.

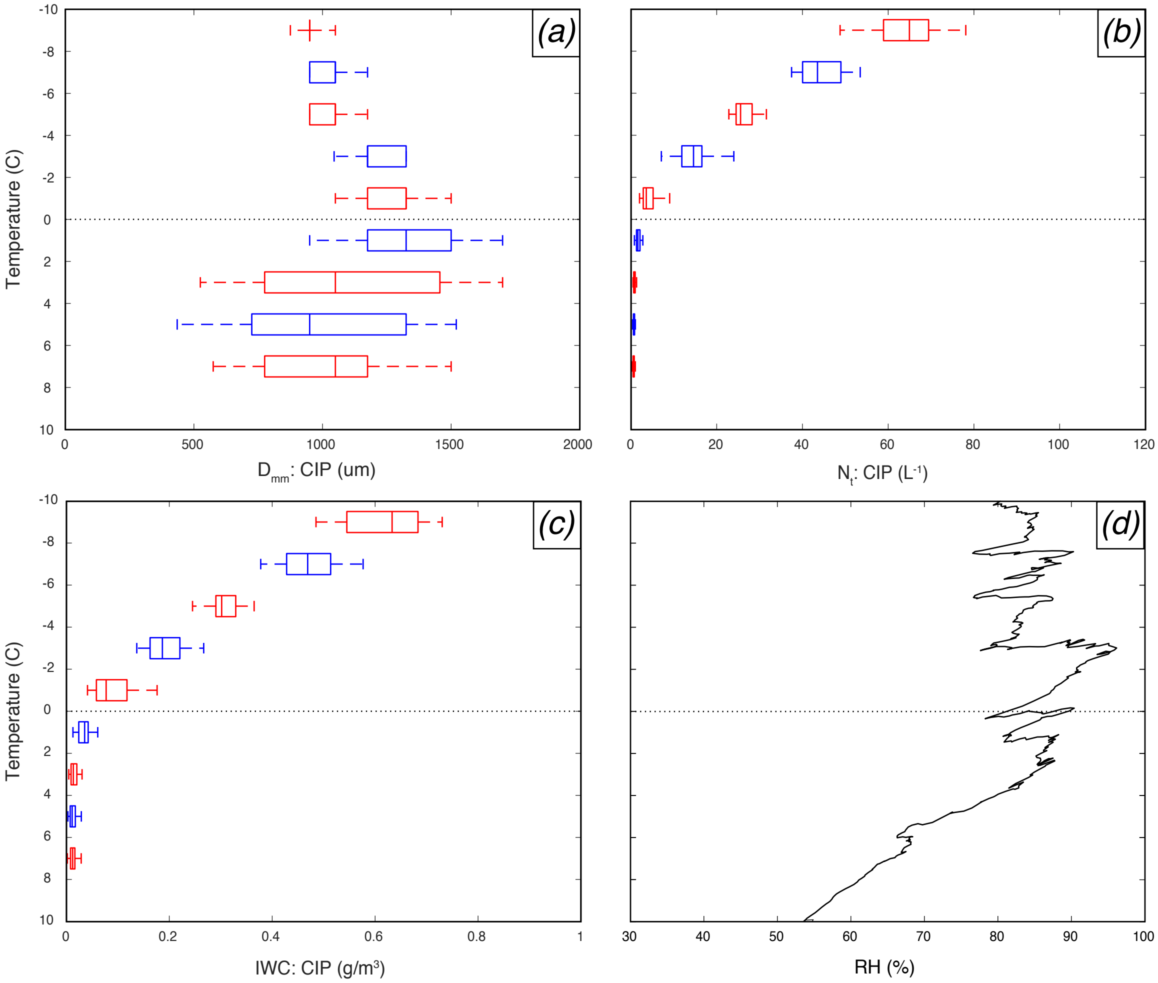

Figure 4.18: As in Fig. 4.17, but for the fourth downward spiral.

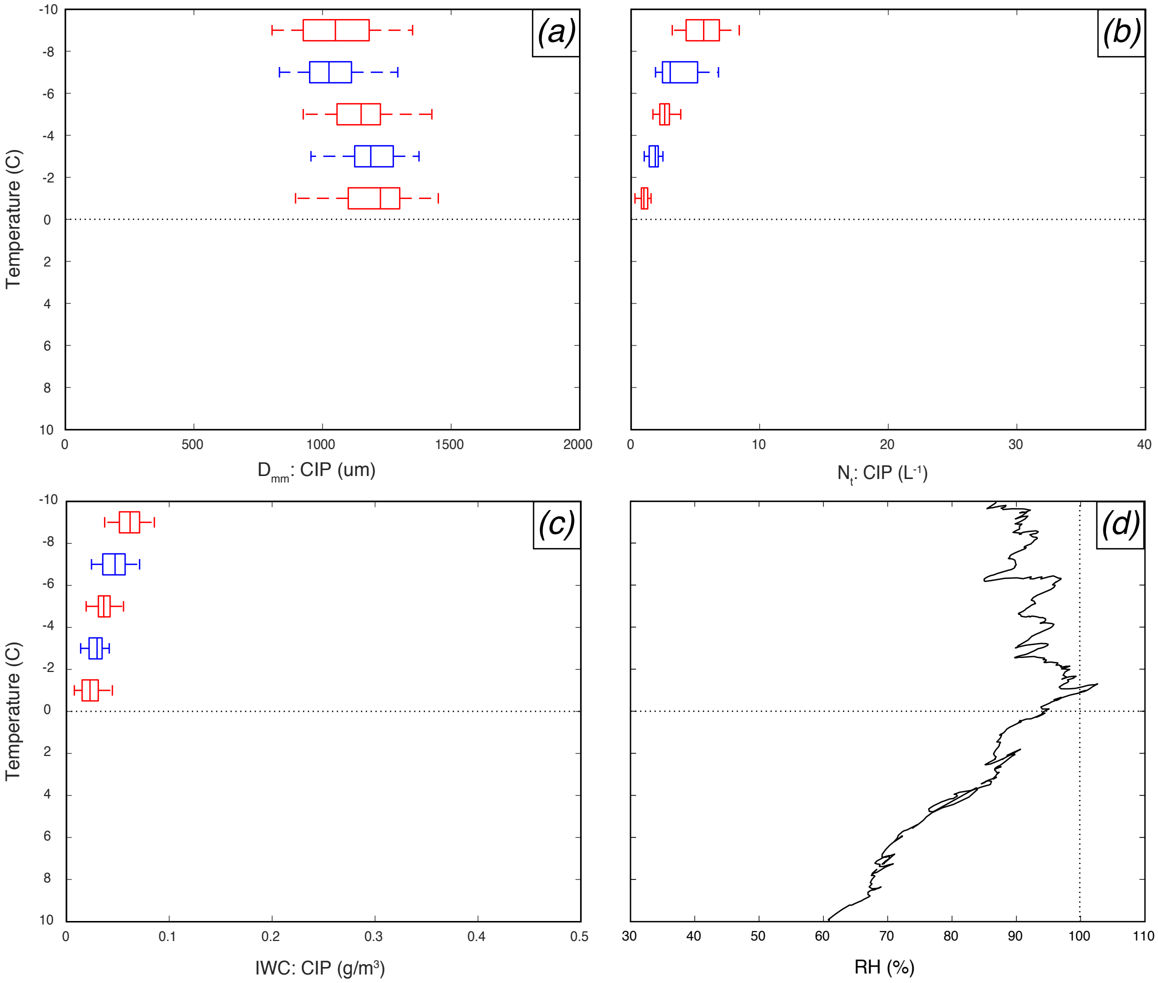

Figure 4.19: As in Fig. 4.17, but for the fifth downward spiral.

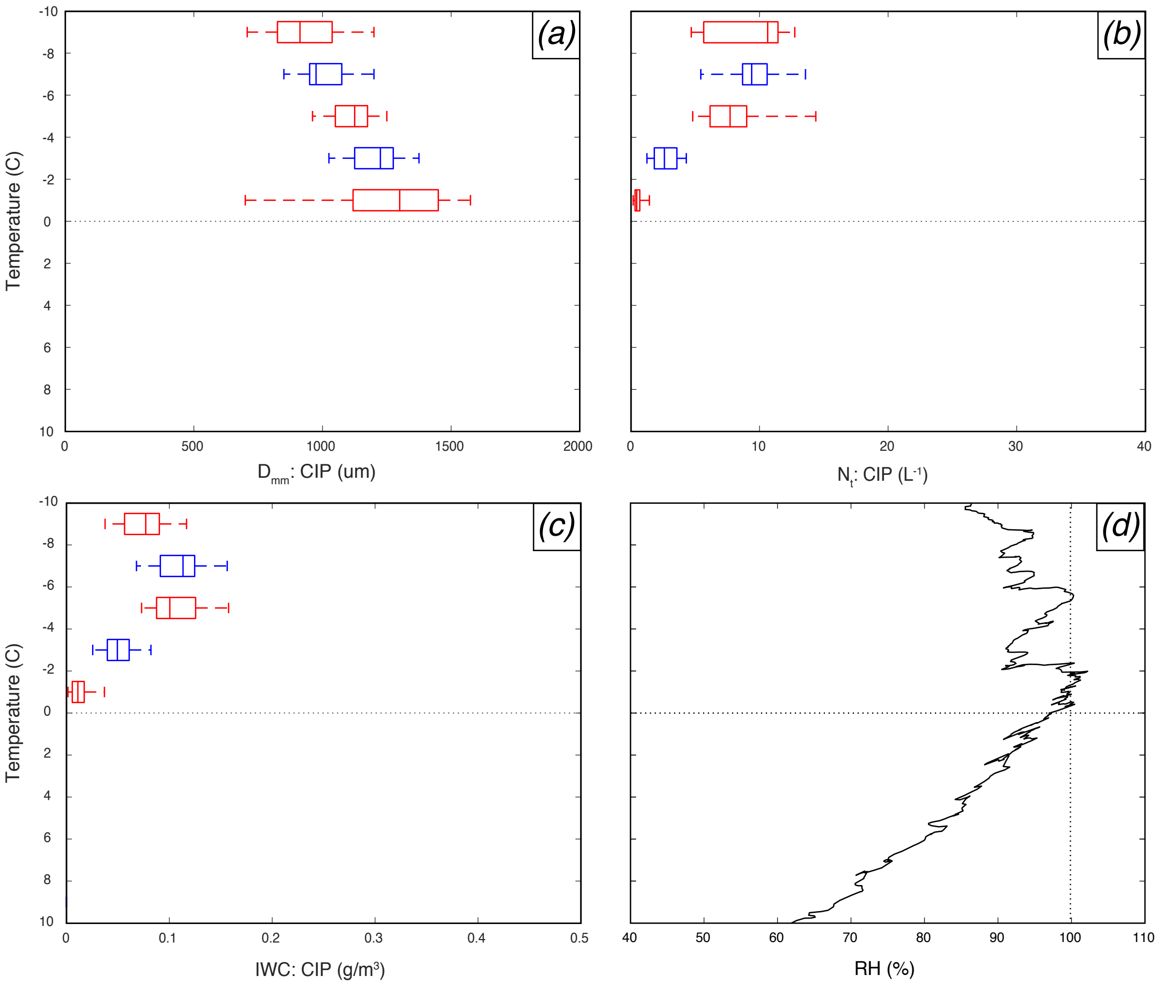

Figure 4.20: As in Fig. 4.17, but for the sixth downward spiral.

IWC decreasing from 0.63 to 0.08 g/m^3 from the -10 to -8 °C bin to the -2 to 0 °C bins in Fig. 4.16. The pattern of increasing D_{mm} and decreasing N_t is indicative of particle aggregation with depth, while a decrease in IWC is likely indicative of particle sublimation within dry air typically found in these types of systems. Looking at Fig. 4.15d, RH_i was greater than 100% from approximately -7 to -2 °C. From the -8 to -6 °C bin to the -4 to -2 °C bin where RH_i was above 100%, IWC remains constant, with a median value of 0.18 g/m^3 in all three bins (even the bin from -6 to -4 °C, which is not shown due to having less than 40 samples). This makes sense, as sublimation would not occur in regions where $RH_i > 100\%$. However, during spiral 4 (Fig. 4.16), a decrease in IWC values is seen even while the aircraft was sampling RH_i values above 100%. Although values dip below 100% around -4 °C, IWC decreases through the entire vertical extent from -10 to 0 °C in Fig. 4.16c. Some potential reasons for a decrease in IWC even in an environment with $RH_i > 100\%$ could be an increase in terminal velocity of the particles as they grow in size, falling faster as aggregation continues through the -10 to -8 °C layer, and/or riming, with an increase in ice mass significantly outweighed by the increase in terminal velocity. Additionally, horizontal advection of ice hydrometeors out of the sample volume may be occuring, causing the opposite effect as what was seen in Figs. 4.13 and 4.14, where IWC was increasing in a subsaturated environment with respect to ice. The sounding from Aberdeen, SD at 0 UTC showed westerly winds between 0 and -10 °C from 25 to 40 knots, and at 12 UTC from 40 to 45 knots. The exact reason is unknown at this time, and more investigation must be done into what could be causing this decrease in IWC towards the ML in an environment of $RH_i > 100\%$.

On July 9, across all spirals, there is an obvious increase in D_{mm}, decrease in N_t, and decrease in IWC, again pointing toward aggregation occuring alongside particle sublimation. Unlike July 6, values of RH_i remain below 100% for almost the entire vertical extent from -10 to 0 °C during each of the 4 spirals, supporting the idea of particle sublimation contributing to a decrease in IWC. There are a few regions in which RH_i exceeds 100%, however. During the third spiral (Fig. 4.17), N_t and IWC are locally maximized in the -8 to -6 °C bin, with N_t increasing to 14.8 L^{-1} from 8.1 L^{-1} in the -10 to -8 °C bin, and decreasing again to 4.4 L^{-1} in the -6 to -4 °C bin. Likewise, IWC increases from 0.07 g/m^3 to 0.16 g/m^3, and decreases back down to 0.06 g/m^3, in the bins from -10 to -4 °C. On that spiral's profile of RH_i, there is a bump in RH_i values near -7 °C where RH_i increases to greater than 105%. This supports the idea of particle growth via deposition and potentially new particle nucleation in that region (as N_t increases and D_{mm} slightly decreases). Additionally, during the sixth spiral (Fig. 4.20), IWC values have a local maximum in the region from -8 to -4 °C, with values increasing from 0.08 g/m^3 in the -10 to -8 °C bin to 0.11 and 0.10 g/m^3 in the two bins from -8 to -4 °C, and back down to 0.05 g/m^3 in the -4 to -2 °C bin. That spiral's RH_i profile shows an increase of RH_i to just above 100% near -6 °C. The increase in IWC in this spiral is different from that in Fig. 4.17 in that it is paired with a still-decreasing median N_t and increasing median D_{mm}, so depositional growth is dominating over new particle nucleation, although 95th percentile values of N_t are increasing in the -8 to -4 °C temperature region. However, for all four spirals, aggregation remains the dominant particle growth mechanism from the bottom of the DGL to the ML.

On both July 6 and July 9, 2015, there are a few spirals where IWC remained above 0.01 g/m^3 below the ML. While investigations of ice microphysical processes far below the ML are not appropriate due to liquid hydrometeors dominating sample volumes, one interesting signature does show up just below the ML. In profiles of D_{mm}, specifically for spiral 4 on July 6 (Fig. 4.16) and spirals 3 and 4 on July 9 (Figs. 4.17 and 4.18), median values of D_{mm} in the 0 to 2 °C bin are slightly higher than those in the -2 to 0 °C bin. This suggests continued aggregation in the ML/below the freezing level. Heymsfield et al. (2015) also observed this behavior, concluding that aggregation was occurring starting at -4 °C and continuing to 1 °C. They noted that as particles fall into the top of the ML and continue to aggregate, an enhancement of the aggregation process may occur because the aggregates become “stickier” on their exterior as they melt and acquire a water coating, more easily collecting particles as they fall. They also found that melting continued to occur below the freezing level down to 2 °C (i.e., frozen hydrometeors persisted in sample volumes up to 2 °C), with smallest particles melting first and largest melting last. McFarquhar et al. (2007) also observed melting persisting below the freezing level, continuing at temperatures as warm as 3 °C. The conclusion that the largest particles melt last further supports an increasing median D_{mm} below the ML, since both the effects of small particles melting and large particles continuing to aggregate increase median D_{mm}.

4.5 Microphysical Retrievals of Moving CVPs

Microphysical retrievals can be performed on moving CVPs to get an estimate of the microphysical structure the aircraft was flying through. These data can be plotted much like the moving CVP data, taking into account that only data above the subjectively determined ML are ingested into the retrieval codes. Figure 4.21 shows microphysical retrievals performed on the MCS from May 20, 2011. Qualitatively, the stratiform rain contained primarily particles with diameters at or below 1.0 mm, except early in the flight near the ML. Particle concentrations were on the order of 10-100 L^{-1}, and IWC values mainly spanned from approximately 0.3 to 1.5 g/m^3. Between 13 and 14 UTC, a signature of aggregation is visible in Fig. 4.21a-b, where D_m increases and N_t decreases towards the ML.

Microphysical retrievals of moving CVP data can also be performed using data from the other two cases whose moving CVPs were examined in section 4.1. Figures 4.22 and 4.23 show microphysical retrievals performed on the MCSs from April 27, 2011 and July 6, 2015, respectively. Due to how shallow the precipitation was on April

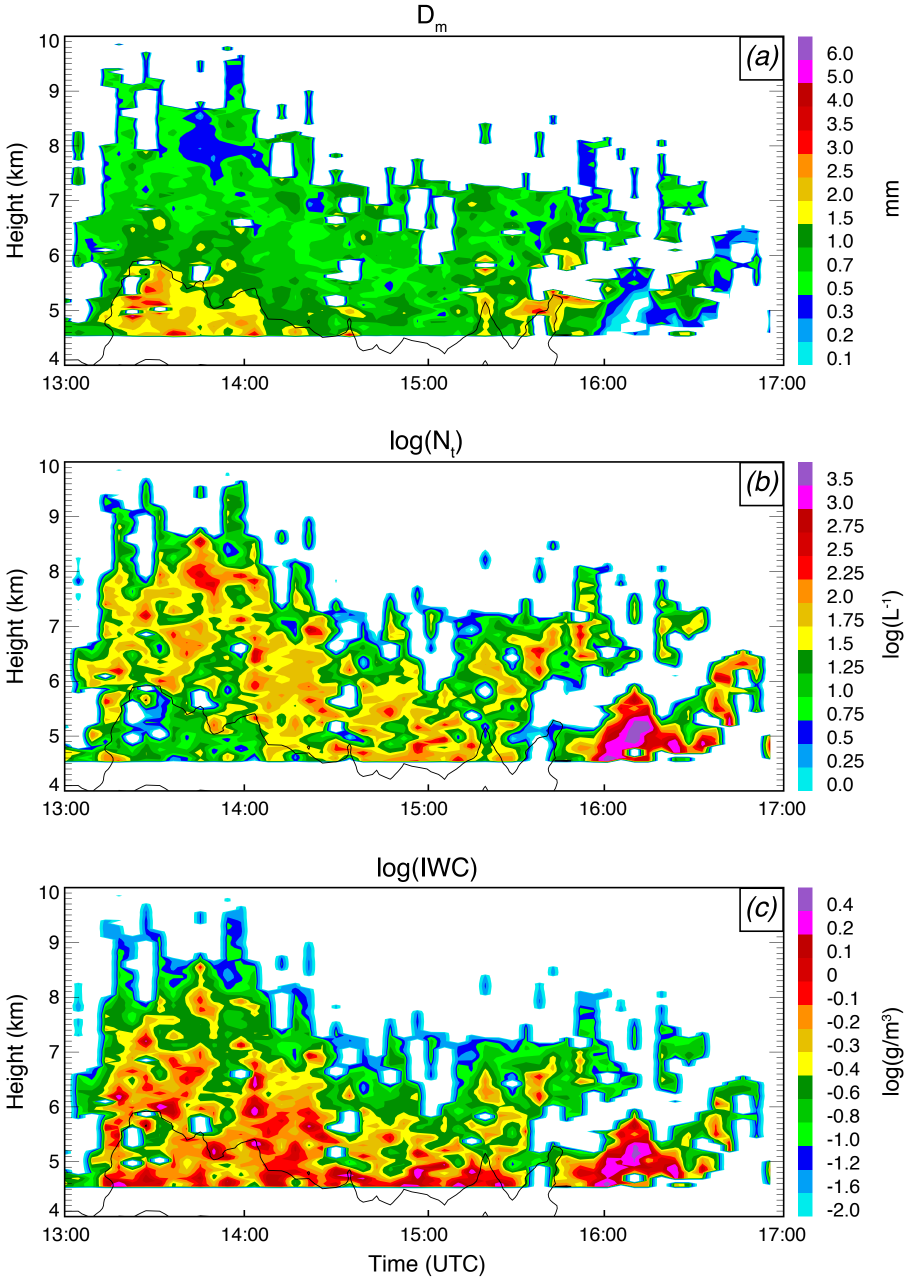

Figure 4.21: Ice microphysical retrievals performed on the May 20, 2011 moving CVP. Panels are of (a) D_m, (b) $\log(N_t)$, and (c) $\log(IWC)$. The height of the ML was subjectively determined to be 4.5 km. Units are (a) mm, (b) $\log(L^{-1})$, and (c) $\log(g/m^3)$.

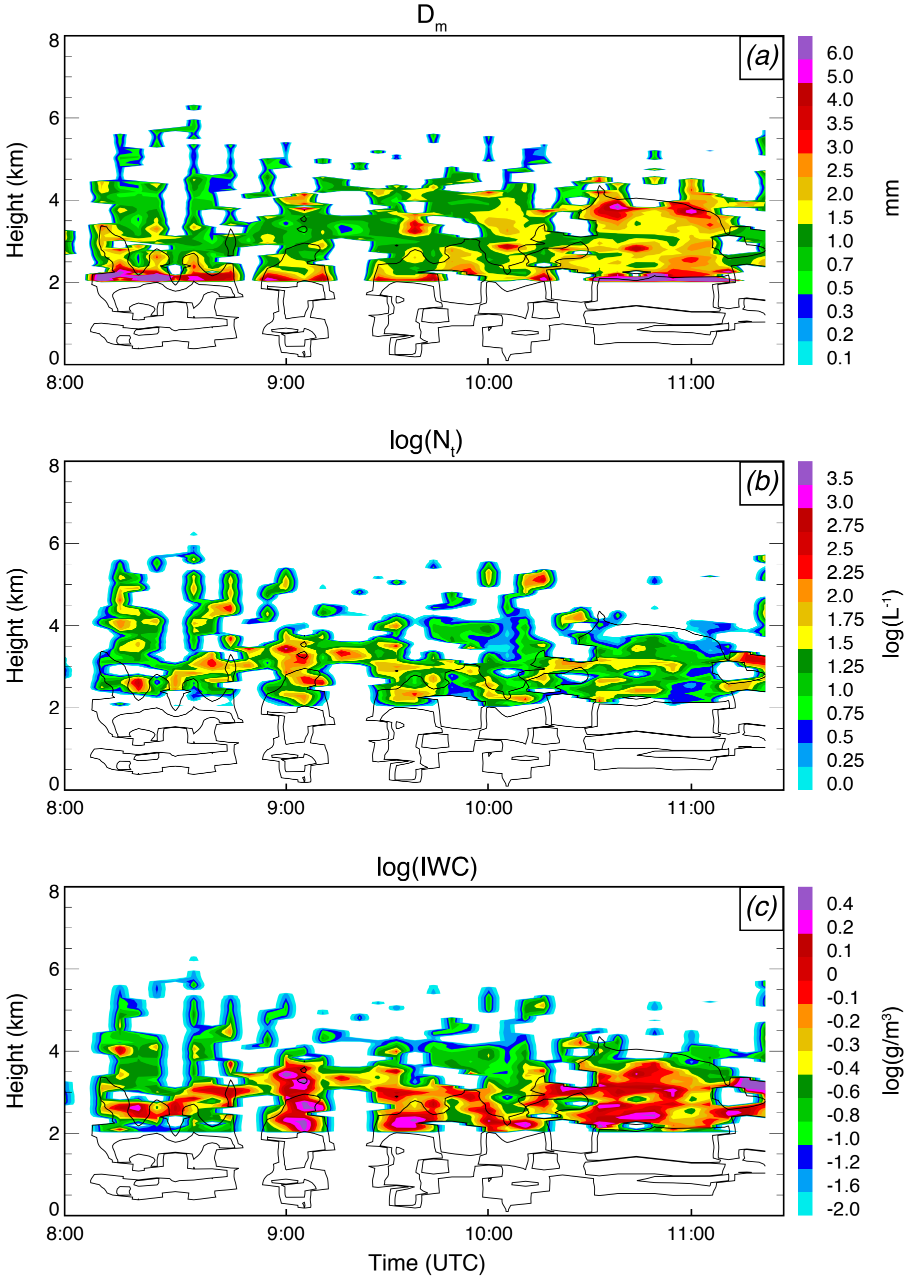

Figure 4.22: Ice microphysical retrievals performed on the April 27, 2011 moving CVP. Panels are of (a) D_m, (b) $\log(N_t)$, and (c) $\log(IWC)$. The height of the ML was subjectively determined to be 2 km. Units are (a) mm, (b) $\log(L^{-1})$, and (c) $\log(g/m^3)$.

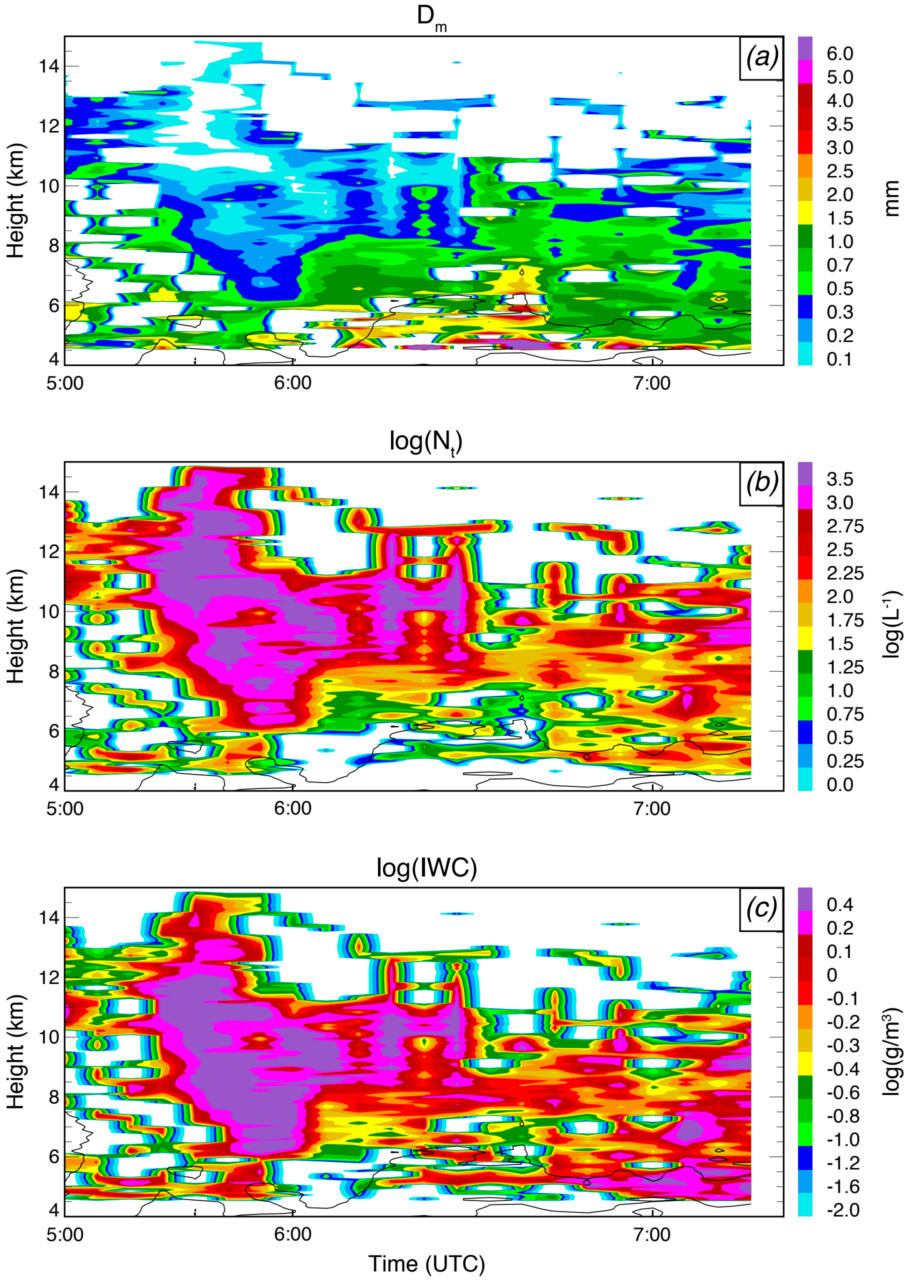

Figure 4.23: Ice microphysical retrievals performed on the July 6, 2015 moving CVP. Panels are of (a) D_m, (b) $\log(N_t)$, and (c) $\log(IWC)$. The height of the ML was subjectively determined to be 4.5 km. Units are (a) mm, (b) $\log(L^{-1})$, and (c) $\log(g/m^3)$.

27, 2011, Fig. 4.22 cannot resolve much of the vertical structure of the precipitation, even with such a low ML. Additionally, the gaps in the moving CVP make it hard to interpret not only the vertical structure of the precipitation, but also any temporal evolution as the aircraft moves in time within the evolving precipitation system.

On July 6, 2015, however, the storm was quite deep (Fig. 4.23), although gaps in the moving CVP again made it difficult to examine the microphysical structure of the storm at times, especially at the beginning of the period. Retrievals suggested a different microphysical structure than that of the May 20, 2011 MCS, estimating smaller D_m values and larger N_t and IWC values. In fact, the retrievals suggest incredibly high N_t aloft, estimating concentrations exceeding 3000 L^{-1}, and IWC values greater than 3 g/m^3. The spiral that came the closest to penetrating the region of highest N_t and IWC on Fig. 4.23 was the third spiral (Fig. 4.12), but N_t values for that spiral (not shown) peak only near 100 L^{-1}, and IWC values hover around 0.5 g/m^3. However, this spiral only reached altitudes of 6.5-7 km just before 6 UTC, whereas the region of highest N_t on Fig. 4.23 exists primarily at altitudes above 7 km, so a deep penetration of this region of incredibly high N_t and IWC retrieval values was not performed. So, it is possible that the aircraft flew only at the periphery of the maximum in N_t and IWC observed in Fig. 4.23. One explanation for such high values may be homogeneous freezing, as soundings performed by the NWS office in Aberdeen, SD at 0 and 12 UTC on July 6, 2015 show temperatures of -30 °C near 10.5 km and -40 °C near 12.3 km. Examining Fig. 4.4, the system's cloud top was near 14 km, making homogeneous freezing near cloud top possible, as homogeneous freezing of cloud drops takes place at temperatures colder than about -36 to -38 °C depending on drop size (Pruppacher and Klett, 1997).

The focus of the remainder of the study will be on the May 20, 2011 MCS, for a number of reasons. First, this was a deep precipitating system, allowing for analyses of ice microphysical properties in relatively cold regions beyond what is possible with the more shallow April 27, 2011 MC3E case. Additionally, the July 6th, 2015 flight focused on making passes through the ML (Fig. 4.12), and collected little data in temperature regions -10 °C and below, where the ice microphysical retrievals of Ryzhkov et al. (2018) are postulated to be most effective. The May 20, 2011 flight did fly at fairly cold temperatures, in and through the DGL, creating the best opportunity to analyze the effectiveness of the ice microphysical retrievals used herein.

4.6 Collocated Aircraft In Situ and Radar Microphysical Data

The technique to collocate aircraft location with CVP data was first introduced in section 2.3 as a three-dimensional collocation method in the horizontal and in time; expanded to collocate data in the vertical, therefore creating a four-dimensional collocation technique in section 3.3; and applied to ice microphysical retrievals in 3.4.2. With this technique, aircraft in situ data can now be directly compared to ice microphysical retrievals performed on CVP data, collocated to the aircraft in four dimensions. In this manner, the accuracy of equations 3.8, 3.11, and 3.12 can be tested to determine how well they are able to predict the microphysical properties of a midlatitude MCS. For these comparisons, while direct comparison of aircraft in situ measurements and ice microphysical retrievals of N_t and IWC are possible, the measure of particle size derived from the aircraft in situ measurements is D_{mm}, whereas for the ice microphysical retrievals it is D_m. While these variables are different, comparing them should still give an approximate measure of the effectiveness of the ice microphysical retrieval technique.

Figure 4.24 shows a direct comparison of aircraft in situ data to ice microphysical retrievals performed on moving CVP data. Overall the retrievals performed well, estimating the three variables within a factor of 2-3. However, there are periods of time where the retrieval algorithms struggle to accurately quantify the ice microphysical properties, such as near 15 and 16 UTC for N_t and IWC, and between 13:30

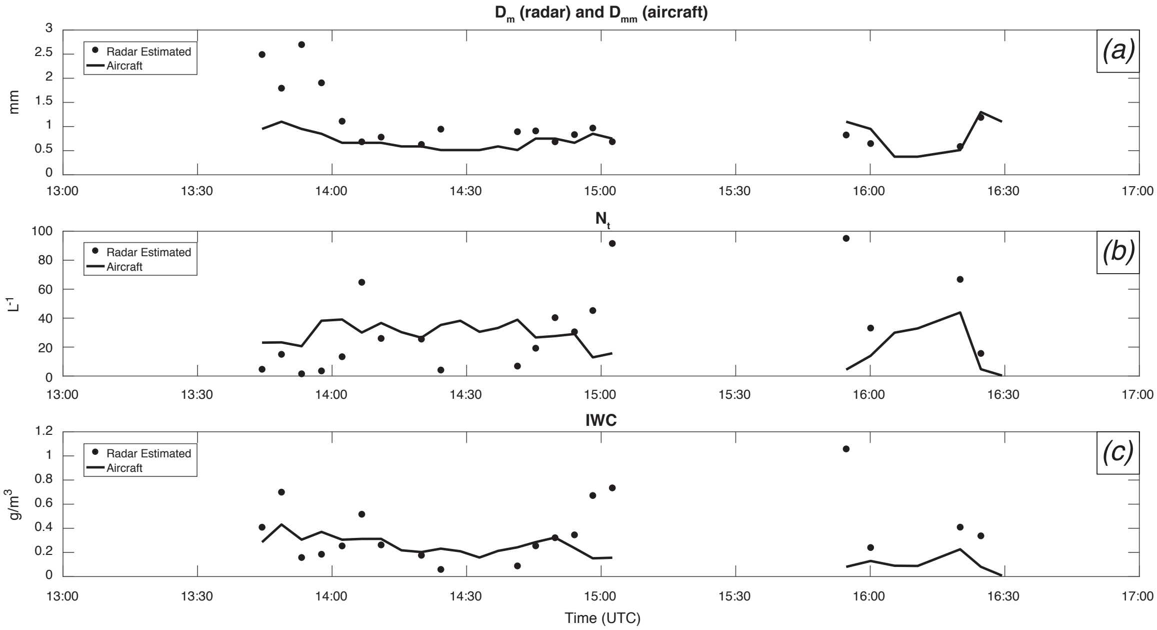

Figure 4.24: Collocated aircraft in situ data (solid line) and ice microphysical retrievals of moving CVP data (dots) collected on May 20, 2011. Panels are of (a) D_m (radar) and D_{mm} (aircraft), (b) N_t, and (c) IWC. The height of the ML was subjectively determined to be 4.5 km, and data collected below that level are not shown. Units are (a) mm, (b) L^{-1}, and (c) g/m^3.

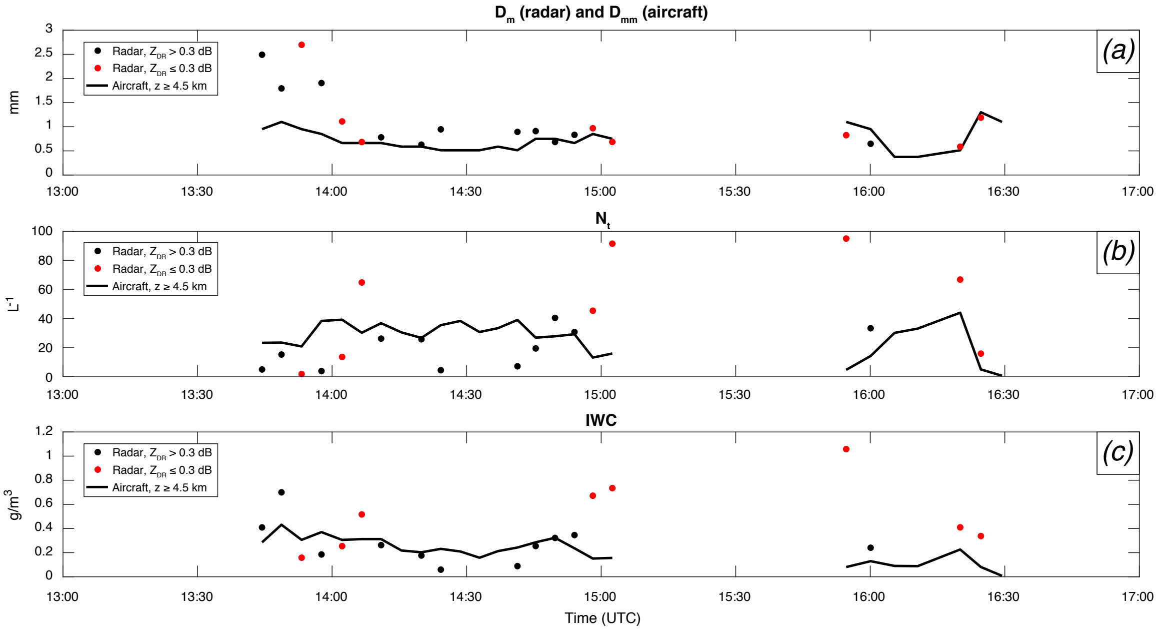

Figure 4.25: As in Fig. 4.24, but where red dots signify retrievals performed in regions where $Z_{DR} \leq 0.3$ dB.

and 14 UTC for D_m. The environments in which these aircraft in situ data and radar observations were collected vary in their polarimetric signatures, CVP distance from the radar, and distance above the ML, among other factors, and any one of these uncontrolled variables could be contributing to the errors in the microphysical estimates.

Therefore, the effects of the values of different variables must be tested to determine how the algorithm is or is not affected by high or low values of each. Low values of Z_{DR} are thought to negatively impact the algorithm's performance, since as values of Z_{DR} trend to 0, the denominator in eqn. 3.11 grows smaller, amplifying the IWC estimate. Additionally, Z_{DR} is used in calculating Z_{DP}, which is used in eqns. 3.8 and 3.12 to calculate D_m and N_t. Figure 4.25 is similar to Fig. 4.24, but points where retrievals were performed in regions of $Z_{DR} \leq 0.3$ dB are flagged as red. Low Z_{DR} values do not seem to have an appreciable effect on D_m values, but some N_t and IWC estimates with considerable error are characterized by low values of Z_{DR}. This is also

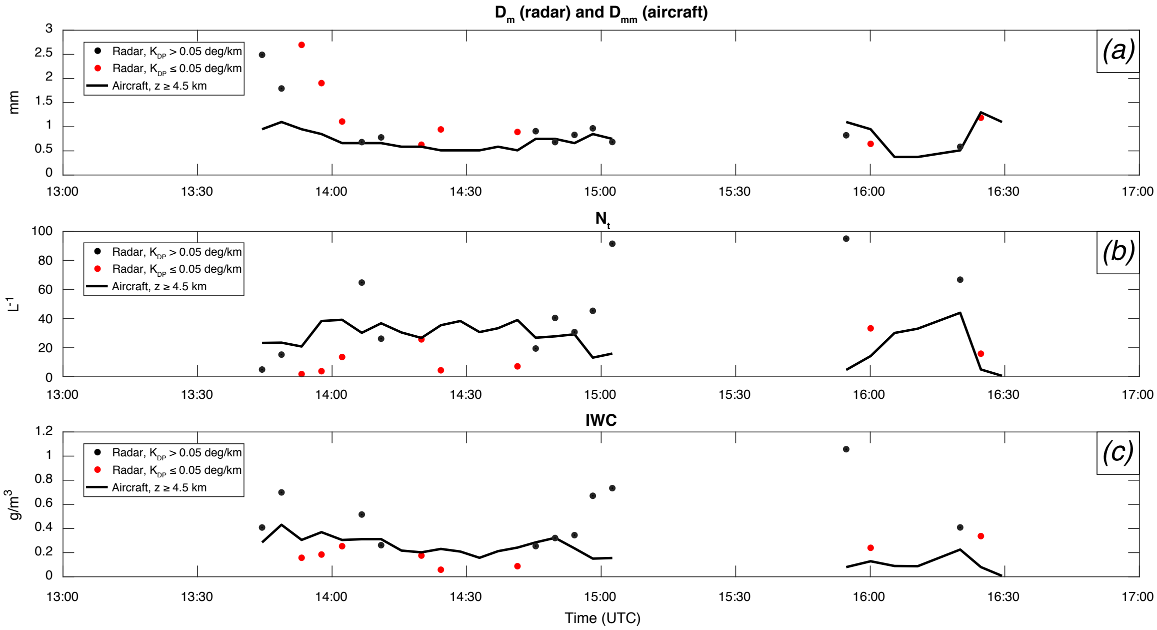

Figure 4.26: As in Fig. 4.24, but where red dots signify retrievals performed in regions where $K_{DP} \leq 0.05$ deg/km.

possibly due to a proximity to the ML, as Z_{DR} values tend to decrease towards the ML, to values near 0.2-0.25 dB.

Another polarimetric variable included in the microphysical retrievals outlined in table 3.2 is K_{DP}. Values of K_{DP} tend to drop dramatically just above the ML, and are especially small in snow for longer wavelength radars like the WSR-88Ds. Much like with Z_{DR}, as K_{DP} trends towards 0, estimates of all 3 polarimetric variables are prone to large errors. Therefore, it is feasible that ice microphysical retrievals with large errors could have been performed in regions with very low K_{DP}. Figure 4.26 is similar to Fig. 4.24, but points where retrievals were performed in regions of $K_{DP} \leq 0.05$ deg/km are flagged as red. In this case, a considerable amount of the red dots in each panel are fairly close to the in situ aircraft measurements, and many dots that stray farthest from that line are not flagged as red, except for near 14 UTC on Fig. 4.26a and a few near 14 and 14:30 UTC on Fig. 4.26b. It is important to remember, however, that for both Z_{DR} and K_{DP}, thresholds are in place to filter

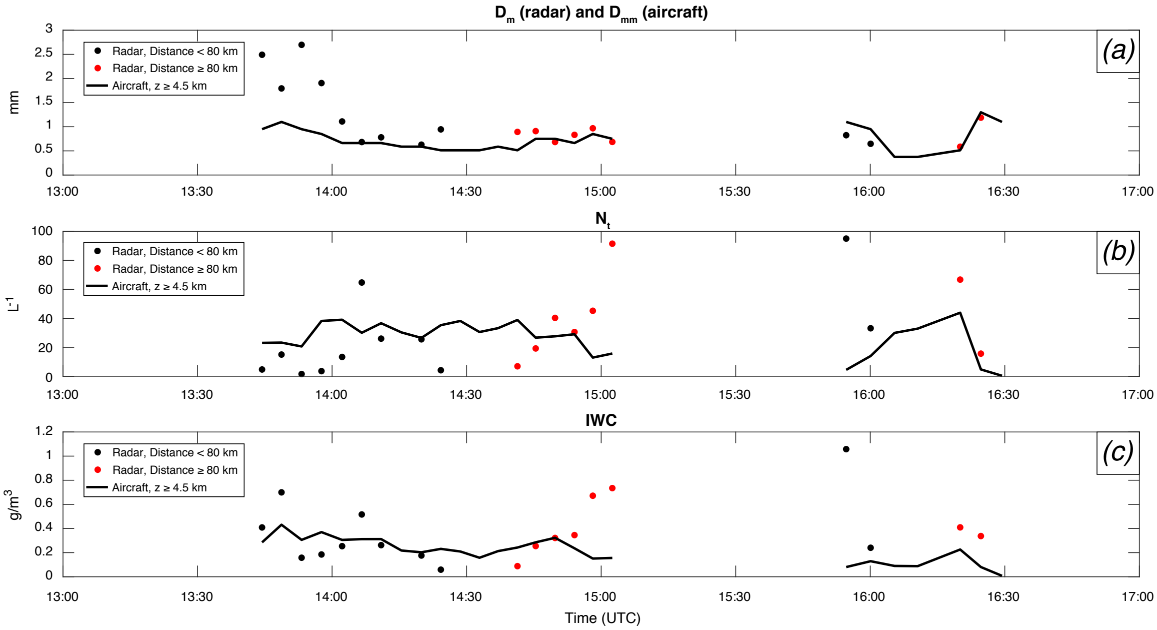

Figure 4.27: As in Fig. 4.24, but where red dots signify retrievals performed in at times when the CVP sector was centered $\geq$ 80 km from the radar.

out low confidence observations before microphysical retrievals are performed. So the conclusion is not that low values of Z_{DR} do not negatively affect D_m estimates, or that low values of K_{DP} are not strongly correlated to errors in microphysical retrievals. Rather, it is that the thresholds on how large these polarimetric values must be to be ingested into the algorithm may need further tuning, to improve estimates of D_m in regions of low Z_{DR}, and slightly improve estimates overall in regions of low K_{DP}.

Of additional concern is the effect the distance the CVP sector is from the radar can have on the estimates. As distance from the radar increases, the size of the CVP sector increases in the azimuthal direction. This increase in sector size could potentially smooth out finescale features that would have been resolved if the aircraft was closer in radial distance from the radar. So, an investigation of the dependance of algorithm accuracy to CVP sector distance from the radar is warranted. Figure 4.27 is again similar to Fig. 4.24, but points where retrievals were performed at distances $\geq$ 80 km are flagged as red. Examining all three subplots, it seems that

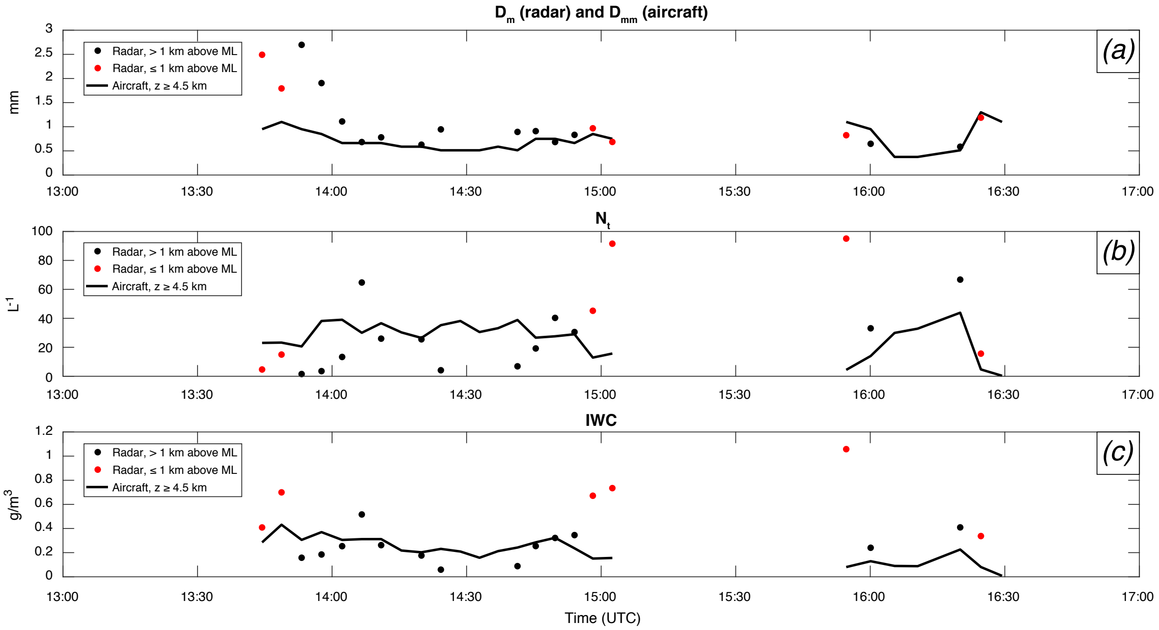

Figure 4.28: As in Fig. 4.24, but where red dots signify retrievals performed in regions where the aircraft was flying $\leq$ 1 km above the ML.

CVP distance from the radar does not have a considerable effect of the retrieval technique's accuracy, especially for D_m, where some of the most accurate retrievals happened when the CVP was $\geq$ 80 km from the radar. This statement holds for all times except near 15 UTC for N_t and IWC, as was also seen in Fig. 4.25b-c, where the aircraft was also flying in regions of low Z_{DR}. However, as was previously mentioned, this error may be related more to the aircraft's distance above the ML.

As stated when discussing the effect of low Z_{DR} values and large CVP distance from the radar on the algorithm's estimates, proximity to the ML can also be a predictor of poor estimates, as polarimetric variables decrease toward the ML due to aggregation. Figure 4.28 highlights points where retrievals were performed as the aircraft flew $\leq$ 1 km above the ML. Many of the points with considerable error are flagged as red, meaning that the algorithm struggled to accurately quantify the microphysical properties of the precipitaiton in regions near the ML. Ryzhkov et al.

(2018) address this, stating “the method is expected to be more accurate at relatively low temperatures (say, lower than -10 to -15 °C).”

4.7 Analysis of Particle Imagery

Particle images, taken by the 2D-C and HVPS probes on May 20, 2011, were analyzed to determine the relative concentrations of isotropic and anisotropic particles within the system. During this flight, the moving CVP does not show any enhancement in Z_{DR} above the ML in the region of the DGL (Fig. 2.7), which according to in situ temperature measurements existed between approximately 6 and 7.5 km. As mentioned by Griffin et al. (2018), strong Z_{DR} signatures may be absent in the DGL for two distinct reasons. First, such signatures may be absent if the volume sampled by the radar remains dominated by small, quasi-isometric ice hydrometeors falling into the DGL from aloft, masking the Z_{DR} signature from the less abundant dendrites. Second, dendrites may not exist within the DGL, eliminating the potential for such a strong Z_{DR} signature.

Particle images taken with the 2D-C and HVPS probes are shown in Figs. 4.29 and 4.30. These images are from the entire duration of the flight, and each panel shows imagery taken during the second at which the temperature sampled was closest to the temperature listed to the left of the panel, which increases downward in 1 °C increments from -20 to -10 °C. Across all panels of particle imagery for temperatures from -20 to -10 °C, the 2D-C imagery in Fig. 4.29 show very few dendrites, and sampling volumes are consistently dominated by quasi spherical ice. McFarquhar et al. (2007) examined particle imagery just below the DGL and above the ML for the downward portion of 2 spirals executed during an MCS event sampled by the P-3 aircraft during BAMEX. They found that in this region (at temperatures equal to and warmer than -10 °C, different from the DGL as is investigated here), ice was also primarily quasi spherical, and no evidence of dendrites at the coldest temperatures

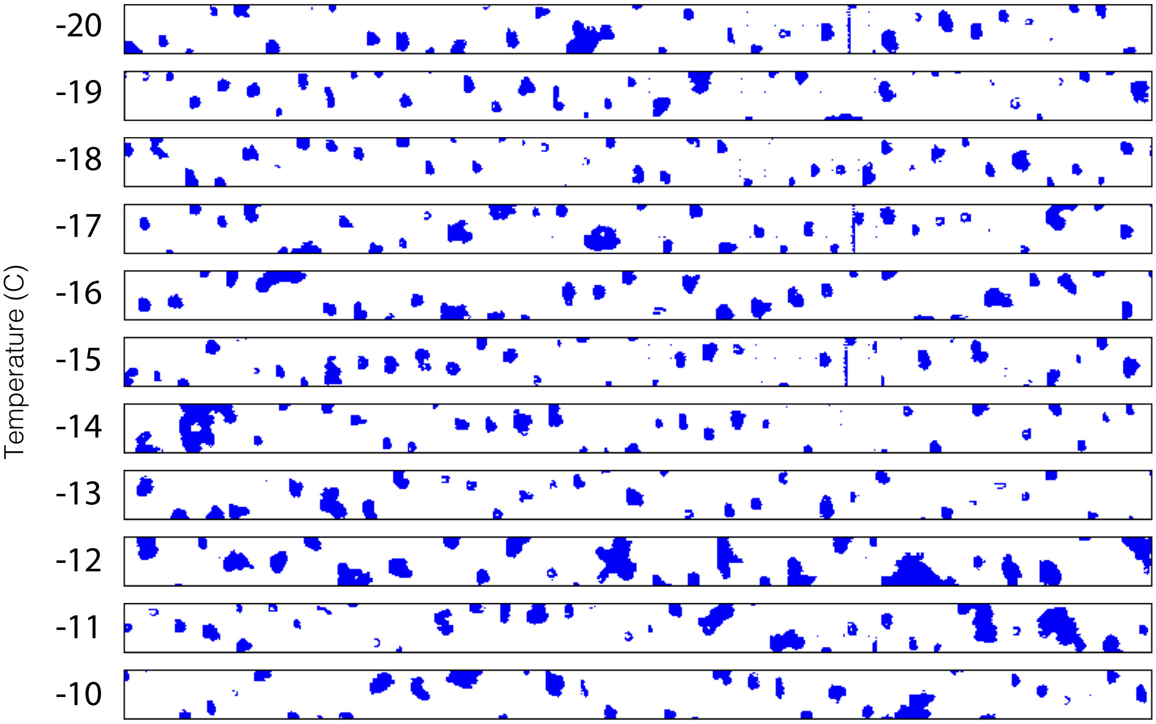

Figure 4.29: Particle imagery from the 2D-C probe, with panels of images taken at temperatures from -20 to -10 °C, in increments of 1 °C, increasing downward. Panels show data collected during the second at which the sampled temperature was closest to the noted temperature. Buffer width is 960 microns, and resolution is 30 microns.

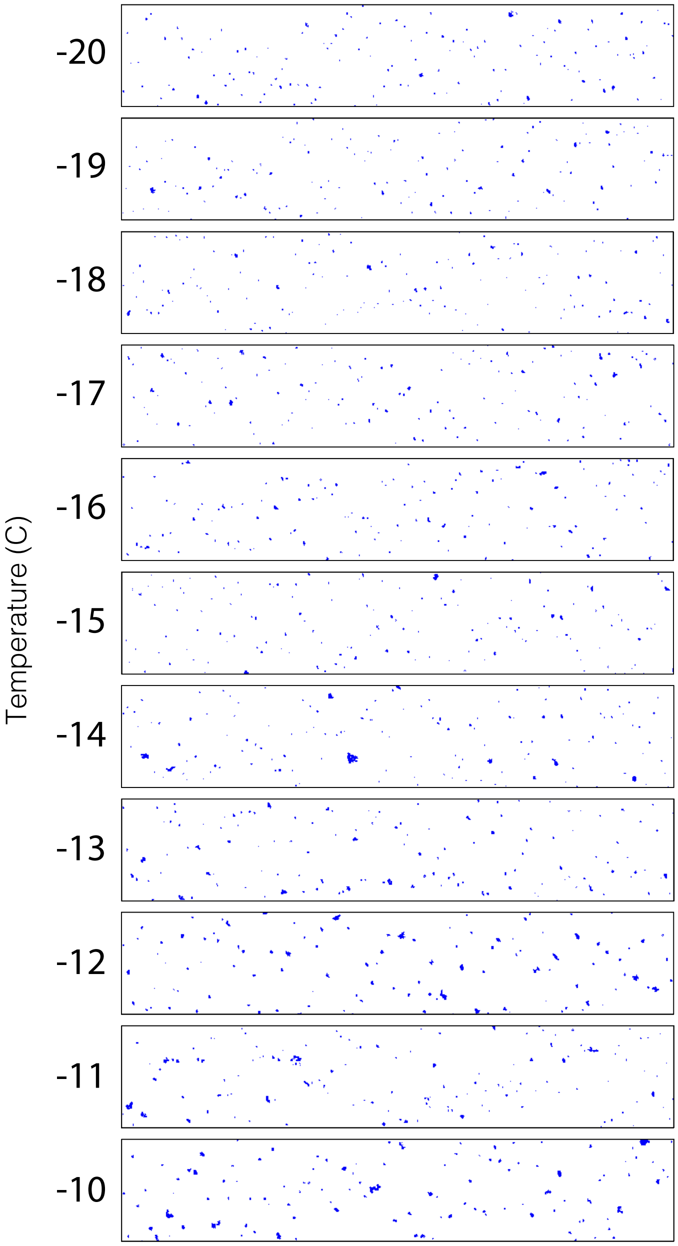

Figure 4.30: Particle imagery from the HVPS probe, with panels of images taken at temperatures from -20 to -10 °C, in increments of 1 °C, increasing downward. Panels show data collected during the second at which the sampled temperature was closest to the noted temperature. Buffer width is 19200 microns, and resolution is 150 microns.

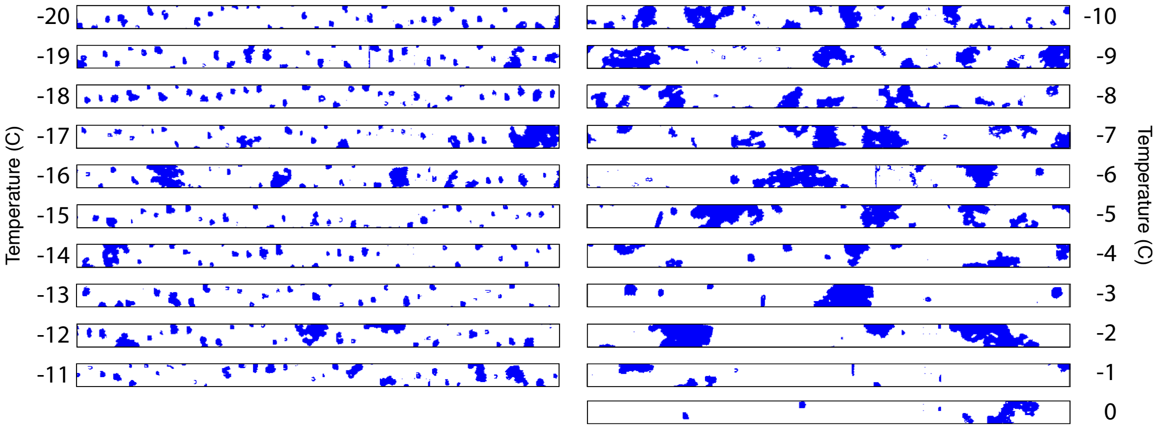

Figure 4.31: Particle imagery from the 2D-C probe, with panels of images taken at temperatures from -20 to 0 °C, in increments of 1 °C. Panels show data collected during the downward portion of the spiral performed at the end of the flight, with each individual panel showing particle imagery taken during the second at which the sampled temperature was closest to the noted temperature. Buffer width is 960 microns, and resolution is 30 microns.

shown was present. Although more difficult to see with the HVPS probe in Fig. 4.30, again, almost all of the ice sampled is quasi spherical, with little to no evidence of dendritic growth. The finding that particles within the DGL of this storm are primarily quasi spherical and few if any dendrites are present supports the lack of Z_{DR} signature in cold regions penetrated by the aircraft (Fig. 2.7).

Additionally, particle imagery from May 20, 2011 can be used to validate hypotheses about particle morphology and evolution throughout the downward spiral performed on that day, as examined in section 4.4. Figs. 4.31 and 4.32 show particle imagery from the downward portion of the spiral performed at the end of the flight, as was analyzed via box and whisker plots in Figs. 4.13 and 4.14. From the latter two figures, it was hypothesized that aggregation was not a dominant process until the aircraft sampled regions with temperatures greater than -10 °C, and that potential sublimation of small particles was occuring concurrently with aggregation.

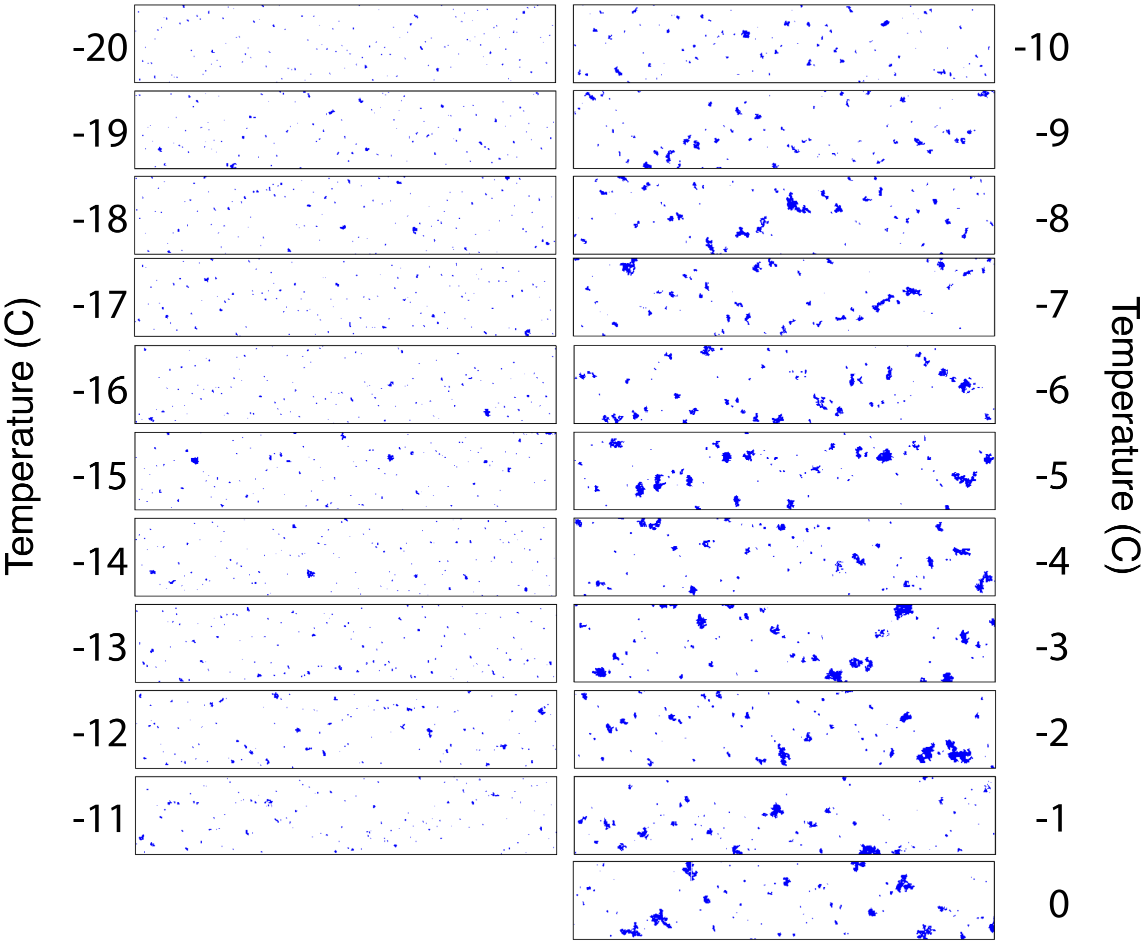

Figure 4.32: Particle imagery from the HVPS probe, with panels of images taken at temperatures from -20 to 0 °C, in increments of 1 °C. Panels show data collected during the downward portion of the spiral performed at the end of the flight, with each individual panel showing particle imagery taken during the second at which the sampled temperature was closest to the noted temperature. Buffer width is 19200 microns, and resolution is 150 microns.

Examining Figs. 4.31 and 4.32, both show a marked increase in average particle size at temperatures greater than -10 °C when compared to temperatures less than -10 °C, confirming that aggregation became a dominant process at these temperatures. Smaller particles are also much less numerous in particle imagery at warmer temperatures, which could be solely due to the collection of such particles during the aggregation process, but also could be due to sublimation of small particles.

4.8 Comparison of Midlatitude and Tropical MCS Stratiform Microphysical Structure

The final investigation into the vertical structure of MCSs as it pertains to microphysical quantities and polarimetric radar data involves a comparison of midlatitude and tropical MCS stratiform regions. Currently, the ice microphysical retrieval technique described in section 3.4 has been applied only to midlatitude MCSs and a handful of landfalling tropical cyclones (Ryzhkov et al., 2018). The analyses of MCS stratiform regions in section 4.5 can be expanded to analyze a climatology of archetypal MCSs observed over the contiguous United States, and compare QVPs and microphysical retrievals from those cases to QVPs and retrievals of data collected within tropical MCS stratiform. Analyzing the differences between polarimetric variables and ice microphysical retrieval outputs from midlatitude and tropical MCSs will offer insight into how the microphysical structures of these systems may differ.

A number of archetypal MCSs observed by the WSR-88D radar network during 2017 comprise a small climatology herein, and were chosen for their robust stratiform regions and close proximity to a WSR-88D radar site. MCSs with well defined leading convective lines, transition zones, and trailing stratiform regions were sampled by KBMX in Birmingham, AL on April 3 from 12-18 UTC; by KLSX in St. Louis, MO on April 29-30 from 19-3 UTC; and by KEAX in Kansas City, MO on October 22 from 4-10 UTC. QVPs of the MCSs sampled on these days and by these radars are

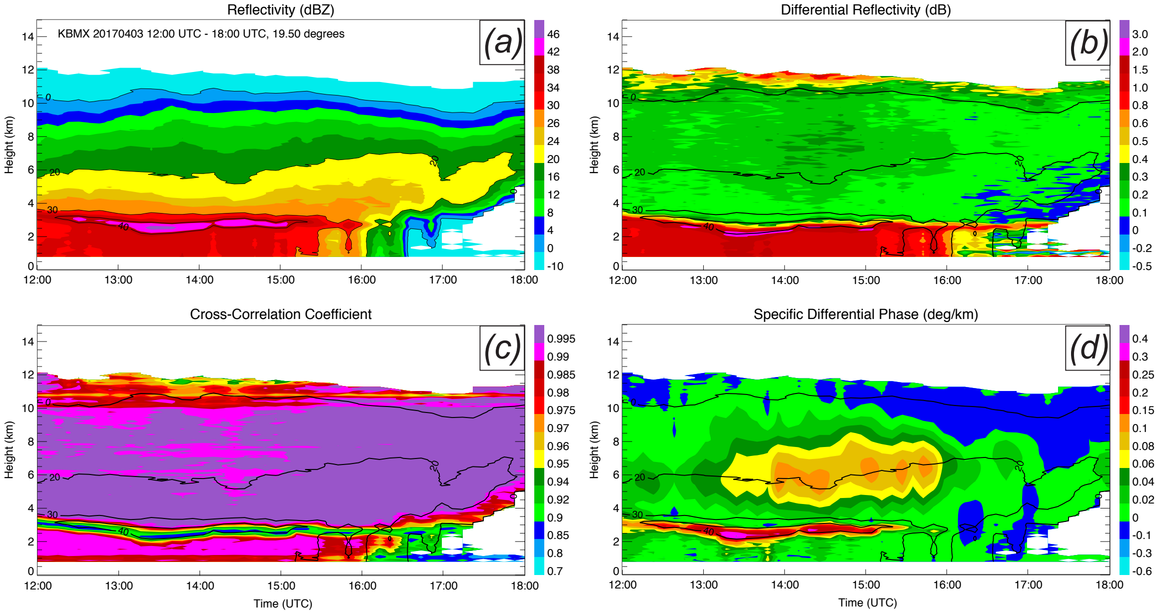

Figure 4.33: QVP of (a) Z, (b) Z_{DR}, (c) ρ_{hv}, and (d) K_{DP} from 12-18 UTC on April 3, 2017, using data from the KBMX radar.

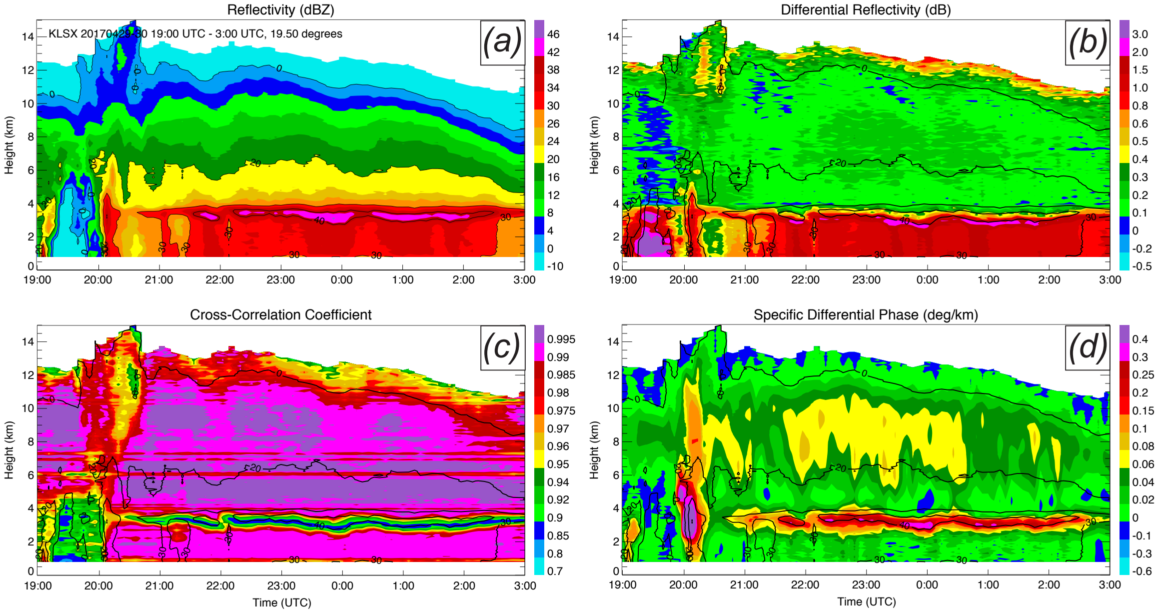

Figure 4.34: QVP of (a) Z, (b) Z_{DR}, (c) ρ_{hv}, and (d) K_{DP} from 19-3 UTC on April 29-30, 2017, using data from the KLSX radar.

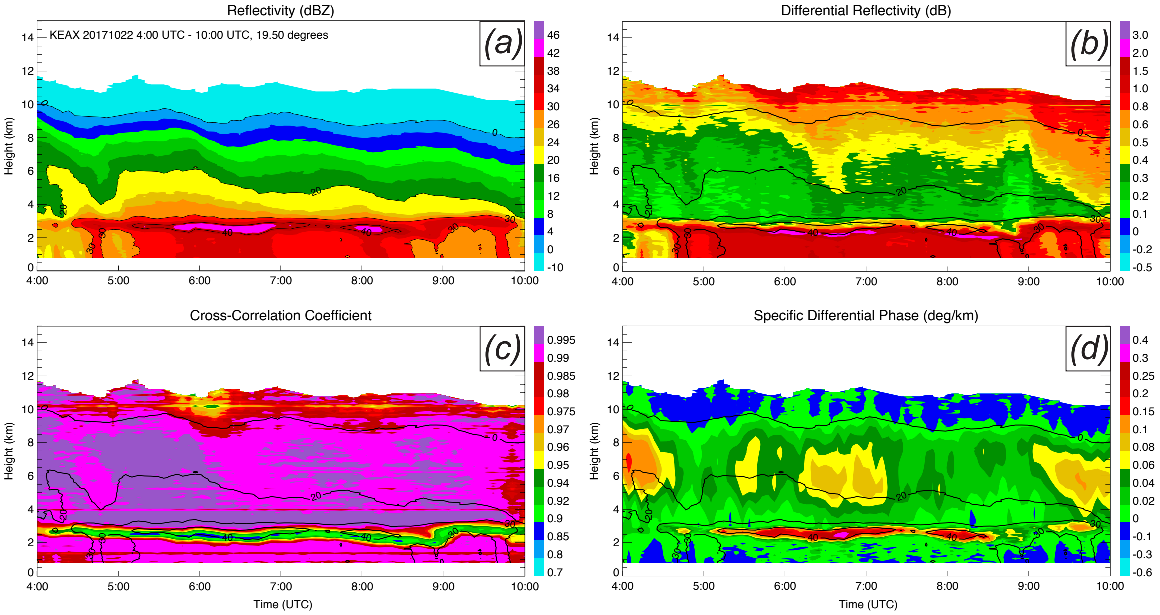

Figure 4.35: QVP of (a) Z, (b) Z_{DR}, (c) ρ_{hv}, and (d) K_{DP} from 4-10 UTC on October 22, 2017, using data from the KEAX radar.

seen in Figs. 4.33-4.35. In all 3 of these QVPs, clear ML signatures in all 4 panels are visible, and the QVPs themselves are visually quite smooth (except for the beginning of Fig. 4.34), indicating that the QVPs are not heavily contaminated by convection.

Tropical MCSs were observed by S-band radar during the Dynamics of the MJO (DYNAMO; Yoneyama et al., 2013) campaign over the Indian Ocean. DYNAMO was executed as a part of the Cooperative Indian Ocean Experiment on Intraseasonal Variability in the Year 2011 (CINDY2011) to study the Madden-Julian Oscillation (MJO) and its influence on convective initiation in the tropics. The S-PolKa radar, an advanced dual-polarimetric, dual-wavelength (10 cm for S-band, 0.8 cm for Ka-band) radar (Lutz et al., 1995; UCAR/NCAR-Earth Observing Laboratory, 1996, 2012), was operating during this campaign. On October 24, 2011, robust stratiform was sampled by the radar during the first half of the day, presenting an opportunity to do a QVP analysis of tropical stratiform sampled by an S-band radar, as shown in

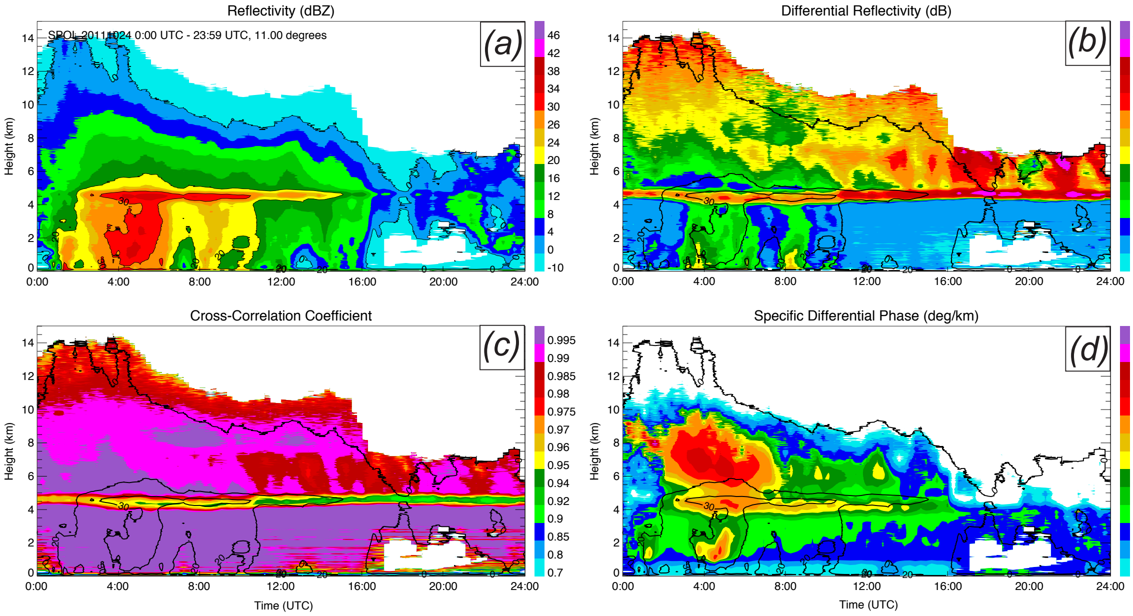

Figure 4.36: QVP of (a) Z, (b) Z_{DR}, (c) ρ_{hv}, and (d) K_{DP} from 0-23:59 UTC on October 24, 2011, using data from the S-PolKa radar.

Fig. 4.36. These panels also show a strong ML signature, with the best QVP data quality in the beginning of the period.

A number of MCSs were also been sampled over Darwin, Australia with the C-POL radar (Keenan et al., 1998). Established as a part of the Tropical Rainfall Measuring Mission (TRMM) to provide information on tropical rainfall, it operates October through May annually and provides one volume scan of C-band (5 cm wavelength) radar data every 10 minutes. Therefore, QVPs of tropical rainfall can also be made using this data. MCS stratiform was sampled by C-POL on February 15, 2011 and February 18, 2014, persisting for the entire day and primarily during the latter half of the day for each case, respectively. Figures 4.37 and 4.38 show QVPs created using that radar data. Again, the QVPs of C-POL data show a fairly smooth profile of each polarimetric variable through the entire day for Fig. 4.37 and the latter half of the day for Fig. 4.38, and distinct ML signatures in 3 of the 4 panels, excluding K_{DP}. Of note are the obvious issues with K_{DP} near the surface/below the ML in Fig. 4.38,

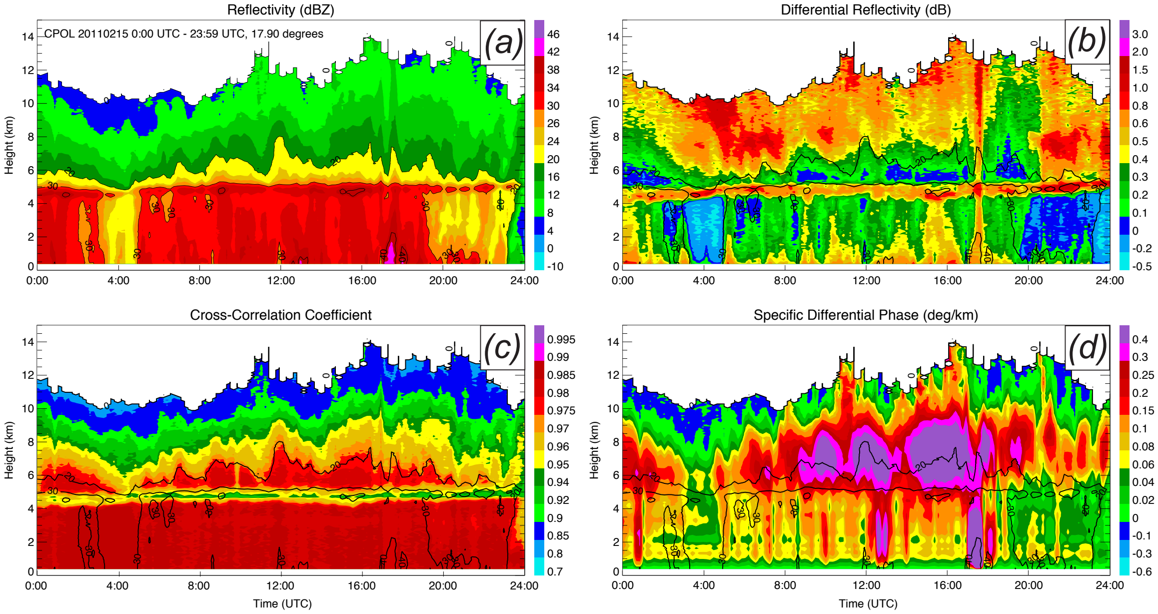

Figure 4.37: QVP of (a) Z, (b) Z_{DR}, (c) ρ_{hv}, and (d) K_{DP} from 0-23:59 UTC on February 15, 2011, using data from the C-POL radar.

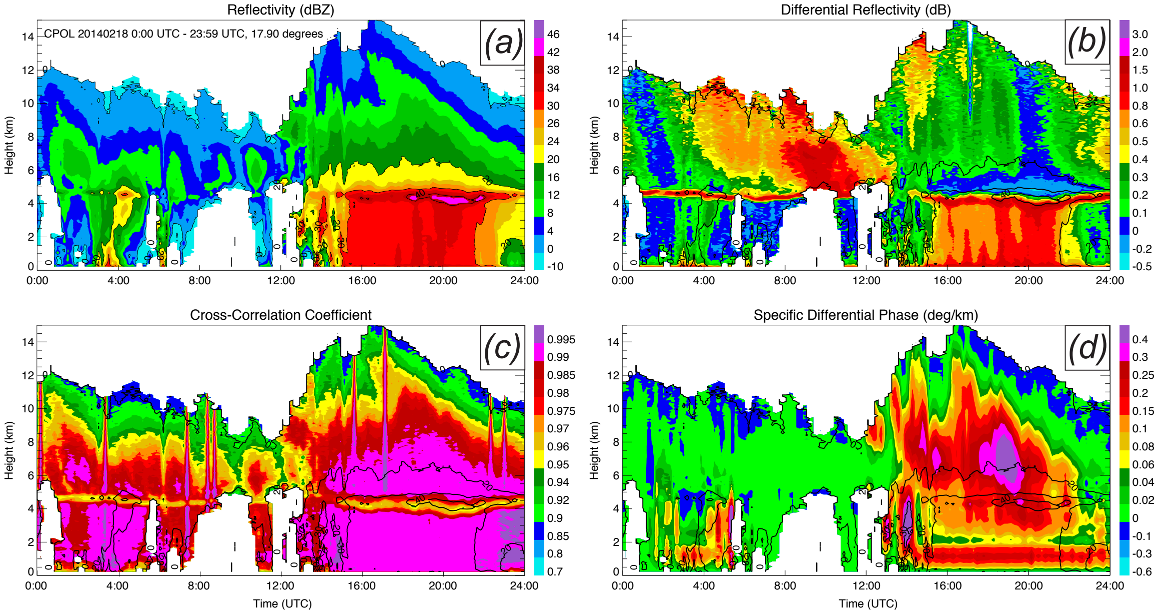

Figure 4.38: QVP of (a) Z, (b) Z_{DR}, (c) ρ_{hv}, and (d) K_{DP} from 0-23:59 UTC on February 18, 2014, using data from the C-POL radar.

from approximately 0.5-2 km. Additionally, it is slightly concerning that in Figs. 4.37 and 4.38, there is no clear K_{DP} maximum within the ML as are seen in Figs. 4.33-4.36. Instead, for the C-POL QVPs, enhanced K_{DP} extends from midlevels to into the ML, whereas in the midlatitude cases and for S-PolKa, this is not observed. Therefore, future work using this QVP data should investigate potential sources of error or artifacts that may persist in the C-POL data, particularly in K_{DP} and Φ_{DP}. However, data above the ML appear to be of good quality in all 4 panels for both C-POL cases, and since the focus herein will be on the ice microphysical properties of these midlatitude and tropical systems, despite the issues with K_{DP} near the surface and an absence of a K_{DP} maximum in the ML, the data from these cases will still be used.

To determine any potential differences in microphysical structure between midlatitude and tropical MCSs, microphysical retrievals were performed on the 6 aforementioned cases, for direct comparison of the vertical structures of D_m, N_t, and IWC. Instead of creating figures displaying the 3 retrieved variables for each individual case, Figs. 4.39-4.41 show the retrievals of D_m, N_t, and IWC, respectively, for all 6 of the cases, organized into columns of midlatitude and tropical cases.

In Fig. 4.39, there appears to be a clear signature of aggregation in the retrievals performed on midlatitude systems, with a marked increase of D_m from cloud top toward the ML. Such a strong signature is absent, however, in the tropical retrievals. D_m for those cases is much more constant in magnitude with depth in the cloud. Apparently, aggregation of ice in tropical clouds is not a dominant process, in contrast with midlatitudes, for the cases shown herein. Comparing the relative magnitudes of midlatitude and tropical D_m, the average value for tropical is lower than that for midlatitude, except near cloud top.

In retrievals of N_t (Fig. 4.40), the concentrations of ice in the tropical clouds generally exceed those in the midlatitude clouds by an order of magnitude. The only

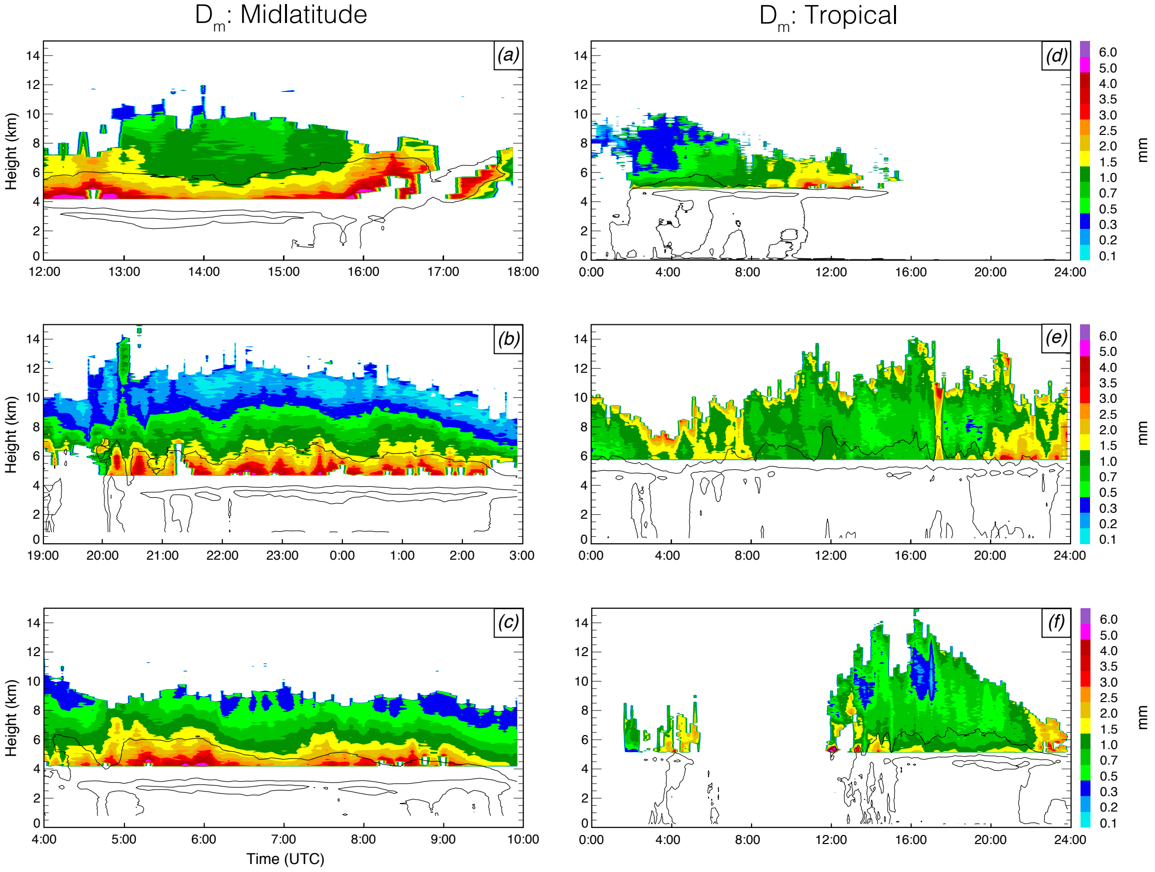

Figure 4.39: Ice microphysical retrievals of D_m performed on (a-c) midlatitude and (d-f) tropical MCSs, calculated from Figs. 4.33-4.38, shown in numeric-to-alphabetical order. The height of the ML was subjectively determined for each case, and units are in mm.

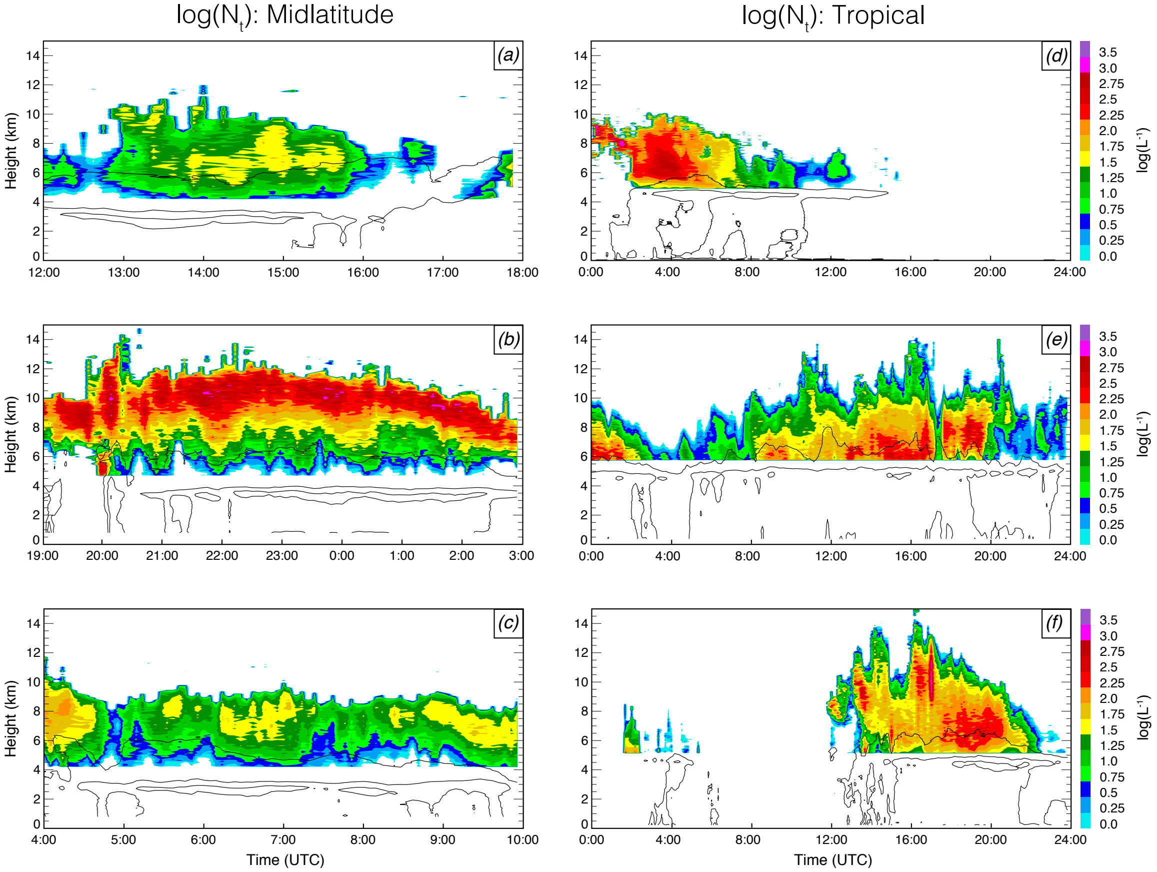

Figure 4.40: Ice microphysical retrievals of $\log(N_t)$ performed on (a-c) midlatitude and (d-f) tropical MCSs, calculated from Figs. 4.33-4.38, shown in numeric-to-alphabetical order. The height of the ML was subjectively determined for each case, and units are in $\log(L^{-1})$.

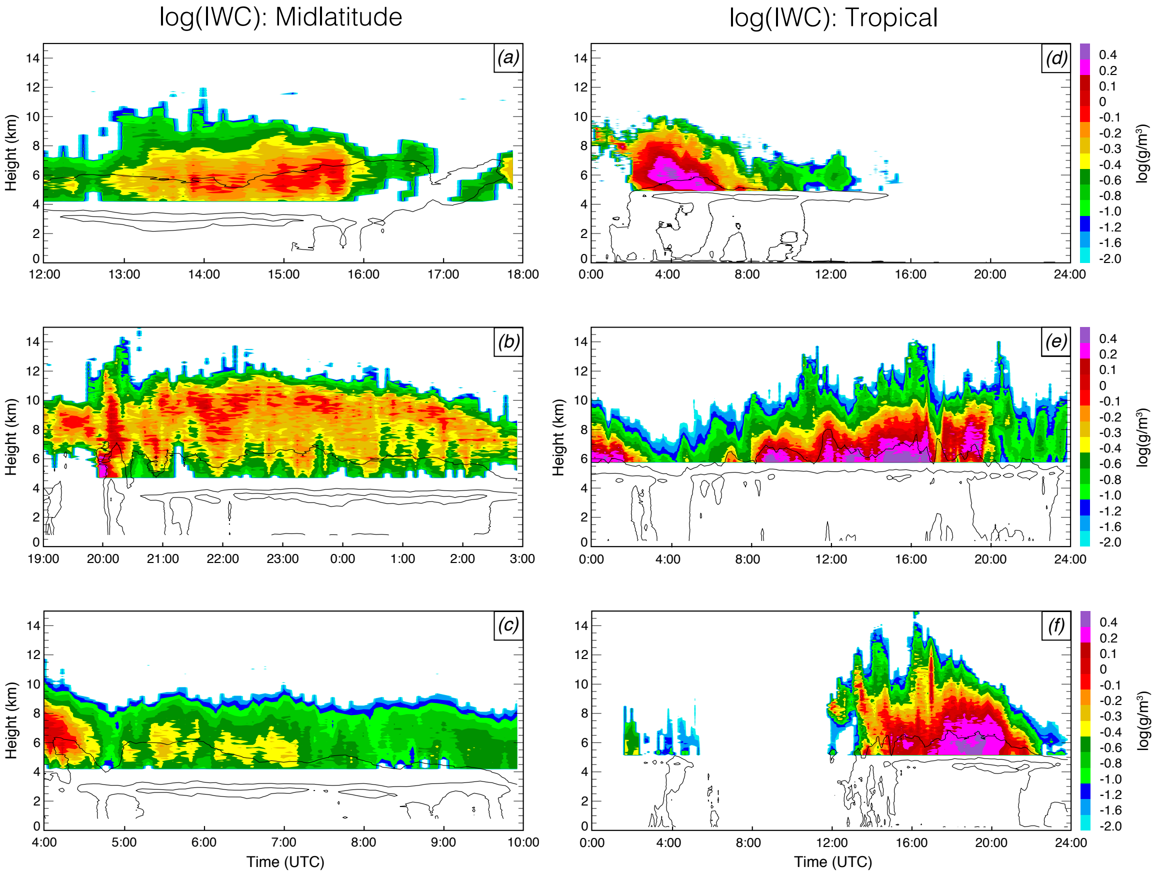

Figure 4.41: Ice microphysical retrievals of IWC performed on (a-c) midlatitude and (d-f) tropical MCSs, calculated from Figs. 4.33-4.38, shown in numeric-to-alphabetical order. The height of the ML was subjectively determined for each case, and units are in $\log(g/m^3)$.

exception is with Fig. 4.40b, which is the N_t retrieval from the April 29-30, 2017 case sampled by KLSX. Magnitudes of N_t for this case match and sometimes even exceed the concentrations seen in the tropical cases. In the midlatitude cases, it appears that N_t is maximized near cloud top or just below, and decreases toward the ML. This is not the case in the tropical cases, where N_t appears to increase steadily towards the ML.

A similar pattern is seen in retrievals of IWC (Fig. 4.41). Values of IWC in midlatitude clouds are less than those in tropical clouds by a factor of 2-3 on average. In tropical clouds, IWC values exceed 3 g/m^3, whereas in midlatitude, values rarely exceed 1 g/m^3. Values of IWC in the midlatitude cases are maximized in the midlevels, and stay fairly constant, decreasing somewhat towards the ML, whereas in the tropical cases, peak values of IWC are found right above the ML, with a steady increase in IWC through the depth of the cloud above the ML.

Analyzing the conclusions drawn for each microphysical variable for both midlatitude and tropical cases, it is evident that while there are magnitude differences for each variable between the retrievals performed in midlatitude and tropical MCSs, the most important story may be in the vertical gradients of these variables. The vertical gradients of D_m, $\log(N_t)$, and $\log(IWC)$ were calculated for the April 29-30, 2017 KLSX (Fig. 4.42) and February 15, 2011 C-POL (Fig. 4.43) QVPs, to analyze the vertical gradients of the 3 microphysical variables for one midlatitude and one tropical case. To calculate these gradients, first, the retrievals were smoothed vertically using a five-point running mean, performed if there were data in at least 3 of the 5 points in the five-point window. The vertical gradient was then calculated for each point using a central difference method, meaning that the gradient was calculated as half of the difference between the points directly above and below the point of interest. The vertical data spacing in each QVP is approximately 80 m, and an increase downward is defined as positive, so these gradients are in units of $[-\Delta[variableunits]/(80m)]$.

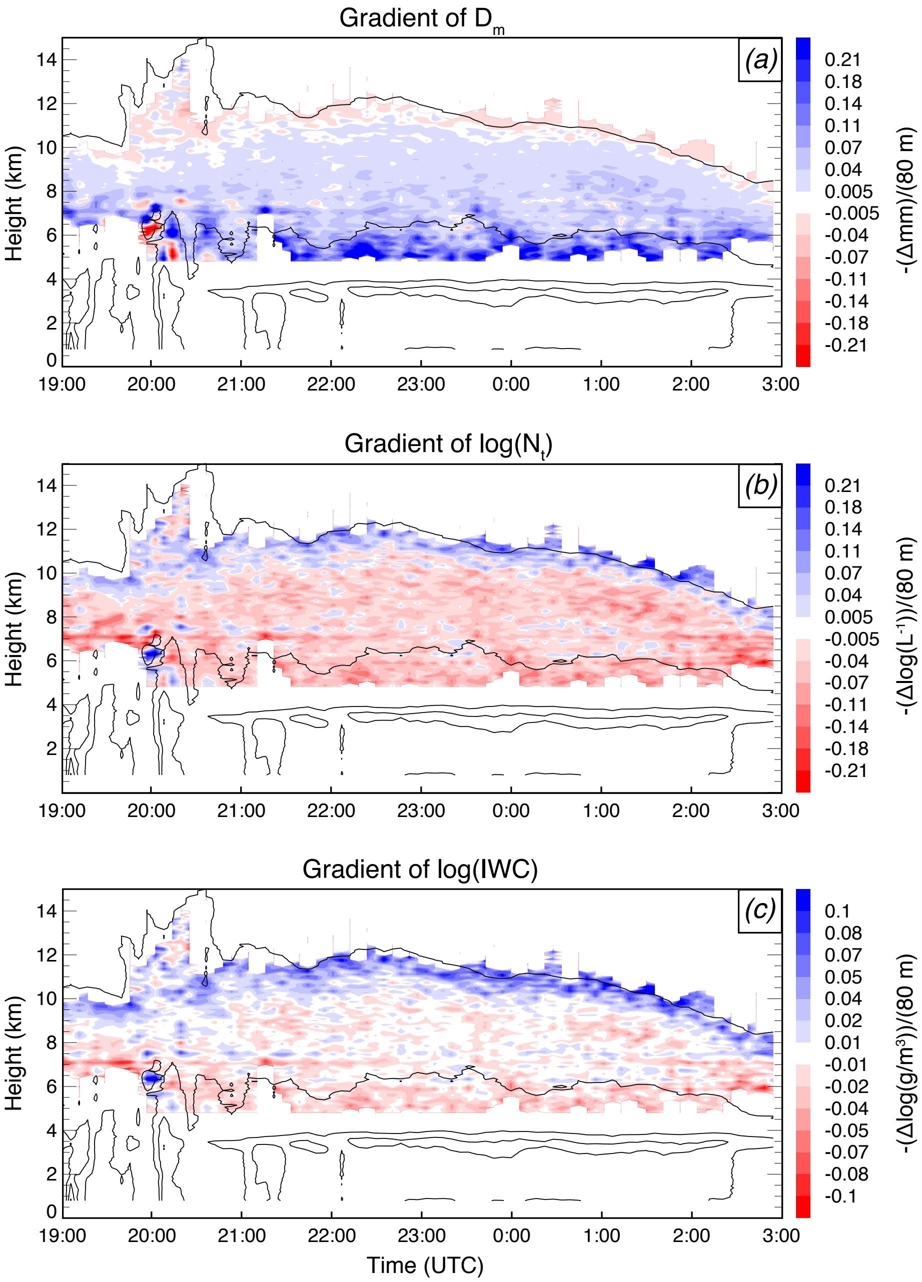

Figure 4.42: Vertical gradients of (a) D_m, (b) $\log(N_t)$, and (c) $\log(IWC)$ for the KLSX QVP shown in Fig. 4.34 using retrieval data for that case shown in Figs. 4.39-4.41. Blue denotes a downward increase, and red denotes a downward decrease in each variable.

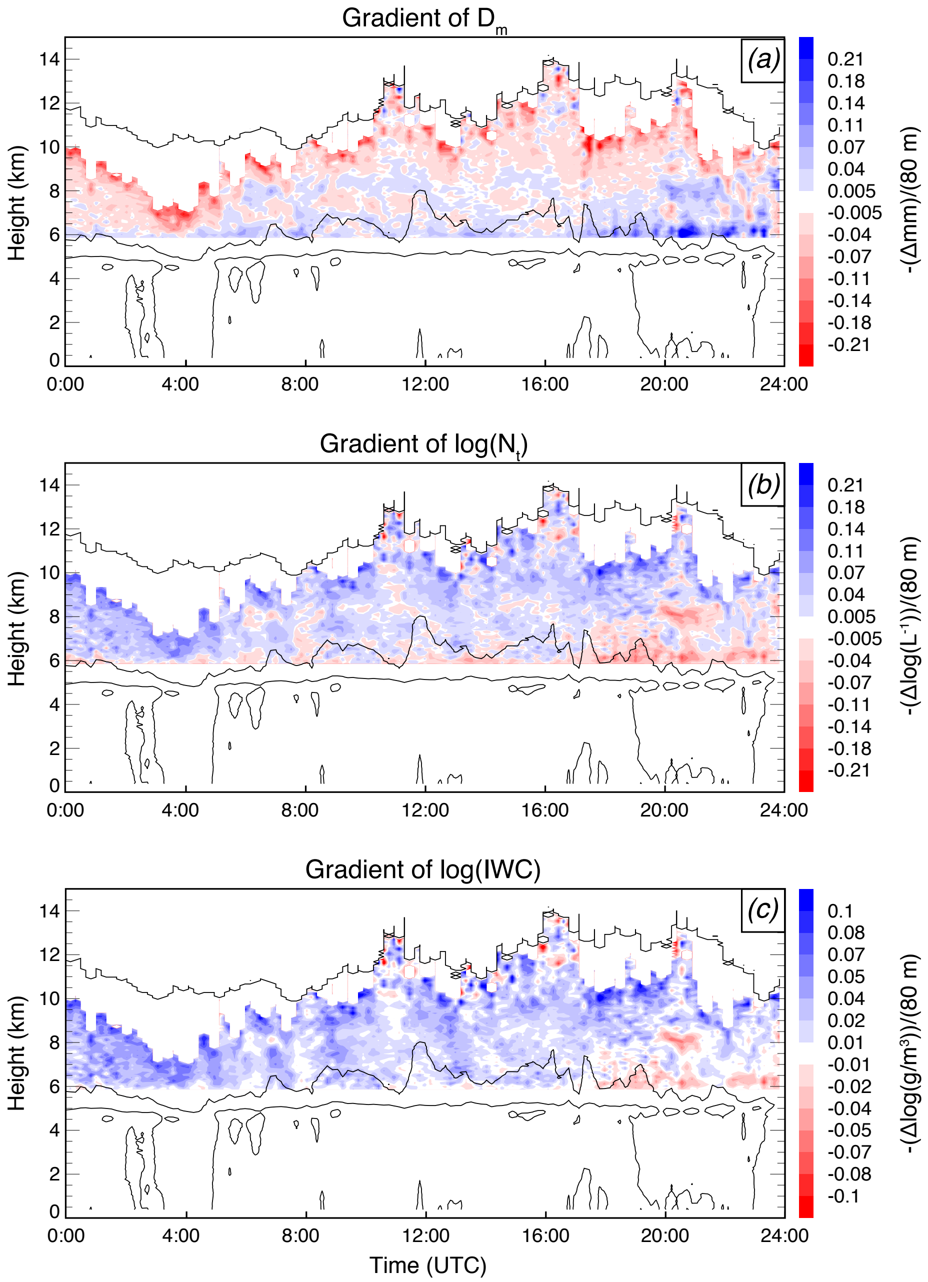

Figure 4.43: Vertical gradients of (a) D_m, (b) $\log(N_t)$, and (c) $\log(IWC)$ for the C-POL QVP shown in Fig. 4.37 using retrieval data for that case shown in Figs. 4.39-4.41. Blue denotes a downward increase, and red denotes a downward decrease in each variable.

Note that the difference between a $\log(N_t)$ value of 2.1 and 2.0 is the same as the difference between 0.6 and 0.5, so when N_t is represented in log space, it appears as if the same change in concentration is occuring between points of 2.0 and 2.1 $\log(L^{-1})$ and points of 0.5 and 0.6 $\log(L^{-1})$, when in linear space, this translates to changes of 25 and 0.8 L^{-1}, respectively. For that reason, analyses of these figures should focus on qualitative conclusions and not on quantitative changes in magnitude (particularly of $\log(N_t)$ and $\log(IWC)$ values). If a quantitative understanding of these figures is desired, analyses of these gradients should be paired with the microphysical retrievals for each case to be able to understand the gradients in terms of the actual magnitudes of N_t and IWC. Gradients are to be trusted most in regions far from cloud top and/or the ML, as the microphysical retrievals work best far from the ML, and polarimetric radar data can sometimes be spurious near cloud top.

In the midlatitude case (Fig. 4.42), D_m increases through the entire vertical profile of the storm above the ML, with the increase strongest at lower altitudes. Physically, this suggests aggregation of smaller particles aloft, where D_m increases only a small amount from the aggregation of small particles. Lower in the cloud, where particles are larger and radar sample volumes have a higher concentrations of aggregates, the aggregation of these already sizeable aggregates produces a large average increase of D_m. This is corroborated with the profile of N_t in Fig. 4.42. Except right at cloud top, where the gradient of $\log(N_t)$ is positive likely due to particle nucleation, the gradient of $\log(N_t)$ is negative through the entire depth of the cloud. This suggests that particles are aggregating through the entire depth of the cloud, pairing well with what is seen in the vertical profile of the D_m gradient. When the gradient of N_t in linear space is calculated (not shown), the gradient of N_t is highly negative in the upper levels of the cloud, increasing to near zero by 8 km and remaining near zero from 8 km to the ML. This also corroborates the hypothesis that small particles are aggregating aloft and large particles are aggregating near the ML, since a much larger number of particles exist at the onset of aggregation, such that aggregation of these particles greatly decreases the concentration with depth, and progressively less particles exist as aggregation persists, such that aggregation of these particles decreases the concentration only slightly. By using the gradient of $\log(N_t)$ instead of N_t, small decreases in regions of lower N_t are much more visible. Finally, the vertical gradient of IWC is slightly negative through the depth of the cloud except right at cloud top, but overall is very close to zero. This qualitatively agrees with the concept that particles are falling and aggregating through the depth of the cloud, and no new ice mass is being added via particle nucleation or depositional growth. The slight decrease in IWC could be due to particles falling faster as they aggregate and grow in size and mass, contributing to the visible decrease in $\log(N_t)$ with depth, or sublimation of small particles, also contributing to decreasing $\log(N_t)$ and increasing D_m.

In the tropical case (Fig. 4.43), gradients of D_m are weak, with values remaining nearly consistent with depth. From this alone, it appears that aggregation of ice in tropical clouds is not a dominant process, in contrast with midlatitudes. A different story than what was told with the midlatitude case is told mainly by the profiles of $\log(N_t)$ and $\log(IWC)$. Both of these profiles show a steady increase through the depth of the cloud. Physically, this suggests an upward shift of the particle PSD, with mean size of the particles in each sample volume remaining nearly the same, but the number concentration across the PSD increasing, producing an increase in IWC. This may suggest that in tropical clouds, nucleation of particles is not limited to the upper levels of the cloud, but rather occurs through the depth of the cloud and in the absence of aggregation. In addition, ice multiplication due to shattering of freezing cloud drops may be another reason for the increase of N_t and IWC towards the freezing level in tropical systems (Khain and Pinsky, 2018).

In continuing analyses, this comparison of three MCSs from each environment will need to be expanded to include more cases from both environments. This development of a large climatology of cases will allow for more broad conclusions about their respective microphysical structures, and the ability to corroborate the initial conclusions drawn herein. A larger sample size will ensure that these conclusions hold up when considering the majority of MCSs in each environment, and that the three chosen for each environment herein were not anomalies. Furthermore, this fundamental difference in microphysical processes in midlatitude versus tropical MCSs requires further investigation beyond microphysical retrievals, including similar point-by-point comparison as was done in section 4.6 for tropical MCSs, to ensure that the retrievals are appropriately characterizing the structure of tropical MCSs and that what is seen in Fig. 4.43 is mirrored in in situ data.

Chapter 5

Future Work

The CVP methodology is still in its infancy, and as a result, there is a lot of future work that can be done with CVPs, ice microphysical retrievals, and the various applications shown herein. A number of those are outlined below, with the caveat that this list is non-exhaustive, and will only grow as the CVP and ice microphysical retrieval techniques are more widely used and embraced by the community.

1) The CVP technique was tested herein on only MCSs, and no published literature exists examining the technique when applied to different precipitation types and structures. Some analyses using CVPs to examine hurricanes/tropical cyclones and the precipitation substructures within them are ongoing with scientists at NSSL and the Cooperative Institute for Mesoscale Meteorological Studies (CIMMS), but as the technique itself is not yet published, the opportunity hasn't presented itself to the broader community to examine other precipitaiton structures with CVPs. While it can be expected that the CVP technique will appropriately resolve the vertical structure of whatever precipitation it is used to analyze, further analyses of other precipitation types are needed to confirm that, and will likely happen with time and a broader awareness of this technique in the community.

2) As mentioned in sections 4.3 and 4.8, the QVP technique can sometimes struggle when ingesting weather radar data not collected by S-band radars or radars within the WSR-88D radar network. The main challenge seems to be appropriately calculating K_{DP}, with additional challenges seen in the NOXP data in section 4.3 relating to low SNR and low Z_{DR} above the ML. While some of the issues in the X-band data can likely be resolved with rigorous attenuation correction, since these issues only presented themselves in QVPs of C- and X-band radar data, the processing codes

must be examined and optimized to create high quality QVPs using data from radars of various wavelengths, and not just S-band. Additionally, creating QVPs using radar data not collected by the WSR-88D network is fairly labor intensive, since the algorithm was optimized to ingest and examine data stored in the specific format of data available through the National Centers for Environmental Information (NCEI), and creating CVPs with data of other formats is not currently possible. Further modification of the codes to ingest a wide array of data types is needed, and like with further exploration of the CVP technique's efficacy in examining different precipitation structures, will likely come as the community continues and begins to embrace the QVP and CVP techniques, respectively.

3) Different specifications within the CVP code must be tested more rigorously than they were here. Variations in the vertical data spacing and Cressman radius of influence were discussed in section 4.1, but many more degrees of freedom exist when creating the CVP, including the sector size. Although cursory examination of sector size has been done for a few individual cases (not shown), a more rigorous test of sector size must be done to determine whether or not 20 km by 20° is the optimum sector size for CVPs. Also, investigations into the vertical data spacing and Cressman radius of influence in section 4.1 were strictly qualitative, and discussed how the CVP image differed when these specifications were changed. Quantitative analyses must be performed, including performing ice microphysical retrievals on CVPs with these varying specifications, to determine how changing these specifications affects the actual values of the polarimetric variables and the microphysical data retrieved from them.

4) Finally, in situ data for tropical MCSs must be examined to determine whether or not the microphysical retrievals performed on these storms are accurate and the retrieval codes applicable to these storms. Due to how different the microphysical structures and processes appear to be between midlatitude and tropical MCSs from

analyses of these retrievals, in situ data are imperative to determine whether or not such stark differences are truly present. Such in situ validation of the algorithms' effectiveness in tropical environments is a natural next step towards determining the universal applicability of these ice microphysical retrieval equations.

Chapter 6

Conclusions

This study examined how operational weather radar data could be better used to understand the vertical structure of precipitation on an even finer scale than what is possible using QVPs. It also capitalized on the belief that there exists a rich opportunity to use in situ microphysical measurements to validate ice microphysical retrieval algorithms optimized for S-band operational weather radar data. Together, these pursuits offered an opportunity to gain a deeper understanding of the microphysical structure of MCSs. Therefore, the goal of this study was to utilize operational polarimetric radar data and polarimetric ice microphysical retrieval algorithms in conjunction with in situ aircraft data to gain a deeper understanding of the ice microphysical structure of MCSs, and determine the usefulness and effectiveness of such new ice microphysical retrieval algorithms and radar data processing techniques. A number of conclusions can be drawn from the work herein:

1) The CVP methodology has emerged as a novel way to visualize operational polarimetric radar data collected by S-band WSR-88D weather radars. This technique is most appropriate when the CVP sector is centered at a distance less than 110 km from the radar, and can be altered such that the CVP center moves in time. Compared to the GridRad technique, CVPs offer greater vertical resolution, which is important for analyzing finescale polarimetric signatures in precipitation.

2) Newly developed ice microphysical retrieval techniques using polarimetric radar data show promise in quantitatively estimating D_m, N_t, and IWC within midlatitude MCSs. Such algorithms work best in regions of high Z_{DR} and high K_{DP}, such as in the DGL. Thresholds can and have been applied to eliminate low values of these variables, but may need to be adjusted in the future. It was shown that, of the

values above the set thresholds, low values of Z_{DR} may negatively affect N_t and IWC estimates, whereas low K_{DP} values had no strong correlation to errors in any of the three microphysical variables. This may indicate a need to tune the Z_{DR} thresholds for the retrieval algorithms. CVP sector distance from the radar had no visible effect on D_m estimates and only occasional negative impact on N_t and IWC, with no clear correlation between distance and poor estimates. The factor that seemed to negatively affect estimates the most was proximity to the ML. A distance of ≤ 1 km above the ML was related to worse estimates of all 3 microphysical variables, confirming that the algorithm works best in regions far above the ML, as stated in Ryzhkov et al. (2018).

3) QVPs of archetypal MCSs from both midlatitude and tropical environments were examined, and ice microphysical retrievals were performed on those QVPs. Two distinct microphysical structures were observed, with potentially quite different microphysical processes. In midlatitude MCSs, an increase of D_m and decrease of N_t with depth, with a nearly constant IWC, suggest aggregation through the depth of the cloud. In tropical MCSs, nearly constant D_m paired with increasing N_t and IWC with depth suggest nucleation of new hydrometeors and an overall absence of aggregation. Further studies into the microphysical structure and processes of tropical MCSs, including in situ measurements and an expanded climatology, are needed to confirm these initial conclusions.

Bibliography

Andric, J., M. R. Kumjian, D. S. Zrnic, J. M. Straka, and V. M. Melnikov, 2013: Polarimetric Signatures above the Melting Layer in Winter Storms: An Observational and Modeling Study . *J. Appl. Meteor. Climatol.*, **52**, 682–700.

Atlas, D., S. Matrosov, A. Heymsfield, M. Chou, and D. Wolf, 1995: Radar and Radiation Properties of Ice Clouds. *J. Appl. Meteor.*, **34**, 2329–2345.

Austin, P. M., and A. C. Bemis, 1950: A Quantitative Study of the "Bright Band" in Radar Precipitation Echoes. *J. Operational Meteor*, **7**, 145–151.

Aydin, K., and C. Tang, 1997: Relationships between IWC and Polarimetric Radar Measurands at 94 and 220 GHz for Hexagonal Columns and Plates. *J. Atmos. Oceanic Technol.*, **14**, 1055–1063.

Bailey, M. P., and J. Hallett, 2009: A Comprehensive Habit Diagram for Atmospheric Ice Crystals: Confirmation from the Laboratory, AIRS II, and Other Field Studies. *J. Atmos. Sci.*, **66**, 2888–2899.

Baker, B. A., and R. P. Lawson, 2006: *Improvement in determination of ice water content from two-dimensional particle imagery: Part I: Image to mass relationships*, Vol. 45. 1282–1290 pp.

Balakrishnan, N., and D. S. Zrnic, 1990a: Estimation of Rain and Hail Rates in Mixed-Phase Precipitation. *J. Atmos. Sci.*, **47**, 565–583.

Balakrishnan, N., and D. S. Zrnic, 1990b: Use of Polarization to Characterize Precipitation and Discriminate Large Hail. *J. Atmos. Sci.*, **47**, 1525–1540.

Biggerstaff, M. I., and Coauthors, 2015: The Shared Mobile Atmospheric Research and Teaching Radar: A Collaboration to Enhance Research and Teaching. *Bull. Amer. Meteor. Soc.*, **86**, 1263–1274.

Bowman, K. P., and C. R. Homeyer, 2017: GridRad - Three-Dimensional Gridded NEXRAD WSR-88D Radar Data. Research Data Archive at the National Center for Atmospheric Research, Computational and Information Systems Laboratory, Boulder, CO. [Available online at https://doi.org/10.5065/D6NK3CR7.].

Bringi, V. N., and V. Chandrasekar, 2001: *Polarimetric Doppler Weather Radar: Principles and Applications.* Cambridge University Press, 636 pp.

Bukovcic, P., A. Ryzhkov, D. Zrnic, and G. Zhang, 2018: Polarimetric Radar Relations for Quantification of Snow Based on Disdrometer Data. *J. Appl. Meteor. Climatol.*, **57**, 103–120.

Bukovcic, P., D. Zrnic, and G. Zhang, 2017: Winter Precipitation Liquid-Ice Phase Transitions Revealed with Polarimetric Radar and 2DVD Observations in Central Oklahoma. *J. Appl. Meteor. Climatol.*, **56**, 1345–1363.

Carey, L. D., and W. A. Petersen, 2015: Sensitivity of C-Band Polarimetric Radar-Based Drop Size Estimates to Maximum Diameter. *J. Appl. Meteor. Climatol.*, **54**, 1352–1371.

Carlin, J. T., A. V. Ryzhkov, J. C. Snyder, and A. Khain, 2016: Hydrometeor Mixing Ratio Retrivals for Storm-Scale Radar Data Assimilation: Utility of Current Relations and Potential Benefits of Polarimetry. *Mon. Wea. Rev.*, **144**, 2981–3001.

Cazenave, F., M. Gosset, M. Kacou, M. Alcoba, E. Fontaine, C. Duroure, and B. Dolan, 2016: Characterization of Hydrometeors in Sahelian Convective Systems with an X-Band Radar and Comparison with In Situ Measurements. Part I: Sensitivity of Polarimetric Radar Particle Identification Retrieval and Case Study Evaluation. *J. Appl. Meteor. Climatol.*, **55**, 231–249.

Cooney, J. W., K. P. Bowman, C. R. Homeyer, and T. M. Fenske, 2018: Ten-year analysis of tropopause-overshooting convection using GridRad data. *J. Geophys. Res.*, **123**, 329–343.

Cressman, G. P., 1959: An Operational Objective Analysis System. *Mon. Wea. Rev.*, **87**, 367–374.

Crum, T. D., and R. D. Alberty, 1993: The WSR-88D and the WSR-88D Operational Support Facility. *Bull. Amer. Meteor. Soc.*, **74**, 1669–1688.

Davis, C., and Coauthors, 2004: The Bow Echo and MCV Experiment: Observations and Opportunities. *Bull. Amer. Meteor. Soc.*, **85**, 1075–1093.

Delanoe, J., A. Heymsfield, A. Protat, A. Bansemer, and R. Hogan, 2014: Normalized particle distribution for remote sensing application. *J. Geophys. Res. Atmos.*, **119**, 4204–4227.

Doviak, R. J., V. Bringi, A. Ryzhkov, A. Zahrai, and D. Zrnic, 2000: Considerations for Polarimetric Upgrades to Operational WSR-88D Radars. *J. Atmos. Oceanic Technol.*, **17**, 257–278.

Doviak, R. J., and D. S. Zrnic, 2006: *Doppler Radar and Weather Observations*. Dover, second edition.

Elmore, K. L., 2011: The NSSL Hydrometeor Classification Algorithm in Winter Surface Precipitation: Evaluation and Future Development. *Wea. Forecasting*, **26**, 756–765.

Fan, J., and Coauthors, 2015: Improving representation of convective transport for scale-aware parameterization: 1. Convection and cloud properties simulated with spectral bin and bulk microphysics. *J. Geophys. Res. Atmos.*, **120**, 3485–3509.

Finlon, J. A., G. M. McFarquhar, R. M. Rauber, D. M. Plummer, B. F. Jewett, D. Leon, and K. R. Knupp, 2016: A Comparison of X-Band Polarization Parameters with In Situ Microphysical Measurements in the Comma Head of Two Winter Cyclones. *J. Appl. Meteor. Climatol.*, **55**, 2549–2574.

Fridlind, A., A. Ackerman, A. Grandin, F. Dezitter, M. Weber, J. Strapp, A. Korolev, and C. Williams, 2015: High ice water content at low radar reflectivity near deep convection – Part 1: Consistency of in situ and remote-sensing observations with stratiform rain column simulations. *Atmos. Chem. Phys.*, **15**, 11 713–11 728.

Fridlind, A. M., and Coauthors, 2017: Derivation of aerosol profiles for MC3E convection studies and use in simulations of the 20 May squall line case. *Atmos. Chem. Phys.*, **17**, 5947–5972.

Fujita, T., 1955: Results of Detailed Synoptic Studies of Squall Lines. *Tellus*, **7**, 405–436.

Geerts, B., and Coauthors, 2017: The 2015 Plains Elevated Convection At Night Field Project. *Bull. Amer. Meteor. Soc.*, **98**, 767–786.

Giangrande, S. E., and A. V. Ryzhkov, 2008: Estimation of Rainfall Based on the Results of Polarimetric Echo Classification. *J. Appl. Meteor. Climatol.*, **47**, 2445–2462.

Griffin, E. M., T. J. Schuur, and A. V. Ryzhkov, 2018: A Polarimetric Analysis of Ice Microphysical Processes in Snow, using Quasi-Vertical Profiles. *J. Appl. Meteor. Climatol.*, **57**, 31–50.

Hamilton, R. A., and J. W. Archbold, 1945: Meteorology of Nigeria and adjacent territory. *Quart. J. Roy. Meteor. Soc.*, **71**, 231–262.

Heinselman, P. L., and A. V. Ryzhkov, 2006: Validation of Polarimetric Hail Detection. *Wea. Forecasting*, **21**, 839–850.

Heymsfield, A., S. Matrosov, and N. Wood, 2016: Toward improving ice water content and snow-rate retrievals from radars. Part I: X and W bands, emphasizing *CloudSat*. *J. Appl. Meteor. Climatol.*, **55**, 2063–2090.

Heymsfield, A., Z. Wang, and S. Matrosov, 2005: Improved radar ice water content retrieval algorithms using coincident microphysical and radar measurements. *J. Appl. Meteor.*, **44**, 1391–1412.

Heymsfield, A. J., A. Bansemer, M. R. Poellot, and N. Wood, 2015: Observations of Ice Microphysics through the Melting Layer. *J. Atmos. Sci.*, **72**, 2902–2928.

Hogan, R., M. Mittermaier, and A. Illingworth, 2006: The retrievals of ice water content from radar reflectivity factor and temperature and its use in evaluating a mesoscale model. *J. Appl. Meteor. Climatol.*, **45**, 301–317.

Hogan, R. J., L. Tian, P. R. A. Brown, C. D. Westbrook, A. J. Heymsfield, and J. D. Eastment, 2012: Radar Scattering from Ice Aggregates Using the Horizontally Aligned Oblate Spheroid Approximation. *J. Appl. Meteor. Climatol.*, **51**, 655–671.

Homeyer, C. R., 2014: Formation of the enhanced-V infrared cloud top feature from high-resolution three-dimensional radar observations. *J. Atmos. Sci.*, **71**, 332–348.

Homeyer, C. R., and M. R. Kumjian, 2015: Microphysical characteristics of overshooting convection from polarimetric radar observations. *J. Atmos. Sci.*, **72**, 870–891.

Houze, R. A., 2004: Mesoscale Convective Systems. *Rev. Geophys.*, **42**, 43 pp.

Houze, R. A., 2018: 100 Years of Research on Mesoscale Convective Systems. *Meteor. Monogr.*, in press.

Houze, R. A., S. A. Rutledge, M. I. Biggerstaff, and B. F. Smull, 1989: Interpretation of Doppler Weather Radar Displays of Midlatitude Mesoscale Convective Systems. *Bull. Amer. Meteor. Soc.*, **70**, 608–619.

Houze, R. A., B. F. Smull, and P. Dodge, 1990: Mesoscale Organization of Springtime Rainstorms in Oklahoma. *Mon. Wea. Rev.*, **118**, 613–654.

Jameson, A. R., 1983a: Microphysical Interpretation of Multi-Parameter Radar Estimates in Rain. Part I: Interpretation of Polarization Measurements and Estimation of Raindrop Shapes. *J. Atmos. Sci.*, **40**, 1792–1802.

Jameson, A. R., 1983b: Microphysical Interpretation of Multi-Parameter Radar Estimates in Rain. Part II: Estimation of Raindrop Distribution Parameters by Combined Dual-Wavelength and Polarization Measurements. *J. Atmos. Sci.*, **40**, 1803–1814.

Jameson, A. R., 1985: Deducing the Microphysical Character of Precipitation from Multi-Parameter Radar Polarization Measurements. *J. Climate Appl. Meteor.*, **42**, 1037–1047.

Jensen, M. P., and Coauthors, 2016: The Midlatitude Continental Convective Clouds Experiment (MC3E). *Bull. Amer. Meteor. Soc.*, **97 (9)**, 1667–1686.

Keenan, T. D., K. Glasson, F. Cummings, T. S. Bird, J. Keeler, and J. Lutz, 1998: The BMRC/NCAR C-Band polarimetric (C-POL) radar system. *J. Atmos. Oceanic Technol.*, **15**, 871–886.

Khain, A., and M. Pinsky, 2018: *Physical Processes in Clouds and Cloud Modeling.* Cambridge University Press, 686 pp.

Korolev, A., and P. R. Field, 2015: Assessment of the performance of the inter-arrival time algorithm to identify ice shattering artifacts in cloud particle probe measurements. *Atmos. Meas. Tech.*, **8**, 761–777.

Korolev, A. V., 2007: Reconstruction of the sizes of spherical particles from their shadow images. Part I: theoretical consideration. *J. Atmos. Oceanic Technol.*, **24**, 376–389.

Korolev, A. V., E. F. Emery, J. W. Strapp, S. G. Cober, and G. A. Isaac, 2013: Quantification of the Effects of Shattering on Airborne Ice Particle Measurements. *J. Atmos. Oceanic Technol.*, **30**, 2527–2553.

Kumjian, M. R., 2012: The Impact of Precipitation Physical Processes on the Polarimetric Radar Variables. Ph.D. thesis, University of Oklahoma, 327 pp.

Kumjian, M. R., 2013a: Principles and applications of dual-polarization weather radar. Part I: Description of the polarimetric radar variables. *J. Operational Meteor.*, **1 (19)**, 226–242.

Kumjian, M. R., 2013b: Principles and applications of dual-polarization weather radar. Part II: Warm- and cold-season applications. *J. Operational Meteor.*, **1 (20)**, 243–264.

Kumjian, M. R., 2013c: Principles and applications of dual-polarization weather radar. Part III: Artifacts. *J. Operational Meteor.*, **1 (21)**, 265–274.

Kumjian, M. R., and K. A. Lombardo, 2017: Insights into the Evolving Microphysical and Kinematic Structure of Northeastern U.S. Winter Storms from Dual-Polarization Doppler Radar. *Mon. Wea. Rev.*, **145**, 1033–1061.

Kumjian, M. R., S. Mishra, S. E. Giangrande, T. Toto, A. V. Ryzhkov, and A. Bansemer, 2016: Polarimetric radar and aircraft observations of saggy bright bands during MC3E. *J. Geophys. Res.*, **121**, 3584–3607.

Kumjian, M. R., and A. V. Ryzhkov, 2008: Polarimetric Signatures in Supercell Thunderstorms. *J. Appl. Meteor. Climatol.*, **47**, 1940–1961.

Kumjian, M. R., A. V. Ryzhkov, H. D. Reeves, and T. J. Schuur, 2013: A Dual-Polarization Radar Signature of Hydrometeor Refreezing in Winter Storms. *J. Appl. Meteor. Climatol.*, **52**, 2549–2566.

Leroy, D., and Coauthors, 2017: Ice crystal sizes in high ice water content clouds. Part II: Statistics of mass diameter percentiles in tropical convection observed during the HAIC/HIWC project. *J. Atmos. Oceanic Technol.*, **34**, 117–136.

Liu, C., and A. Illingworth, 2000: Toward more accurate retrievals of ice water content from radar measurements of clouds. *J. Appl. Meteor.*, **39**, 1130–1146.

Lutz, J., P. Johnson, B. Lewis, E. Loew, M. Randall, and J. Van Andel, 1995: NCAR SPol: Portable polariemtric S-band radar. *Preprints, Ninth Symp. on Meteorological Observations and Instrumentation*, Charlotte, NC, Amer. Meteor. Soc., 408–410.

Marinescu, P. J., S. C. van den Heever, S. M. Saleeby, S. M. Kreidenweis, and P. J. De Mott, 2017: The Microphysical Roles of Lower-Tropospheric versus Midtropospheric Aerosol Particles in Mature-Stage MCS Precipitation. *J. Atmos. Sci.*, **74**, 3657–3678.

Matrosov, S. Y., R. F. Reinking, R. A. Kropfli, and B. W. Bartram, 1996: Estimation of Ice Hydrometeor Types and Shapes from Radar Polarization Measurements. *J. Atmos. Oceanic Technol.*, **13**, 85–96.

McFarquhar, G. M., J. A. Finlon, D. M. Stechman, W. Wu, R. C. Jackson, and M. Freer, 2018: University of Illinois/Oklahoma Optical Array Probe (OAP) Processing Software. URL https://doi.org/10.5281/zenodo.1285969, doi:10.5281/zenodo.1285969.

McFarquhar, G. M., and A. J. Heymsfield, 1998: The Definition and Significance of an Effective Radius for Ice Clouds. *J. Atmos. Sci.*, **55**, 2039–2052.

McFarquhar, G. M., M. S. Timlin, R. M. Rauber, B. F. Jewett, J. A. Grim, and D. P. Jorgensen, 2007: Vertical Variability of Cloud Hydrometeors in the Stratiform Region of Mesoscale Convective Systems and Bow Echoes. *Mon. Wea. Rev.*, **135**, 3405–3428.

Montopoli, M., N. Roberto, E. Adirosi, E. Gorgucci, and L. Baldini, 2017: Investigation of Weather Radar Quantitative Precipitation Estimation Methodologies in Complex Orography. *Atmosphere*, **8**, 34.

Murphy, A. M., R. M. Rauber, G. M. McFarquhar, J. A. Finlon, D. M. Plummer, A. A. Rosenow, and B. F. Jewett, 2017: A Microphysical Analysis of Elevated Convection in the Comma Head Region of Continental Winter Cyclones. *J. Atmos. Sci.*, **74**, 69–91.

Murphy, A. M., A. Ryzhkov, P. Zhang, G. McFarquhar, W. Wu, and D. Stechman, 2018: A Poalrimetric and Microphysical Analysis of the Stratiform Rain Region of MCSs. *2018 AMS Annual Meeting*, January 8-11, Austin, TX.

Newton, C. W., 1950: Structure and Mechanism of the Prefrontal Squall Line. *J. Operational Meteor*, **7**, 210–222.

Nguyen, C., M. Wolde, K. Baibakov, and A. Korolev, 2017: Detection and Estimation of High Ice Water Content using X-band and W-band Dual-Polarization Airborne Radar Data. *38th Conference on Radar Meteorology*, Chicago, IL, Amer. Meteor. Soc., 89.

Park, H., A. V. Ryzhkov, D. S. Zrnic, and K. Kim, 2009: The Hydrometeor Classification Algorithm for the Polarimetric WSR-88D: Description and Application to an MCS. *Wea. Forecasting*, **24**, 730–748.

Parker, M. D., and R. H. Johnson, 2000: Organizational Modes of Midlatitude Mesoscale Convective Systems. *Mon. Wea. Rev.*, **128**, 3413–3436.

Parker, M. D., and R. H. Johnson, 2004: Structures and Dynamics of Quasi-2D Mesoscale Convective Systems. *J. Atmos. Sci.*, **61**, 545–567.

Pedgley, D. E., 1962: A meso-synoptic analysis of the thunderstorms on 28 August 1958. Brit. Meteor. Off., Geophys. Mem., No. 106. London: Her Majesty's Stationery Office.

Protat, A., and Coauthors, 2016: The Measured Relationship between Ice Water Content and Cloud Radar Reflectivity in Tropical Convective Clouds. *J. Appl. Meteor. Climatol.*, **55**, 1707–1729.

Pruppacher, H. R., and J. D. Klett, 1997: *Microphysics of Clouds and Precipitation*. Oxford Press, second edition, 963 pp.

Rasmussen, R., M. Dixon, S. Vasiloff, F. Hage, S. Knight, J. Vivekanandan, and M. Xu, 2003: Snow Nowcasting Using a Real-Time Correlation of Radar Reflectivity with Snow Gauge Accumulation. *J. Appl. Meteor.*, **42**, 20–36.

Ryzhkov, A., P. Bukovcic, A. Murphy, P. Zhang, and G. McFarquhar, 2018: Ice microphysical retrievals using polarimetric radar data. *10th European Conference on Radar in Meteorology and Hydrology*, July 1-6, Ede, Netherlands.

Ryzhkov, A., P. Zhang, H. Reeves, M. Kumjian, T. Tschallener, S. Troemel, and C. Simmer, 2016: Quasi-Vertical Profiles–A New Way to Look at Polarimetric Radar Data. *J. Atmos. Oceanic Technol.*, **33**, 551–562.

Ryzhkov, A., and D. Zrnic, 1996a: Assessment of Rainfall Measurement That Uses Specific Differential Phase. *J. Appl. Meteor.*, **35**, 2080–2090.

Ryzhkov, A., D. Zrnic, and R. Fulton, 2000: Areal Rainfall Estimates Using Differential Phase. *J. Appl. Meteor.*, **39**, 263–268.

Ryzhkov, A., and Coauthors, 2017: Estimation of Depolarization Ratio Using Weather Radars with Simultaneous Transmission/Reception. *J. Appl. Meteor. Climatol.*, **56 (7)**, 1797–1816.

Ryzhkov, A. V., D. W. Burgess, D. S. Zrnic, T. Smith, and S. E. Giangrande, 2002: Polarimetric Analysis of a 3 May 1999 Tornado. *21st Conf. on Severe Local Storms*, San Antonio, Texas, Amer. Meteor. Soc., 515–518.

Ryzhkov, A. V., S. E. Giangrande, V. M. Melnikov, and T. J. Schuur, 2005a: Calibration Issues of Dual-Polarization Radar Measurements. *J. Appl. Meteor.*, **44**, 502–515.

Ryzhkov, A. V., S. E. Giangrande, and T. J. Schuur, 2005b: Rainfall Estimation with a Polarimetric Prototype of WSR-88D. *J. Appl. Meteor.*, **44**, 502–515.

Ryzhkov, A. V., M. R. Kumjian, S. M. Ganson, and A. P. Khain, 2013: Polarimetric Radar Characteristics of Melting Hail. Part I: Theoretical Simulations Using Spectral Microphysical Modeling. *J. Appl. Meteor. Climatol.*, **52**, 2849–2870.

Ryzhkov, A. V., T. J. Schuur, D. W. Burgess, and D. S. Zrnic, 2005c: Polarimetric Tornado Detection. *J. Appl. Meteor.*, **44**, 557–570.

Ryzhkov, A. V., and D. S. Zrnic, 1996b: Rain in Shallow and Deep Convection Measured with a Polarimetric Radar. *J. Atmos. Sci.*, **53**, 2989–2995.

Ryzhkov, A. V., and D. S. Zrnic, 1998: Discrimination between rain and snow with a polarimetric radar. *J. Appl. Meteor.*, **37**, 1228–1240.

Ryzhkov, A. V., D. S. Zrnic, and B. A. Gordon, 1998: Polarimetric Method for Ice Water Content Determination. *J. Appl. Meteor.*, **37**, 125–134.

Sachidananda, M., and D. S. Zrnic, 1986: Differential Propagation Phase Shift and Rainfall Rate Estimation. *Radio Sci.*, **21**, 235–247.

Sachidananda, M., and D. S. Zrnic, 1987: Rain Rate Estimates from Differential Polarization Measurements. *J. Atmos. Oceanic Technol.*, **4**, 588–598.

Sassen, K., 1987: Ice Cloud Content from Radar Reflectivity. *J. Climate Appl. Meteor.*, **26**, 1050–1053.

Schrom, R. S., and M. R. Kumjian, 2016: Connecting Microphysical Processes in Colorado Winter Storms with Vertical Profiles of Radar Observations. *J. Appl. Meteor. Climatol.*, **55**, 1771–1787.

Seliga, T. A., and V. N. Bringi, 1976: Potential Use of Radar Differential Reflectivity Measurements at Orthoganal Polarizations for Measuring Precipitation. *J. Appl. Meteor.*, **15**, 69–76.

Snyder, J. C., and A. V. Ryzhkov, 2015: Automated Detection of Polarimetric Tornadic Debris Signatures using a Hydrometeor Classification Algorithm. *J. Appl. Meteor. Climatol.*, **54 (9)**, 1861–1870.

Solomon, D. L., K. P. Bowman, and C. R. Homeyer, 2016: Tropopause-penetrating convection from three-dimensional gridded NEXRAD data. *J. Appl. Meteor. Climatol.*, **55**, 465–478.

Stanford, M., A. Warble, E. Zipser, J. Strapp, A. Leroy, A. Schwarzenboeck, R. Potts, and A. Protat, 2017: A ubiquitous ice size bias in simulations of tropical deep convection. *Atmos. Chem. Phys.*, **17**, 9599–9621.

Stechman, D. M., 2018: Observed Microphysical Characteristics and Inferred Thermodynamic Processes Contributing to the Structure, Evolution, and Maintenance of Nocturnal Elevated Mesoscale Convective Systems. Ph.D. thesis, University of Illinois, 192 pp.

Storm, B. A., M. D. Parker, and D. P. Jorgense, 2007: A Convective Line with Leading Stratiform Precipitation from BAMEX. *Mon. Wea. Rev.*, **135**, 1769–1785.

Straka, J. M., D. S. Zrnic, and A. V. Ryzhkov, 2000: Bulk Hydrometeor Classification and Quantification using Polarimetric Radar Data: Synthesis of Relations. *J. Appl. Meteor.*, **39**, 1341–1372.

Strapp, J. W., and Coauthors, 2016: The High Ice Water Content (HIWC) study of deep convective clouds: Report on science and technical plan. FAA Rep. DOT/FAA/TC–14/31, 105 pp. [Available online at http://www.tc.faa.gov/its/worldpac/techrpt/tc14–31.pdf].

Sulia, K. J., and M. R. Kumjian, 2017: Simulated Polarimetric Fields of Ice Vapor Growth Using the Adaptive Habit Model, Part II: A Case Study from the FROST Experiment. *Mon. Wea. Rev.*, **145**, 2303–2323.

Tian, J., X. Dong, B. Xi, J. Wang, C. R. Homeyer, G. M. McFarquhar, and J. Fan, 2016: Retrievals of ice cloud microphysical properties of deep convective systems using radar measurements. *J. Geophys. Res. Atmos.*, **121**, 10 820–10 839.

Tobin, D. M., and M. R. Kumjian, 2017: Polarimetric Radar and Surface-Based Precipitation-Type Observations of Ice Pellet to Freezing Rain Transitions. *Wea. Forecasting*, **32**, 2065–2082.

Troemel, S., M. R. Kumjian, A. V. Ryzhkov, C. Simmer, and M. Diederich, 2013: Backscatter Differential Phase–Estimation and Variability. *J. Appl. Meteor. Climatol.*, **52**, 2529–2548.

Troemel, S., A. V. Ryzhkov, K. Diederich, K. Muhlbauer, S. Kneifel, J. Snyder, and C. Simmer, 2017: Multisensor Characterization of Mammatus. *Mon. Wea. Rev.*, **145**, 235–251.

Troemel, S., A. V. Ryzhkov, P. Zhang, and C. Simmer, 2014: Investigations of Backscatter Differential Phase in the Melting Layer. *J. Appl. Meteor. Climatol.*, **53**, 2344–2359.

UCAR/NCAR-Earth Observing Laboratory, 1996: S-PolKa: S-band/Ka-band Dual Polarization, Dual Wavelength Doppler Radar. UCAR/NCAR - Earth Observing Laboratory. https://doi.org/10.5065/D6RV0KR8.

UCAR/NCAR-Earth Observing Laboratory, 2012: S-PolKa Radar, fully corrected, final moments data in cfRadial format. Version 1.0. doi:10.5065/d6j101ck. https://data.eol.ucar.edu/dataset/347.017.

Van de Hulst, H., 1981: *Light Scattering by Small Particles*. Dover.

Van Den Broeke, M. S., and S. T. Jauernic, 2014: Spatial and Temporal Characteristics of Polarimetric Tornadic Debris Signatures. *J. Appl. Meteor. Climatol.*, **53**, 2344–2359.

Van Den Broeke, M. S., D. M. Tobin, and M. R. Kumjian, 2016: Polarimetric Radar Observations of Precipitation Type and Rate from the 2–3 March 2014 Winter Storm in Oklahoma and Arkansas. *Wea. Forecasting*, **31**, 1179–1196.

Van Den Broeke, M. S., D. M. Tobin, and M. R. Kumjian, 2017: Polarimetric Radar Observations of Precipitation Type and Rate from the 2-3 March 2014 Winter Storm in Oklahoma and Arkansas. *Wea. Forecasting*, **31**, 1179–1196.

Van Lier-Walqui, M., and Coauthors, 2016: On Polarimetric Radar Signatures of Deep Convection for Model Evaluation: Columns of Specific Differential Phase Observed during MC3E. *Mon. Wea. Rev.*, **144**, 737–758.

Vivekanandan, J., V. N. Bringi, M. Hagen, and P. Meischner, 1994: Polarimetric Radar Studies of Atmospheric Ice Particles. *IEEE Trans. Geosci. Remote Sens.*, **32**, 1–10.

Williams, E. R., and Coauthors, 2015: Measurements of Differential Reflectivity in Snowstorms and Warm Season Stratiform Systems. *J. Appl. Meteor. Climatol.*, **54**, 573–595.

Wu, W., and G. M. McFarquhar, 2016: On the Impacts of Different Definitions of Maximum Dimension for Nonspherical Particles Recorded by 2D Imaging Probes. *J. Atmos. Oceanic Technol.*, **33**, 1057–1072.

Xue, L., and Coauthors, 2017: Idealized Simulations of a Squall Line from the MC3E Field Campaign Applying Three Bin Microphysics Schemes: Dynamic and Thermodynamic Structure. *Mon. Wea. Rev.*, **145**, 4789–4812.

Yoneyama, K., C. Zhang, and C. N. Long, 2013: Tracking Pulses of the Madden-Julian Oscillation. *Bull. Amer. Meteor. Soc.*, **94**, 1871–1891.

Zahrai, A., and D. S. Zrnic, 1993: The 10-cm-Wavelength Polarimetric Weather Radar at NOAA's National Severe Storms Laboratory. *J. Atmos. Oceanic Technol.*, **10 (5)**, 649–662.

Zhang, G., 2017: *Weather Radar Polarimetry.* CRC Press, 304 pp.

Zipser, E. J., 1969: The rold of organized unsaturated convective downdrafts in the structure and rapid decay of an equatorial disturbance. *J. Appl. Meteor.*, **8**, 799–814.

Zrnic, D. S., 1996: Weather Radar Polarimetry–Trends Toward Operational Applications. *Bull. Amer. Meteor. Soc.*, **77**, 1529–1534.

Zrnic, D. S., N. Balakrishnan, C. L. Ziegler, V. N. Bringi, K. Aydin, and T. Matejka, 1993: Polarimetric Signatures in the Stratiform Region of a Mesoscale Convective System. *J. Appl. Meteor.*, **32**, 678–693.

Zrnic, D. S., A. Ryzhkov, J. Straka, Y. Liu, and J. Vivekanandan, 2001: Testing a Procedure for Automatic Classification of Hydrometeor Types. *J. Atmos. Oceanic Technol.*, **18**, 892–913.

Zrnic, D. S., and A. V. Ryzhkov, 1999: Polarimetry for Weather Surveillance Radars. *Bull. Amer. Meteor. Soc.*, **80**, 389–406.